Weak lensing magnification in SpARCS

Dissertation
zur
Erlangung des Doktorgrades (Dr. rer. nat.)
der
Mathematisch-Naturwissenschaftlichen Fakultät
der
Rheinischen Friedrich-Wilhelms-Universität Bonn

vorgelegt von
Alexandru Tudorică
aus
Ghirdoveni, Rumänien

Bonn 2020

Angefertigt mit Genehmigung der Mathematisch-Naturwissenschaftlichen Fakultät der Rheinischen Friedrich-Wilhelms-Universität Bonn

1. Gutachter:	Prof. Dr. Hendrik Hildebrandt
2. Gutachter:	Prof. Dr. Peter Schneider

Tag der Promotion: 12.09.2019
Erscheinungsjahr: 2020

To the Titans of Science

Abstract

The growth of large scale structure is one of the fundamental predictions of any cosmological model. Galaxy clusters are the highest peaks in the cosmological matter density field and therefore of prime importance in cosmology. The calibration of the high-redshift ($z > 1$) galaxy cluster mass-richness relation is particularly important as it contains information about galaxy clusters in their assembly phase, when assumptions such as virial/hydrostatic equilibrium might not be valid. Measuring the mass-richness relation over a wide range in redshift will help to better understand the astrophysics of clusters over time and simultaneously provide cosmological structure growth constraints.

An independent and novel method to acquire this information is the use of the weak gravitational lensing magnification effect, which is able to accurately measure the masses of large samples of high-z clusters in a statistical way (i.e. through stacking) without the need to resolve background galaxies. This magnification effect leads to a change of source counts which then can be analysed by measuring the angular cross-correlation function of optically selected Lyman-break galaxies and high-redshift clusters. We apply this method to the hundreds of new high-z galaxy clusters found in the SpARCS (Spitzer Adaptation of the Red-Sequence Cluster Survey) infrared survey, observed also with the CFHT in the optical *ugrz*-bands.

We measure the cross-correlation between the positions of galaxy cluster candidates and LBGs and detect a weak lensing magnification signal for all bins at a detection significance of 2.6-5.5σ. In particular, the significance of the measurement for clusters with $z > 1.0$ is 4.1σ; for the entire cluster sample we obtain an average M_{200} of $1.28^{+0.23}_{-0.21} \times 10^{14}\ M_{\odot}$.

Our measurements demonstrate the feasibility of using weak lensing magnification as a viable tool for determining the average halo masses for samples of high redshift galaxy clusters. The results also establish the success of using galaxy over-densities to select massive clusters at $z > 1$. Additional studies are necessary for further modelling of the various systematic effects we discussed.

Contents

List of Figures 1

List of Tables 3

1 Cosmology and Galaxy Clusters 7
- 1.1 Cosmological Framework . . . 7
  - 1.1.1 The Einstein Field Equations . . . 7
  - 1.1.2 Isotropy and Homogeneity . . . 8
  - 1.1.3 Friedmann-Lemaître Models . . . 9
  - 1.1.4 Cosmological Redshift . . . 11
  - 1.1.5 Cosmological Distance Measurements . . . 12
- 1.2 The Formation of Structures in the Universe . . . 15
  - 1.2.1 Linear Perturbation Theory . . . 15
  - 1.2.2 Cosmological Density Fluctuations . . . 17
  - 1.2.3 Gaussian Random Fields . . . 18
  - 1.2.4 The Dark Matter Field . . . 19
  - 1.2.5 The Model of Spherical Collapse . . . 20
  - 1.2.6 The Number Density of Dark Matter Halos . . . 21
  - 1.2.7 The Lens Bias . . . 23
  - 1.2.8 The NFW Profile . . . 23
  - 1.2.9 The Halo Model . . . 23
- 1.3 Clusters of Galaxies . . . 27
  - 1.3.1 Properties . . . 27
  - 1.3.2 Detection . . . 29
  - 1.3.3 Scaling Relations . . . 29
  - 1.3.4 Significance . . . 32

2 Gravitational Lensing 35
- 2.1 Outline of Gravitational Lensing . . . 35
- 2.2 Weak Gravitational Lensing . . . 38
  - 2.2.1 Magnification of Number Counts . . . 40
  - 2.2.2 Galaxy Clusters and Gravitational Lensing . . . 41

3 Data **43**
3.1 SWIRE - Infrared Data . . . 43
3.2 SpARCS - Optical Follow-up of SWIRE . . . 43
3.2.1 Cluster Catalogue . . . 45
3.3 CFHT *ugriz* Optical Data . . . 47
3.4 Data Reduction & Source Selection . . . 49
3.4.1 Basic Data Reduction . . . 49
3.4.2 LBG Candidates . . . 58

4 Galaxy clusters in SpARCS **65**
4.1 Magnification of Number Counts . . . 65
4.2 Magnification Model . . . 66
4.2.1 Signal-to-Noise Ratio Estimates . . . 69
4.3 Composite-Halo Fits . . . 69
4.3.1 Masking Correction . . . 71

5 Results and discussion **73**

6 Summary and Conclusions **81**

A – Appendix: CFHT Optical Data Properties **83**

B – Appendix: Data Release Website **87**

Bibliography **95**

List of Figures

1.1 Distance measurements in cosmology . . . 13
1.2 Halo mass functions . . . 22
1.3 A very massive galaxy cluster - IDCS J1426.5+3508 . . . 28
1.4 Mass-richness relation for simulated Euclid data . . . 31
1.5 N_{200} maxBCG-RCS2 richness comparison . . . 32
1.6 Observational constraints of cosmological parameters . . . 33

2.1 Gravitational lens geometry outline . . . 36
2.2 Effect of convergence and shear on a circular source . . . 40

3.1 Outline of the SpARCS fields . . . 44
3.2 Redshift and richness distribution of SpARCS clusters . . . 47
3.3 A very high redshift galaxy cluster - SpARCS-1613 . . . 48
3.4 Basic data reduction output . . . 50
3.5 Bi-dimensional distribution of the reference astrometric residuals . . . 51
3.6 Bi-dimensional distribution of the internal astrometric residuals . . . 52
3.7 Matching of individual frames per pointing . . . 53
3.8 Example of a distortion map . . . 54
3.9 PSF anisotropy before and after correction for one field . . . 55
3.10 Map of the median depth for a field . . . 56
3.11 Field mask detail . . . 57
3.12 Field masking . . . 57
3.13 Lyman Break galaxies and the dropout technique . . . 59
3.14 Colour-colour number density plot of galaxies in SpARCS . . . 61
3.15 Examples of LBG candidates rejected after the visual inspection . . . 61
3.16 SpARCS *u*-dropouts numbercounts . . . 62
3.17 Histogram of the redshift distribution of SpARCS clusters . . . 63

4.1 Correlation matrix of the cross-correlation function . . . 70
4.2 Masking correction factors f_{mask} as a function of the redshift . . . 72

5.1 Angular cross-correlation measurements for clusters binned in redshift . 74
5.2 Angular cross-correlation measurements for clusters binned in richness 74

5.3 Angular cross-correlation measurements for clusters binned in both redshift and richness 75
5.4 Richness proxies for the galaxy cluster candidates common to CFHTLenS and SpARCS 75
5.5 Mass and richness for the SpARCS cluster samples compared to the the CFHTLenS analysis results 76
5.6 Mass-richness relation for the SpARCS cluster samples as a function of redshift 77

List of Tables

3.1 Properties of the six SpARCS fields 45
3.2 Properties of the CFHT optical data 49

5.1 Mass estimates for various sub-samples of the SpARCS clusters 79

A.1 CFHT optical data properties per pointing per filter 83

B.1 Data release website keys description 89

Thesis structure

This thesis is organized as follows:

- In Chapter 1, we begin by summarizing the cosmological model used as a framework for describing the Universe. Aspects relevant to this thesis regarding the formation of structures in the Universe are being described, starting from the cosmological background and going through the evolution of structures in the linear regime. The chapter ends with a short overview of the formation, physical properties, scaling relations and cosmological significance of clusters of galaxies.
- The basic concepts of gravitational lensing are reviewed in Chapter 2. The formalism of weak gravitational lensing is summarized, particularly emphasising the weak gravitational lensing magnification, which stands at the basis of the present work.
- In Chapter 3 the properties of the data set are detailed. We start by describing the the Spitzer Space telescope SWIRE (infrared) survey properties and continue with the optical follow-up to which this thesis has also contributed to and is based upon. An overview of the motivation of the optical follow-up as well as of the data acquisition strategy and subsequent post-processing for obtaining the final scientific catalogues is presented. The chapter ends with the construction of the two main samples of objects - cluster candidates (as lenses) and Lyman-Break Galaxy candidates (as sources).
- Chapter 4 reviews the application of the weak gravitational lensing magnification theory to the data sets previously described, along with signal-to-noise estimates, the composite halo model used for fitting the data and further corrections related to the masking of sources by lens members.
- Chapter 5 contains the results of the measurements along with literature comparisons for the calibration of the mass-richness relation of galaxy clusters to high redshift. We also discuss the various simplifying assumptions and sources of systematic or statistical biases or errors.
- In Chapter 6, a summary of the main results of the thesis as well as a brief discussion of their importance and further avenues of research is presented.

- Appendix A and Appendix B contain detailed information about each of the optical data individual pointings and a short description of the public release website and data, along with the physical parameters estimated or measured.

CHAPTER 1

Cosmology and Galaxy Clusters

1.1 Cosmological Framework

1.1.1 The Einstein Field Equations

Cosmology is the branch of science that addresses the physics of the Universe as a whole; its origin, properties and evolution. Although many cosmological models were proposed since the ancient times, it wasn't until the early 20th century when cosmology became a modern science, once the theoretical tools and observational instruments available could be used to create testable, compelling theories of cosmology. The development of the General theory of Relativity (hereafter GR) coupled with better, more accurate astronomical instruments, enabled us to measure the quantities and properties predicted by the new theories of cosmology.

The four fundamental forces discovered so far by modern physics have very different manifestations in the Universe also due to their interaction range. While the strong and electroweak forces play a direct role only at subatomic scales, the electromagnetic and gravitational forces have an apparently infinite range of interaction. The relative strength between the coupling constants of gravity and electromagnetism is over 36 orders of magnitude in favour of the latter. However, the fact that there are two types of electric charge opposite to each other makes electromagnetism irrelevant for interactions between large celestial bodies such as planets, stars and galaxies, since these contain on average equal numbers of protons and electrons, therefore having a null net electric charge. A theory able to describe the evolution of the Universe is therefore mostly a theory of gravity. In addition to the self-interaction of matter, a cosmological theory must also address the geometrical properties of space. This is because the Euclidean geometry that we are familiar with in our daily lives might not accurately describe the Universe as a whole, and we will see later that this is indeed the case.

GR is a geometric theory of gravity (Einstein 1915a;b;c;d; 1916), connecting Newton's law of universal gravitation with special relativity, providing a unified descrip-

tion of gravity as a geometric property of time and space directly influenced by the presence of matter. A particularly simple and intuitive description of GR given by Wheeler & Ford (1998) states: "Spacetime tells matter how to move; matter tells spacetime how to curve." This connection is described by a system of partial differential equations known as the Einstein Field Equations:

$$G_{\mu\nu} = -\frac{8\pi G}{c^4} T_{\mu\nu} - \Lambda g_{\mu\nu}, \tag{1.1}$$

where $G_{\mu\nu}$ is the Einstein tensor, G is Newton's gravitational constant, c is the speed of light in vacuum, $T_{\mu\nu}$ is the stress-energy tensor, and Λ $g_{\mu\nu}$ is the cosmological constant.

1.1.2 Isotropy and Homogeneity

The Einstein Field Equations can be used to construct a cosmological theory based on postulating that that the laws of physics do not change as a function of position in space and that on large scales the Universe is homogeneous and isotropic. Also called the cosmological principle, it implies that for any observer the Universe looks the same on large scales in a statistical way. These assumptions have the added benefit of providing us with simple solutions to the field equations, enabling us to construct straightforward cosmological theories.

Fortunately, there is a great deal of evidence in support of these principles. Studies of the galaxy distributions on very large scales show that indeed the Universe looks nearly homogeneous and that there are few structures at that level. Upper limits for structures still consistent with the cosmological principle have been estimated to be roughly 260 Mpc/h (Yadav et al. 2010). However, there is some evidence of larger structures than these upper limits (Horvath et al. 2013; Clowes et al. 2013), hinting at the need for more complicated cosmological models. The Planck satellite data have shown that the CMB fluctuations are consistent with statistical isotropy (to one part in 10^5), although there are some indications of anomalies with respect to the current cosmological model, Λ Cold Dark Matter (ΛCDM, Planck Collaboration et al. (2015a) - e.g. a large cold spot on the sky that cannot be easily explained at the moment invoking instrumental effects, even though obtaining only the CMB signal is a very complex process).

Therefore, there are incentives to consider such simple homogenous and isotropic models. If we consider a homogeneous sphere of density $\rho(t)$ able to expand or contract in such a way that the density remains spatially uniform, the behaviour of a matter element of position $\mathbf{x}$ with time t is described by:

$$r(t) = a(t)\mathbf{x}, \tag{1.2}$$

where the function $a(t)$ represents the time dependent scale factor, defined in such a way that it is normalized at the current cosmic time t_0: $a(t_0) \equiv a_0 = 1$. The evolution of such a particle is therefore fully described by the scale factor $a(t)$ and its comoving coordinate (position) $\mathbf{x}$.

One of the simplest solutions to the field equations for a homogeneous and isotropic space is the Friedmann-Lemaitre-Robertson-Walker (FLRW) metric (Friedmann 1922; Lemaître 1933; Robertson 1935; Walker 1937), which can be written in comoving coordinates as:

$$\mathrm{d}s^2 = c^2\mathrm{d}t^2 - a^2(t)[\mathrm{d}\chi^2 + f_k^2(\chi)(\mathrm{d}\theta^2 + \sin^2\theta\mathrm{d}\phi^2)], \tag{1.3}$$

where χ, θ, ϕ are the radial comoving and respectively angular coordinates, k is the curvature parameter and be chosen to be ± 1 or 0 for spaces of constant positive, negative or zero spatial curvature, entering into the comoving angular diameter distance $f_k(\chi)$ as:

$$f_k(\chi) = \begin{cases} k^{-1/2}\sin(k^{1/2}\chi) & (k > 0) \\ \chi & (k = 0) \\ (-k)^{-1/2}\sinh[(-k)^{1/2}\chi] & (k < 0) \end{cases} \tag{1.4}$$

In the framework of such a model, the comoving and fundamentals observers are the same, with worldlines characterized by constant spatial coordinates (χ, θ, ϕ) and the eigentime of all observers coincides with the cosmic time t.

1.1.3 Friedmann-Lemaître Models

Using as input the metric described by equation 1.3 into the Einstein Field Equations (equation 1.1), one obtains an energy-momentum tensor $T_{\mu\nu}$ that represents matter under the form of a homogeneous perfect fluid of density $\rho(t)$ and pressure $p(t)$. The components of the field equations then reduce to two independent differential equations, describing the dynamical evolution of the scale factor $a(t)$:

$$H^2(t) = \left(\frac{\dot{a}}{a}\right)^2 = \frac{8\pi G}{3}\rho - \frac{kc^2}{a^2} + \frac{\Lambda}{3}, \tag{1.5}$$

and

$$\frac{\ddot{a}}{a} = -\frac{4\pi G}{3}\left(\rho + \frac{3p}{c^2}\right) + \frac{\Lambda}{3}, \tag{1.6}$$

with Λ representing the cosmological constant that Einstein originally introduced in order to allow for solutions describing a static Universe. The first equation can also be derived from thermodynamic considerations and is equivalent to the first law of thermodynamics assuming that the expansion of the Universe is an adiabatic process, with the change in energy as a function of time in a comoving volume being equal to the expansion or contraction work carried out within the same comoving volume. Λ is not included in the pressure and density quantities used in the equations above, but it can be described as a vacuum energy density that has negative pressure (therefore accelerating the expansion of the Universe). Equation 1.6 states that both the energy density and the pressure can cause the expansion rate to change, pressure playing a similar role to that of mass (energy) from a gravitational point of view, in accordance with the principles of General Relativity.

$H^2(t) = \frac{\dot{a}}{a}$ is the Hubble parameter, with its present value $H_0 \equiv H(t_0)$, also called the Hubble constant. H_0 is one of the most fundamental cosmological parameters since it represents the rate of expansion for the Universe, while simultaneously being very difficult to measure precisely. Due to large uncertainties in the knowledge of the exact value of the Hubble constant that lasted for many decades, the Hubble constant is usually expressed as:

$$H_0 = 100\,h\,\mathrm{km\,s^{-1}\,Mpc^{-1}} \approx 3.2 \times 10^{-18}\,h\,\mathrm{s^{-1}}, \tag{1.7}$$

where h is a dimensionless parameter which we assume in the following to have a value of 0.6726 (Planck Collaboration et al. 2015b).

For a complete set of equations able to describe the evolution of the scale factor $a(t)$ with time, we also require the equations of state that relate pressure and density for each main component of the Universe that contributes to the total energy density. At different epochs, distinct components dominate the total energy density of the Universe, with the following equations of state:

$$p_\mathrm{m} = 0 \implies \rho_\mathrm{m} \propto a^{-3}\,\text{(matter)}, \tag{1.8}$$

$$p_\mathrm{r} = \frac{\rho_r c^2}{3} \implies \rho_\mathrm{r} \propto a^{-4}\,\text{(radiation)}, \tag{1.9}$$

$$\rho_\Lambda = \text{constant} \implies p_\Lambda \propto -\rho_\Lambda\,\text{(vaccum energy)}. \tag{1.10}$$

As the contribution to the total energy density of the Universe differs for each component as a function of the scale factor in different ways, the Universe went through epochs where each of these components was the dominant one, as well as transition points when the density of two components was the same. Assuming a flat Universe ($k = 0$) and solving Equation 1.5 at times when each component was dominant:

$$a \propto t^{2/3}\,\text{(matter)}, \tag{1.11}$$

$$a \propto t^{1/2}\,\text{(radiation)}, \tag{1.12}$$

$$a \propto e^{\sqrt{\frac{8\pi G}{3}\rho}t}\,\text{(vaccum energy)}. \tag{1.13}$$

The critical density (ρ_crit) is defined as the density that the Universe would need to have today (at $t = t_0$) in order to have a null curvature ($k = 0$) and usually densities ρ are normalized to it. It can be derived from Equation 1.5 by letting $t = t_0$ and $H_0 = \dot{a}(t_0)$:

$$\rho_\mathrm{crit} \equiv \frac{3H_0^2}{8\pi G} \approx 9.22 \times 10^{-30}\,h^2\,\mathrm{g\,cm^{-3}}, \tag{1.14}$$

Rewriting the first Friedmann equation in terms of the density parameters:

$$\Omega_{\rm m} \equiv \frac{\rho_{\rm m}}{\rho_{\rm crit}};\ \ \Omega_{\rm r} \equiv \frac{\rho_{\rm r}}{\rho_{\rm crit}};\ \ \Omega_\Lambda \equiv \frac{\rho_\Lambda}{\rho_{\rm crit}} = \frac{\Lambda c^2}{3H_0^2}, \tag{1.15}$$

we obtain

$$H^2(t) = H_0^2[a^{-4}\Omega_{\rm r} + a^{-3}\Omega_{\rm m} + a^{-2}(1-\Omega_0) + \Omega_\Lambda], \tag{1.16}$$

with the total density parameter today being defined as

$$\Omega_0 = \Omega_{\rm m} + \Omega_{\rm r} + \Omega_\Lambda. \tag{1.17}$$

and

$$k = \left(\frac{H_0}{c}\right)^2 (\Omega_0 - 1) \approx \left(\frac{H_0}{c}\right)^2 (\Omega_{\rm m} + \Omega_\Lambda - 1). \tag{1.18}$$

Equations 1.16, 1.17 and 1.18 imply that the curvature of the Universe is determined by the total density, with:

$$\Omega_0 > 1 \iff k > 0, \tag{1.19}$$

$$\Omega_0 = 1 \iff k = 0, \tag{1.20}$$

$$\Omega_0 < 1 \iff k < 0. \tag{1.21}$$

The last decades have seen the birth of the so-called precision cosmology, with many of the critical cosmological parameters being very well constrained observationally. Very different types of observations sensitive to different kinds of systematic errors now provide values consistent with each other for these parameters, setting the basis for the concordance Λ-Cold-Dark-Matter cosmological model. In the rest of this thesis we assume $H_0 = 67.26$ km s^{-1} Mpc^{-1}, $\Omega_{\rm m} = 0.316$, $\Omega_\Lambda = 1 - \Omega_{\rm m} = 0.684$ (see Planck Collaboration et al. 2015b), while distances are expressed in Mpc.

1.1.4 Cosmological Redshift

The cosmological expansion of the Universe is at the basis of the Hubble law, first derived from the general relativity equations by Georges Lemaître in 1927. Electromagnetic radiation emitted by comoving sources in the Universe arrives at observers with larger wavelengths. For small distances, this change in wavelength is directly proportional to the spatial separation between the source and observer for a homogeneously expanding Universe. The redshift z is defined as:

$$z \equiv \frac{\lambda_{\rm observed}}{\lambda_{\rm emitted}} - 1 = \frac{1}{a(t)}. \tag{1.22}$$

Since our Universe is not expanding at a constant rate and is not Euclidean at large scales, redshift is not a unique way of measuring distances. Instead, we define differ-

ent distance measurements for different applications.

1.1.5 Cosmological Distance Measurements

Comoving Distance

In an expanding Universe with a non-Euclidean geometry, distance measurements can become quite complicated. One of the most fundamental ways of measuring distances in such a Universe is based on the comoving distance, which always remains constant between two comoving observers. In the framework of General Relativity, massless particles such as photons propagate in space along null geodesics ($\mathrm{d}s^2 = 0$). The comoving distance w between an observer at the origin and another at a redshift $z(t)$, setting $\mathrm{d}\phi = 0$ since we want to measure radial distances, can be obtained from the FLRW metric starting with:

$$c\,\mathrm{d}t = a(t)\,\mathrm{d}w. \tag{1.23}$$

As the velocity of light is not a constant through comoving coordinates, we cannot simply multiply c with time in order to obtain the comoving distance. Instead, we must integrate over this change of the velocity of light in comoving coordinates for the duration of the propagation, yielding (see Davis & Lineweaver 2004):

$$w = c \int_{t_{\mathrm{emission}}}^{t_0} \frac{\mathrm{d}t'}{a(t')}, \tag{1.24}$$

where t_{emission} is the time when the photons detected by the observer were emitted. By parametrizing time using redshift, and using the definition of the Hubble parameter, we can cast Equation 1.24 in terms of observables:

$$w = \frac{c}{H_0} \int_0^z \frac{\mathrm{d}z'}{\sqrt{\Omega_{\mathrm{r}}(1+z^4) + \Omega_{\mathrm{m}}(1+z^3) + (1-\Omega_0)(1+z)^2 + \Omega_\Lambda}}. \tag{1.25}$$

One comoving distance of great significance is the one a photon would have travelled freely (i.e. in absence of any interaction) since $t = 0$ (or by setting $z \longrightarrow \infty$ in Equation 1.25), since no information could have been propagated further according to GR. This means that regions separated by more than this distance cannot be causally connected, in effect creating an observational *horizon*. This *comoving horizon* increases in size with time and structures larger than the horizon will enter it at later times.

Angular Diameter Distance

The angular diameter distance is defined as the angle θ that and object of size l subtends on the sky. For small angles, the angular diameter distance D_{ang} is then expressed as:

$$D_{\mathrm{ang}} = \frac{l}{\theta}. \tag{1.26}$$

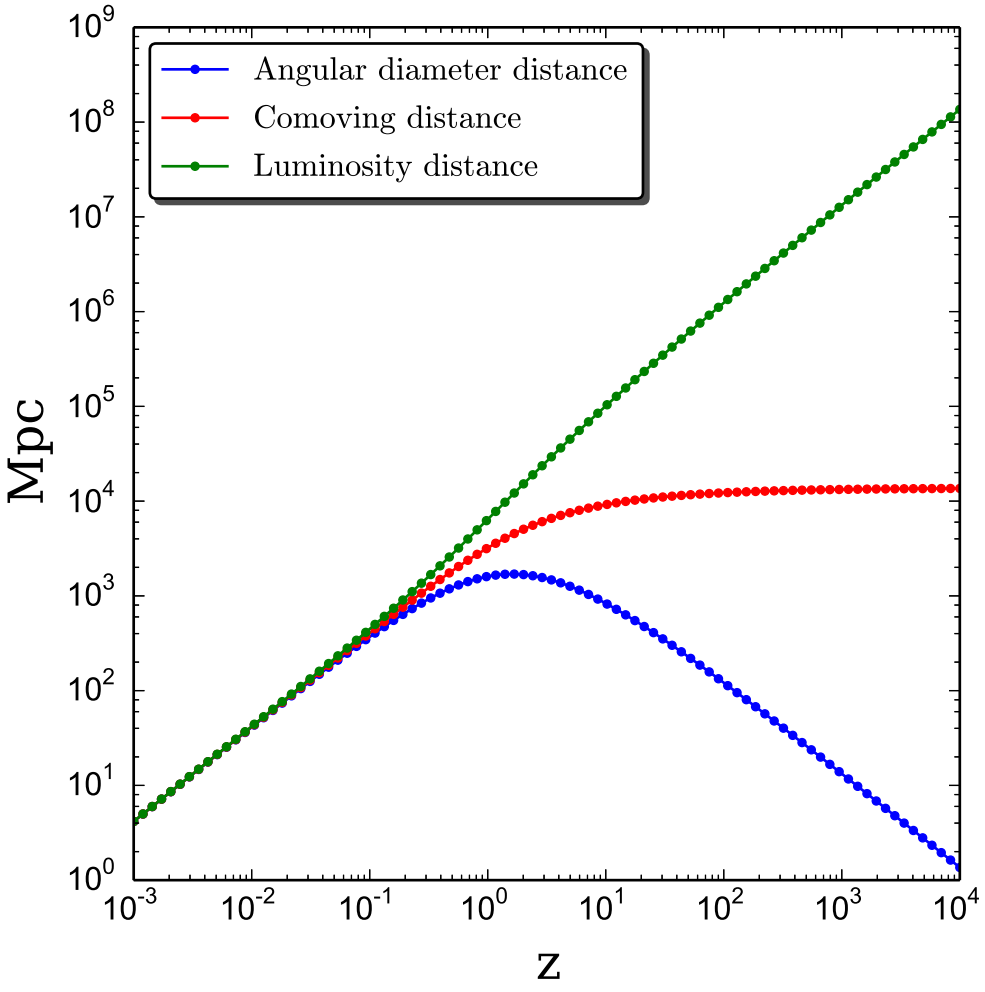

Figure 1.1: A comparison between different types of cosmological distance measures, from z = 0 to the redshift corresponding to the matter - radiation equality (z ≈ 10 000). The background cosmology is $H_0 = 72 \mathrm{km\,s^{-1}Mpc^{-1}}$, $\Omega_\Lambda = 0.7$, $\Omega_\mathrm{m} = 0.3$, $\Omega_\mathrm{r} = 8.24 \times 10^{-5}$, and the Universe is assumed to be flat ($k = 0$).

In a flat, expanding Universe, the angular diameter distance definition has to take into account the fact that the comoving size of the object is actually l/a and that the angle subtended is $\theta = (l/a)/w(a)$, giving:

$$D_{\mathrm{ang}} = \frac{w}{1+z}. \tag{1.27}$$

A very interesting property of the angular diameter distance is that it is not increasing linearly with redshift, actually having a peak at $z \sim 1.5$ for a ΛCDM cosmology, as can be seen in Figure 1.1, where the different distance measurements are compared as a function of z. Therefore, in a flat Universe objects at large redshift appear larger than they would at an intermediate redshift.

Luminosity Distance

Yet another distance measurement gives a precise way of dealing with the flux of light emitted by distant objects. In an Euclidean space the flux of light F is decreasing with the square of the distance d, for a source of luminosity L as: $F = \frac{L}{4\pi d^2}$. Since space is expanding while photons are travelling, the observed flux is further diluted. It has been shown (Ellis 2006) that the luminosity distance can be related to the angular diameter distance in the following way:

$$D_{\mathrm{lum}} = \frac{D_{\mathrm{ang}}}{a^2}. \tag{1.28}$$

This equation is valid only for bolometric quantities. For specific wavelength bands one must compensate the redshift induced change in frequency in order to convert the flux to the rest frame (also called the K-correction), or to compare images of objects taken through the same filter but situated at different redshifts.

All three cosmological distances defined above are larger in a Universe with a cosmological constant than in one with $\Omega_\Lambda = 0$, since the expansion rate would be larger in a matter-dominated Universe (with the same Hubble constant).

Distance Modulus

The prevalent use of magnitudes instead of fluxes in optical astronomy leads to another distance measurement quantity, the distance modulus DM, defined as:

$$DM \equiv 5 \log \frac{D_{\mathrm{lum}}}{10\,\mathrm{pc}}. \tag{1.29}$$

1.2 The Formation of Structures in the Universe

The Friedmann-Lemaître category of models described above are very well suited for describing perfectly homogeneous and isotropic Universes. However, our Universe is far from being so on scales smaller than about 200 Mpc, with clusters, voids, galaxies, stars and planets representing very large over-densities of the matter field (when compared with the critical density). One extension of the cosmological standard model that addresses both the horizon problem and the creation of over-densities is the inflationary scenario. Shortly, it is postulating a period in the very early Universe when space expanded exponentially, in such a way that inhomogeneities, anisotropies and the curvature of space are smoothed out, as well as simultaneously enlarging tiny quantum fluctuations to macroscopic scales. These minute inhomogeneities further develop through gravitational instability inherent in such a configuration and are detectable at the earliest times as anisotropies in the CMB. In the following section we will summarize the physics of large scale structure formation.

1.2.1 Linear Perturbation Theory

To study the evolution of the density perturbations at scales smaller than the horizon size, Newtonian physics offers a sufficiently accurate approximation of the GR results. As discussed above, matter can be considered to be a perfect fluid, with a mass density $\rho(\mathbf{x}, t)$, pressure $P \ll \rho$, and with a position $r(\mathbf{x}) = a(t)\mathbf{x}(t)$ and velocity $\mathbf{u} = \frac{\mathrm{dr}}{\mathrm{d}t}$ for a gas element. Its properties and evolution can be described with three equations:

$$\frac{\partial \mathbf{u}}{\partial t} + (\mathbf{u} \cdot \nabla_r)\mathbf{u} = -\nabla_r \Phi_{\mathrm{gr}}, \tag{1.30}$$

representing the **Euler equation** and describing the acceleration of the element, with $\Phi_{\mathrm{gr}}(\mathbf{x}, t)$ being the gravitational potential,

$$\nabla_r^2 \Phi_{\mathrm{gr}} = 4\pi G\rho - \Lambda, \tag{1.31}$$

which satisfies the **Poisson equation** and is modified in order to account for a cosmological constant, and

$$\frac{\partial \rho(\mathbf{x}, t)}{\partial t} + \nabla_r \cdot [\rho \mathbf{u}] = 0, \tag{1.32}$$

which describes the conservation of mass, also called the **continuity equation**. This set of equations has as a solution an expanding, homogeneous and isotropic Universe. As long as we remain well within sub-horizon scales, the addition of the cosmological constant in Equation 1.31 has no direct effect on the description of perturbations in the matter density field, amounting to a smooth background.

However, it is more useful to work with the equations rewritten in comoving co-

ordinates. The density contrast and respectively the velocity field can be written as:

$$\delta(\mathbf{r}, t) = \frac{\rho(\mathbf{r}, t) - \overline{\rho}(t)}{\overline{\rho}(t)}, \tag{1.33}$$

$$\mathbf{u}(\mathbf{r}, t) = \frac{\dot{a}}{a}\mathbf{r} + \mathbf{v}\left(\frac{\mathbf{r}}{a(t)}, t\right), \tag{1.34}$$

with $\mathbf{v} = \mathbf{u} - (\dot{a}/a)\mathbf{r}$ representing the peculiar velocity.

Since we are interested in the evolution of the small perturbations of the matter density field and the set of equations 1.30, 1.31 and 1.32 is non-linear and cannot be solved analytically, we linearize them by considering only first order terms for small δ and $\mathbf{v}$, discarding the terms containing δ^2 or $\mathbf{v}^2$ (Schneider 2006):

$$\frac{\partial \mathbf{v}}{\partial t} + \frac{\dot{a}}{a}\mathbf{v} = -\frac{1}{a}\nabla\Phi, \tag{1.35}$$

$$\nabla_{\mathrm{x}}^2\Phi = \frac{3H_0^2\Omega_{\mathrm{m}}}{2a}\delta, \tag{1.36}$$

$$\frac{\partial \delta}{\partial t} + \frac{1}{a}\nabla_{\mathrm{x}} \cdot \mathbf{v} = 0, \tag{1.37}$$

where Φ represents the comoving gravitational potential and $\nabla_{\mathrm{r}} = a^{-1}\nabla_{\mathrm{x}}$.

Combining Equation 1.36 with the derivatives of Equations 1.35 and 1.37, we obtain a second order differential equation for the density contrast δ:

$$\frac{\partial^2\delta}{\partial t^2} + \frac{2\dot{a}}{a}\frac{\partial\delta}{\partial t} = 4\pi G\overline{\rho}\delta = \frac{3H_0^2\Omega_{\mathrm{m}}}{2a^3}\delta, \tag{1.38}$$

which has solutions of the form:

$$\delta(\mathbf{x}, t) = D(t)\tilde{\delta}(\mathbf{x}), \tag{1.39}$$

where $\tilde{\delta}(\mathbf{x})$ is an arbitrary function of spatial coordinate $\mathbf{x}$ and the function $D(t)$ is a solution to the equation:

$$\ddot{D} + \frac{2\dot{a}}{a}\dot{D} = \frac{3H_0^2\Omega_{\mathrm{m}}}{2a^3}D. \tag{1.40}$$

This equation has two linearly independent solutions, one of them increasing with time - $D_+(t)$ - and the other decreasing - $D_-(t)$. Therefore, the increasing solution will dominate at later times, while the other will have died out. Normalizing the solution that increases with time $D_+(t_0) = 1$ (also called the growth factor), we then obtain that the density contrast is:

$$\delta(\mathbf{x}, t) = D_+(t)\delta_0(\mathbf{x}) \tag{1.41}$$

It is interesting to note that in the linear perturbation theory described by the solu-

tion above, the shape of the density fluctuations is independent of comoving coordinates, with only their amplitude increasing with time. The exact form of D_+ depends on the cosmological density parameters as:

$$D_+(a) \propto \frac{H(a)}{H_0} \int_0^a \frac{\mathrm{d}a'}{\left[\frac{\Omega_\mathrm{m}}{a'} + \Omega_\Lambda a'^2 - (\Omega_\mathrm{m} + \Omega_\Lambda - 1)^{3/2}\right]}, \tag{1.42}$$

and, for example, it coincides with the scale factor $a(t)$ for and Einsten-de Sitter Universe (with $\Omega_\mathrm{m} = 1$ and $\Omega_\Lambda = 0$).

1.2.2 Cosmological Density Fluctuations

We will now discuss the question of how to describe the inhomogeneities in the Universe. A cosmological theory cannot aim to exactly determine the complete function $\delta(\mathbf{x}, t)$ for a particular Universe, since this would require exact knowledge about the density field at earlier epochs. Instead, cosmological theories should strive to predict the statistical properties of the fluctuations. This is somewhat analogous to predicting the exact trajectories of atoms in a heated gas - a problem to which the thermodynamic theory answers using statistical properties as well in order to have an overview of the entire picture. We will describe in the following how these statistical properties are quantified in the current cosmological model.

Random Fields

A random field is a generalisation of a stochastic process, encompassing information about the probability distribution of a certain realisation. The density fluctuations $\rho(\mathbf{x}, t)$ observed in the Universe can be considered to be a realisation of a random field. Since there is only one observable Universe, one can estimate the statistical properties of the Universe by looking over many large volumes of space, each of which can be considered as a different realisation of the primordial random field.

Correlation Function and Power Spectrum

For a density field which is homogeneous and isotropic on large scales, the two point correlation function ξ is given by:

$$\xi(|\mathbf{x} - \mathbf{y}|) = \xi(r) = \langle \delta(\mathbf{x}) \delta^*(\mathbf{y}) \rangle, \tag{1.43}$$

with the average density being zero ($\langle \delta \rangle = 0$). As the field δ is assumed to be translationally invariant, the correlation function depends only on the separation $|\mathbf{x} - \mathbf{y}|$ and furthermore, since g is also isotropic, the dependency of the two point correlation function reduces to only $r = |\mathbf{x} - \mathbf{y}|$. Quantifying the density field in Fourier space we have:

$$\delta(\mathbf{x}, t) = \int_{\mathbb{R}^3} \frac{\mathrm{d}^n k}{(2\pi)^n} \tilde{\delta}(\mathbf{k}, t) e^{i\mathbf{k}\cdot\mathbf{x}}, \tag{1.44}$$

where different Fourier modes are represented by $\tilde{\delta}(\mathbf{k}, t)$. By definition, the power spectrum and the correlation function are Fourier transform pairs:

$$P(|\mathbf{k}|) = \int_{\mathbb{R}^n} \mathrm{d}^n x e^{-i\mathbf{x}\cdot\mathbf{k}} \xi(|\mathbf{x}|), \tag{1.45}$$

while respecting the following relation to the two point correlation function:

$$\langle \delta(\mathbf{k}) \delta^*(\mathbf{k'}) \rangle = (2\pi)^n \delta_{\mathrm{D}}(\mathbf{k} - \mathbf{k'}) P(|\mathbf{k}|), \tag{1.46}$$

with n representing the number of spatial dimensions and δ_{D} the $n-$D Dirac delta function.

1.2.3 Gaussian Random Fields

The Fourier transform $\tilde{\delta}(\mathbf{k})$ characterizes the same random field as $\delta(\mathbf{x})$. The Fourier transform of $\tilde{\delta}(\mathbf{k})$ can also be discretized on a grid in $\mathbf{k}$-space, meaning that only discrete wave vectors $\mathbf{k} = \Delta k \mathbf{n}$, where $\mathbf{n}$ is a vector with integer components and $\Delta k = 2\pi/L$, are allowed on scales smaller than the scale length L. Considering a finite volume of scale length L and a fixed time t = constant, we obtain:

$$\begin{aligned} \delta(\mathbf{x}) &= \int_{\mathbb{R}^3} \frac{\mathrm{d}^n k}{(2\pi)^n} \tilde{\delta}(\mathbf{k}, t) e^{i\mathbf{k}\cdot\mathbf{x}} \approx \left(\frac{\Delta k}{2\pi}\right)^n \sum_k \tilde{\delta}(\mathbf{k}) e^{i\mathbf{k}\cdot\mathbf{x}} \\ &= \sum_{\mathbf{k}} \delta_{\mathbf{k}} e^{i\mathbf{k}\cdot\mathbf{x}}, \end{aligned} \tag{1.47}$$

with the Fourier coefficient $\delta_{\mathbf{k}} = (\Delta k/2\pi)^n \tilde{\mathbf{k}}$.

Having knowledge of the power spectrum or the two point correlation function is in general not sufficient to completely characterize the statistical properties of a random field. However, for a particular class of random fields of great cosmological importance, this no longer holds true and they can be uniquely described by $P(k)$ or $\xi(r)$. These are called Gaussian random fields and they are assumed to describe the cosmological density fields at very early epochs in the Universe. Such a Gaussian random field must obey the following two properties:

- The Fourier components $\delta_{\mathbf{k}}$ must be statistically independent
- The probability density for a particular Fourier component $\delta_{\mathbf{k}}$ is Gaussian.

Although not immediately obvious, the second property is in many cases a consequence of the first: refining the $\mathbf{k}$-space grid length by a factor n, the number of grid points in Fourier space have a n^3 higher density (for three dimensions). We can then consider $\delta_{\mathbf{k}}$ as the sum of the Fourier components on the finer grid, and, with random phases for the individual modes, the central limit theorem suggests that $\delta_{\mathbf{k}}$ should tend to behave approximately Gaussian.

1.2.4 The Dark Matter Field

Since the detection of the anomalous galaxy rotation curves in 1933, the existence of dark matter has been confirmed through other methods, although it is still eluding direct detection. The properties of large scale scale structure are very sensitive to the quantity and properties of dark matter, the density fluctuations in the matter density field discussed so far being significantly modified by the presence of the dark matter density field.

The Initial Power Spectrum

The primordial spectrum of density fluctuations is predicted by a wide range of inflationary models to follow a Gaussian distribution. Once the initial power spectrum is specified and we have a theory that describes the evolution of the fluctuations, we have a complete picture of the density field, as long as we remain in the linear regime. This Gaussianity is preserved until the different Fourier modes become coupled. It might initially seem that this power spectrum can be an arbitrary function, but as we will show next, this is not really the case.

In the early history of the Universe there is no particular length scale preferred, as density perturbations are much larger than the horizon. This is a consequence of a prediction of inflationary models, where scales usually cross the horizon sufficiently quickly that there is not enough time for large changes in the physical conditions that govern the size of the perturbations. The primordial power spectrum $P_0(k)$ must be a mathematical function that does not depend on a characteristic scale, a power law:

$$P_0(k) \propto k^{n_s}, \tag{1.48}$$

where n_s is called the spectral index. It has been argued (see Harrison 1970; Peebles & Yu 1970; Zeldovich 1972, and others) based on scaling relations that the spectral index n_s should be close to unity and therefore this particular power spectrum is called *Harrison-Zeldovich-Peebles* spectrum. Indeed, measurements show that it is slightly smaller than, but close to unity, with $n_s = 0.968 \pm 0.006$ (see Planck Collaboration et al. 2016), as predicted by inflationary models Such a power spectrum requires that the perturbations that enter the horizon are scale invariant, having the same amplitude. The amplitude A of the primordial power spectrum cannot be predicted by theory and must be constrained by observations:

$$P_0(k) = A\, k^{n_s}, \tag{1.49}$$

growing with time as given by:

$$P(k,t) = D_+^2(t)\, A\, k^{n_s} \tag{1.50}$$

The Transfer Function

As Equation 1.49 only holds for the matter dominated era and disregards any pressure terms in the derivation of D_+, we must correct for the evolution of density perturbations in the radiation-dominated era. The evolution of Fourier density modes is different in the radiation dominated era and there are some which are larger than the horizon, entering at subsequent stages. We can account for the pressure-less Newtonian case with:

$$P_0(k) = A\, T^2(k)\, k^{n_s}, \tag{1.51}$$

where $T(k)$ is called the transfer function. The shape of the transfer function is particularly sensitive to the properties of dark matter, especially to the thermal velocities of its constituents. Hot Dark Matter is composed of relativistic particles when matter and radiation had the same density, while Cold Dark Matter had non-relativistic velocities. There are significant differences in the structure formation depending on the quantity of hot or cold dark matter. Hot dark matter has the tendency of erasing small scale structure, suppressing the power spectrum for large k and enabling the formation of the largest structures first, followed later by fragmentation into smaller components (e.g. galaxies). There is a host of observational evidence that supports a Universe without much hot dark matter, for example the fact that we observe small structures in the very early Universe, the bottom-up, hierarchical scenario of structure formation. For a CDM - dominated Universe, the transfer function can be well approximated for small scales by fitting functions (e.g. Bardeen et al. 1986; Eisenstein & Hu 1998).

Nonlinear Evolution of Density Perturbations

Although linear perturbation theory is sufficient to give an overall idea about the evolution of density perturbations, it cannot describe accurately the growth of structures such as galaxy clusters. Even by solving the equations to higher orders, thus enabling us to follow the density perturbations to larger values of δ, the large mathematical effort required does not really justify the improvement. Instead, large numerical simulations are used, starting from Gaussian random fields and following their evolution, evolving each realisation with time. The statistical properties of the resulting structures can then be used for investigating fitting formulae for the non-linear power spectrum (e.g. Peacock & Dodds 1996; Smith et al. 2003).

1.2.5 The Model of Spherical Collapse

A very useful non-linear model that has analytic solutions is the model of spherical collapse, an over-dense sphere that behaves in precisely the same way as a closed, small Universe. The density perturbation doesn't need to be a uniform sphere, since any perturbation with spherical symmetry will evolve at a given radius the same way as a uniform sphere containing the same amount of mass. The mean density inside

the sphere compared to the mean cosmic density $\overline{\rho}(t)$ is given by:

$$\rho(t) = [1 + \delta(t)]\,\overline{\rho}(t). \tag{1.52}$$

Although this model is not very realistic, it's solutions still give a good idea of the formation and evolution of dark matter haloes at length scales comparable to those of galaxy clusters. Due to the higher mean density of the sphere when compared to the cosmic density, there will be an increased gravitational force that will tend to slow down the sphere's expansion. With time, this positive feedback loop will stop the expansion for certain initial densities, with the sphere entering into recollapse. Since the sphere isn't perfectly homogeneous and its constituent particles deviate from perfectly radial orbits, the recollapse will not end in a point. The particles in the sphere will reach the virial equilibrium forming a so called *halo*, with the sphere having a virial radius $r_{\rm vir}$ half as large as the one at maximum expansion. The value of the mean density inside the sphere at the time of virialisation $t_{\rm vir}$ is approximated by:

$$\langle\rho\rangle = (1 + \delta_{\rm vir})\,\overline{\rho}(t_{\rm vir}),\ \text{where}\ (1 + \delta_{\rm vir}) \simeq 178\,\Omega_{\rm m}^{-0.7} \tag{1.53}$$

This result is at the basis of the statement that a virialized region is a sphere with an average density 200 times larger than the cosmic density at the epoch of collapse, with r_{200} corresponding to the radius and M_{200} to the mass of such a sphere. It can be shown within this framework that mass perturbations with a linear density contrast $\delta(t_0) \geq 1.7$ are virialized today.

1.2.6 The Number Density of Dark Matter Halos

We can now use the model of spherical collapse to estimate the number density of collapsed halos as a function of mass and time, since the properties of the linear density field can now be directly related to the mass and redshift for halos. One of the first mass functions was found by Press & Schechter (1974):

$$f(\sigma) = \frac{M}{\rho_0}\frac{{\rm d}n}{\ln\sigma^{-1}} = \sqrt{\frac{2}{\pi}}\frac{\delta_c}{\sigma}e^{-\frac{\delta_c^2}{2\sigma^2}}, \tag{1.54}$$

where σ represents the variance of mass in a given volume (see Eq. 7 of Press & Schechter (1974)) of the smoothed primordial Gaussian field and $\frac{{\rm d}n}{{\rm d}M}$ stands for the differential comoving number density of halos of mass M. There has been considerable improvement in the empirical determination of the mass function, with a remarkably simple fitting formula being given by (Jenkins et al. 2001):

$$f(\sigma) = 0.315\,e^{-|\ln\sigma^{-1}+0.61|^{3.8}}, \tag{1.55}$$

which provides excellent fits for a wide variety of cosmological models, including ΛCDM. A comparison between the Press-Schechter halo mass function and the more recent results of Peacock (2007) can be seen in Figure 1.2.

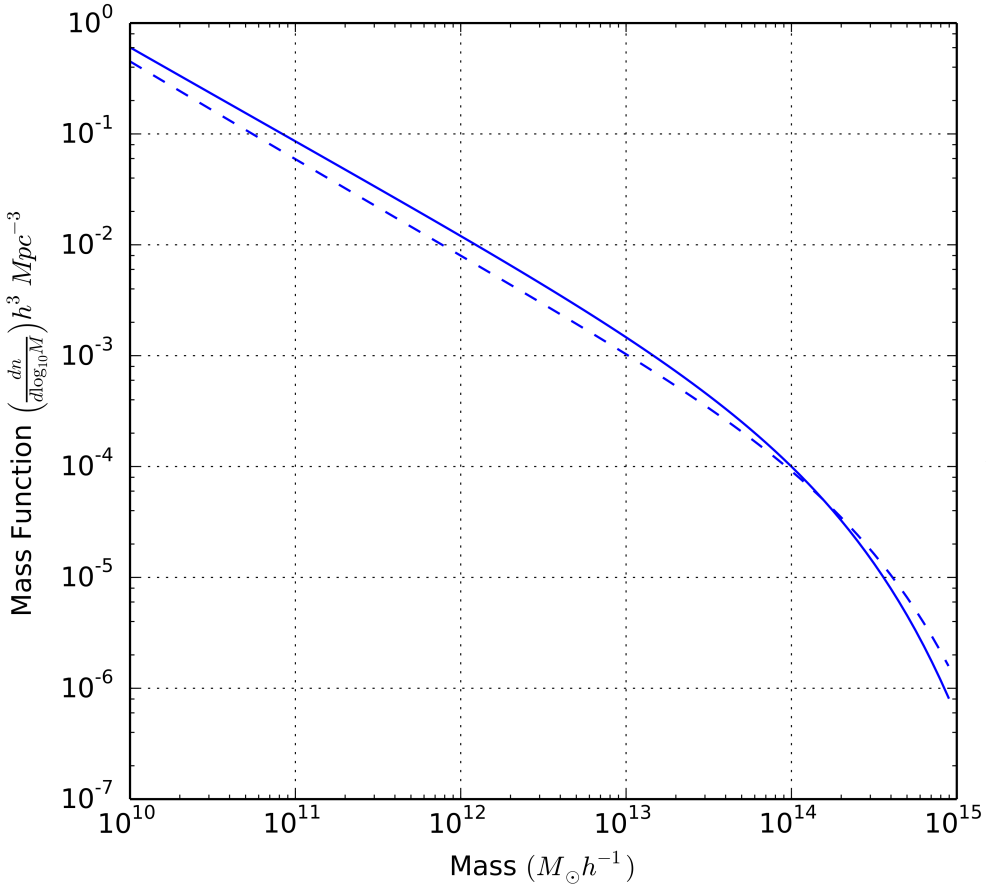

Figure 1.2: The halo mass function in a standard ΛCDM Universe, computed using different methods at a redshift of $z = 0.0$ (Murray et al. 2013). The solid line represents the Press-Schechter mass function (see Equation 1.54), while the dashed line traces the Peacock approximation (Peacock 2007). Press-Schechter slightly overestimates the number of small halos, while underestimating the number of massive ones.

1.2.7 The Lens Bias

If Dark Matter Halos would form independently of the underlying density fluctuations and only under the influence of the gravitational force, then their number density would be an unbiased tracer of the dark matter density fluctuation. Since the spherical collapse model predicts that the probability of forming a halo depends on the initial density field, this means that large scale density fluctuations would act to enhance the formation of dark matter halos. The spatial distribution of galaxies and their halos is tracing the mass distribution of dark matter with a constant bias. The ratio between the 2-point correlation functions of halos of a given mass and that of the underlying dark matter distribution is defined as the bias of dark matter halos.

For the halo bias factor $b_{\rm l}$ we adopt the approximation of Seljak & Warren (2004):

$$b_{\rm l}(x = M/M_{\rm nl}(z)) = 0.53 + 0.39x^{0.45} + \frac{0.13}{40x + 1} + 5 \times 10^{-4}x^{1.5} \tag{1.56}$$

where nonlinear mass $M_{\rm nl}$, is defined as the mass within a sphere for which the root mean square fluctuation amplitude of the linear field is 1.68.

1.2.8 The NFW Profile

The radial mass distribution of dark matter halos is very well fitted independently of their mass, within the virial radius by the Navarro et al. (1997) density profile:

$$\rho(r) = \frac{\delta_{\rm crit}\,\rho_{\rm crit}(z)}{(r/r_{\rm s})(1 + r/r_{\rm s})^2}, \tag{1.57}$$

where $\rho_{\rm crit}(z)$ is the critical density at redshift z, $r_{\rm s}$ is a characteristic radius of the halo defined in terms of the concentration parameter $c \equiv \frac{r_{200}}{r_{\rm s}}$, and $\delta_{\rm crit}$ is defined by:

$$\delta_{\rm crit} \equiv \frac{200}{3}\frac{c^3}{\ln(1 + c) - c/(1 + c)}. \tag{1.58}$$

1.2.9 The Halo Model

Considering the large structures in the Universe as being made of distinct halos of different sizes and masses has a series of advantages. Although based on assumptions which turn out not to be valid following a detailed analysis, the halo model turns out to be a remarkably good approximation to results obtained using more accurate methods such as simulations. For a complete picture of the large scale structure, we require three main components, which were already outlined in previous sections:

1. The halo mass function, that describes the distribution of halo masses
2. The power spectrum, which models the spatial distribution of halos
3. The mass profile of halos

Given NFW halos of abundance n_g, with a mass function 1.55 and clustered according to the halo bias, the galaxy power spectrum can be expressed as the sum of two terms:

$$P_g(k) = P_g^{1h} + P_g^{2h} \tag{1.59}$$

where P_g^{1h} represents the sum of the contributions from galaxies within the same halo, which dominate small scales, while P_g^{2h} representing the sum of the contributions from galaxies in different halos, which dominate large scales. We assume that if a halo hosts only one galaxy, then it is situated in the center of the halo, while if the halo contains multiple galaxies, they are distributed statistically following the halo mass profile.

Using the linear CDM power spectrum, one can calculate the 1-halo term P_g^{1h} and the 2-halo term P_g^{2h} to be:

$$P_g^{1h}(k) = \frac{1}{(2\pi)^3 n_g^2} \int \mathrm{d}M n_{\mathrm{halo}}(M) \langle N_g(N_g - 1)|M\rangle \, |y(k, M)|^p \,, \tag{1.60}$$

and

$$P_g^{2h}(k) = P_{\mathrm{lin}}(k) \left[\frac{1}{n_g} \int \mathrm{d}M n_{\mathrm{halo}}(M) \langle N_g|M\rangle b_1(M) \, y(k, M) \right]^2 , \tag{1.61}$$

where $b_1(M)$ is the halo bias factor detailed above and $y(r, M)$ the normalised Fourier transform of the halo density profile:

$$y(r, M) = \frac{1}{M} \int 4\pi r^2 \mathrm{d}r \, \rho(r, M) \frac{\sin(kr)}{kr}. \tag{1.62}$$

The value of the parameter p depends on the spatial distributions of galaxies in the halo. If we only have one pair in the halo, then the term $y(k, M)$ occurs only once, hence $p = 1$. For the limit of many pairs in the halo, the location of the central galaxy can be neglected and we can assume that each galaxy contributes a factor of $y(k, M)$, therefore $p = 2$.

The Fourier transform of $P_g(k)$ is the two-point correlation function of galaxies.

Two-dimensional Correlation Function for Galaxies

Up to this point we have dealt only with the 3-dimensional distribution of galaxies in space. The existence of a 3-D correlation implies the existence of an angular correlation. Using astronomical observations it is not easy to measure this since it requires precise 3-dimensional data for all galaxies. Redshift information is not only much more imprecise relative to the measurement of 2-D positions on the sky, but also subjected to other effects, such as peculiar velocities and other distortion effects. We can however still estimate the galaxy correlation function by using data about the overall redshift distribution.

Letting the number density fluctuation of galaxies to be denoted by $\delta n \, (f(w)\boldsymbol{\theta}, w)$ and $g(w)$ to represent a selection function in redshift, then the observed number density

fluctuation on the sky is given by:

$$\delta n_{\rm G}(\boldsymbol{\theta}) = \int {\rm d}w\, g(w)\, \delta n\ (f(w)\boldsymbol{\theta},\ w)\,. \tag{1.63}$$

The angular correlation function $w(\boldsymbol{\theta})$ is then given by:

$$w(\boldsymbol{\theta}) = \langle \delta n_{\rm G}(\boldsymbol{\theta'})\, \delta n_{\rm G}(\boldsymbol{\theta} + \boldsymbol{\theta'})\rangle, \tag{1.64}$$

where $\delta n_{\rm G}(\boldsymbol{\theta})$ is the galaxy over- or under-density at position θ, and $\theta = |\boldsymbol{\theta}|$. The following projection integral can be used to relate w to the galaxy number density contrast in real space:

$$w(\theta) = \int_0^\infty {\rm d}w\, g(w) \int_0^\infty {\rm d}w'\, g(w')\, \langle \delta_n(f_K(w)\boldsymbol{\theta'}, w)\, \delta_n\,(f_K(w')(\boldsymbol{\theta} + \boldsymbol{\theta'}),\ w')\rangle. \tag{1.65}$$

If the real-space correlation function does not evolve over the look-back time interval where $g(w)$ is non-zero, and by defining the mean and difference distance with:

$$\overline{w} := \frac{w + w'}{2} \tag{1.66}$$

and

$$\Delta w := w - w', \tag{1.67}$$

we obtain the angular correlation function:

$$w(\theta) = \int_0^\infty {\rm d}\overline{w} \int_{-\infty}^\infty {\rm d}\Delta w\, g\left(\overline{w} + \frac{\Delta w}{2}\right) g\left(\overline{w} - \frac{\Delta w}{2}\right) \xi_{\rm g}\left(\sqrt{f_K^2(\overline{w})\theta^2 + \Delta w^2}, \overline{w}\right) \tag{1.68}$$

where the second argument of $\xi_{\rm g}$ represents the time at which the real-space correlation function is measured and provided that $g(w)$ is a slowly changing function. Using the fact that $\xi_{\rm g}$ is non zero only for sufficiently small Δw, we can then replace the arguments of g-functions by w, arriving at the famous *Limber equation*:

$$w(\theta) = \int {\rm d}\overline{w}\, g^2(\overline{w}) \int {\rm d}\Delta w\, \xi_{\rm g}\left(\sqrt{f_K^2(\overline{w})\theta^2 + \Delta w^2}, \overline{w}\right), \tag{1.69}$$

which relates 2-D and 3-D correlation functions. However, it is important to note that one must know the selection function $g(w)$ for a proper interpretation of the angular correlation function.

A Fourier-space version of the Limber equation can also be derived, relating the 2-D and 3-D power spectra:

$$P_{\rm 2D}(l) = \int {\rm d}^2\theta\, w(\boldsymbol{\theta})\, e^{{\rm i}\boldsymbol{l}\cdot\boldsymbol{\theta}} = \int {\rm d}w\, \frac{g^2(w)}{f_{\rm K}^2} P_{\rm 3D}\left(\frac{l}{f_{\rm K}(w)}, w\right), \tag{1.70}$$

thus relating the power at angular scale of $2\pi/l$ with the 3-D power at length scale $f_{\mathrm{K}}(w)\,(2\pi/l)$ integrated over w.

A useful property of the Limber equation is that if the 3-D angular correlation function is a power law, $\xi(r) = (\frac{r}{r_0})^{-\gamma}$, then w is also a power law:

$$w(\theta) = \theta^{1-\gamma} r_0^{\gamma} \frac{\Gamma(1/2)\,\Gamma(\gamma/2 - 1/2)}{\Gamma(\gamma/2)} \int_0^{\infty} \mathrm{d}\overline{w}\, p^2(\overline{w})\, \left[f_{\mathrm{K}}(\overline{w})\right]^{1-\gamma}, \tag{1.71}$$

where Γ is the Euler Gamma function. Therefore, the slope γ of ξ is connected to the slope δ of w through $\delta = \gamma - 1$, and the amplitude:

$$A_{\theta} = r_0^{\gamma} \frac{\Gamma(1/2)\,\Gamma(\gamma/2 - 1/2)}{\Gamma(\gamma/2)} \int_0^{\infty} \mathrm{d}\overline{w}\, p^2(\overline{w})\, \left[f_{\mathrm{K}}(\overline{w})\right]^{1-\gamma}. \tag{1.72}$$

This means that by measuring the amplitude A_{θ} of the correlation function we can estimate the correlation length r_0 of the real-space correlation function as long as we know the distribution $g(w)$.

1.3 Clusters of Galaxies

1.3.1 Properties

Our current paradigm of large scale structure formation in the Universe suggests that small density fluctuations in the very early Universe are amplified under the influence of gravity and eventually create massive structures dominated by dark matter. The densest regions of the resulting large scale structure correspond to galaxy clusters, and are thought to form through a hierarchical sequence of mergers and accretion of smaller systems (Kravtsov & Borgani 2012; Giodini et al. 2013). These objects contain from tens to thousands of galaxies and are the largest gravitationally bound structures in the Universe.

Although galaxies represent the most familiar part of a galaxy cluster, they only represent a few percent of the mass fraction for a typical cluster (Gonzalez et al. 2013). The bulk of the barionic matter in massive galaxy clusters is made of diffuse plasma residing in between the cluster galaxies, the intracluster medium (hereafter ICM). The properties of the the hot ICM and individual galaxies are somewhat correlated even if they are not directly connected. The average mass of the ICM is about ten times larger than the total stellar mass, although this depends on the mass of the galaxy cluster, with smaller mass systems having a larger quantity of stars relative to the ICM mass, ranging from $M_{\rm stars}/M_{\rm ICM} \approx 0.2$ to 0.05, for cluster masses between $M_{500} \approx 10^{13}{\rm M}_{\odot}$ and $M_{500} \approx 10^{15}{\rm M}_{\odot}$ (see Kravtsov & Borgani (2012) and Fig.1.3). However, most of the mass of a galaxy cluster resides in the dark matter halo, which makes up for about 80% of the total mass, thus completely dominating the system gravitationally.

An assembly of more than 5-6 galaxies is classified as a galaxy group, tens/hundreds represent a cluster and thousands make up a rich cluster. The *richness* parameter of a cluster represents the total number of galaxies above the background values that fulfil certain criteria in order to be considered as part of the system. Many such criteria are employed, usually including galaxies that are of a certain luminosity and within a certain distance form the cluster centre. Unfortunately the freedom of defining the richness parameter also means that various types of studies have often issues comparing their richness parameters if defined and measured in a different way. There are a number of differences between galaxies residing in clusters and field galaxies, for example in morphology (there are more elliptical and lens-shaped galaxies than spirals within clusters), colour (spirals and irregular galaxies tend to be redder on average than field galaxies), total gas content (spiral galaxies close to cluster centres tend to have less neutral hydrogen than field spirals), etc.

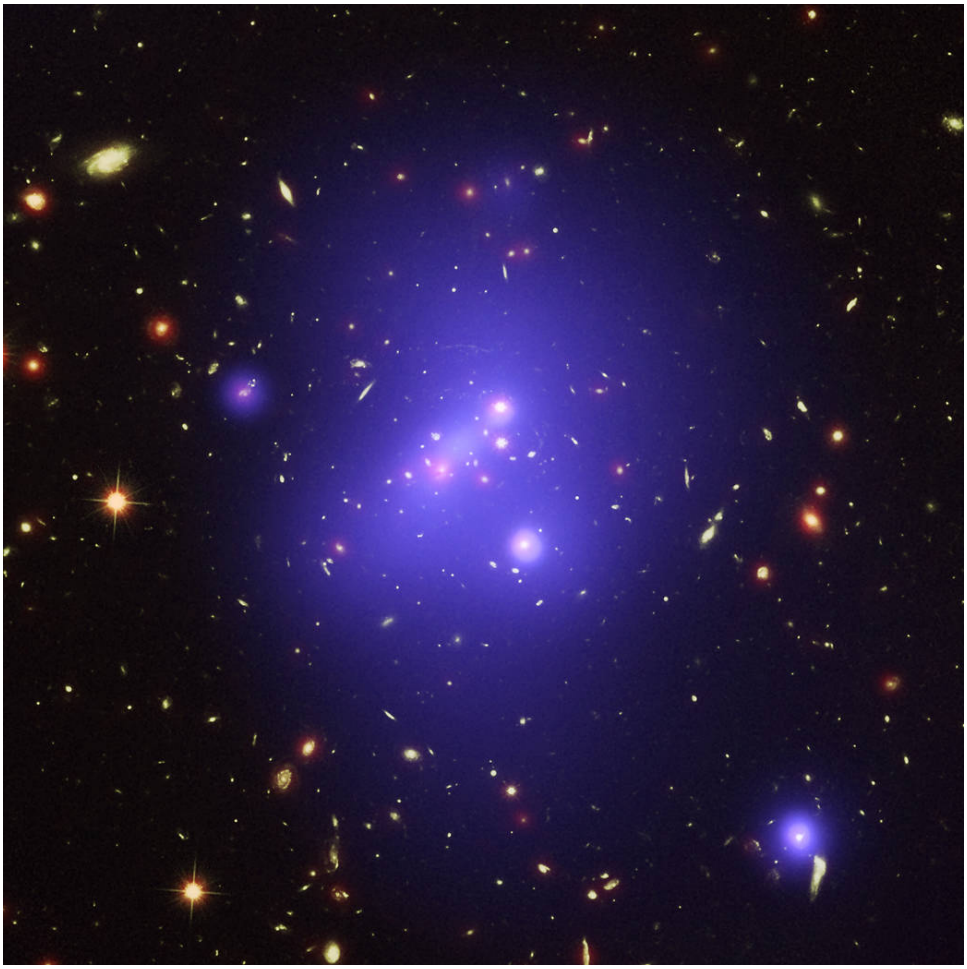

Figure 1.3: A multi-wavelength image of one of the most massive high-redshift galaxy cluster known, IDCS J1426.5+3508 (IDCS 1426 for short), with blue representing in X-rays from the Chandra X-ray Observatory, green visible light from the Hubble Space Telescope, and red the infrared light from the Spitzer Space Telescope. It is located at $z = 1.75$ and has a mass of $M_{500,Y_X} = 2.6^{+1.5}_{-0.5} \times 10^{14} M_\odot$, sitting at the upper end of the galaxy cluster mass function (Brodwin et al. 2016). NASA public release image.

For simplicity of mass modelling we assume the galaxy clusters to have a spherically symmetric shape. This assumption is nevertheless inaccurate, introducing small systematic errors since galaxy clusters exhibit in reality triaxiality. For some applications of gravitational lensing to the study of galaxy clusters, triaxiality effects can bias the mass measurement by even 40% and the concentration c by a factor of 2 (Corless & King 2007). Generalising the spherical NFW profile to include triaxial effects changes Eq. 1.57 to:

$$\rho(r_{3\mathrm{ax}}) = \frac{\delta_c \rho_c(z)}{r_{3\mathrm{ax}}/r_s(1 + r_{3\mathrm{ax}}/r_s)^2}, \tag{1.73}$$

where r_{3ax} represents a triaxial radius:

$$r_{3ax}^2 = \frac{X^2}{a^2} + \frac{Y^2}{b^2} + \frac{Z^2}{c^2}, \ (a \leq b \leq c = 1), \tag{1.74}$$

with a, b and c representing the semi-minor, semi-intermediate and semi-major axes respectively of the iso-density ellipsoid with $r = 1$, while coordinates (X, Y, Z) lie along the principal axes of the cluster.

However, for studies of cluster ensembles this effect becomes smaller with the number of clusters averaged, since mixing many cluster shapes together tends to produce a spherical result. As the signal-to-noise ratio for weak lensing measurements is low, it is usually difficult to even distinguish between simple parametric models for the mass density such as SIS and NFW at certain radial distances (Corless & King 2007; Feroz & Hobson 2012).

1.3.2 Detection

Observational studies of galaxy clusters have now expanded into a broad and complex field, often making use of multi-wavelength data. Clusters can be detected and investigated using a large variety of methods mostly tied to their main matter constituents:

- searching for overdensities in the number of galaxies (sensitive to projection effects in the absence of any redshift information). Assumptions about the distribution of galaxies in clusters and their colors can be used to improve search algorithms
- lensing of background galaxies through observations of strong lensing arcs or shear measurements
- inverse Compton scattering of CMB photons on hot intra-cluster gas electrons (the Sunyaev-Zeldovich effect)
- radio haloes produced by synchrotron emission of electrons travelling through galaxy cluster magnetic fields
- thermal and non-thermal bremsstrahlung emission of the hot intra-cluster gas and respectively relativistic electrons in the X-ray and γ-ray wavebands

1.3.3 Scaling Relations

In order to constrain cosmological parameters using the cluster mass function, a reliable and observationally cheap way of determining the total mass for large samples of clusters is necessary. Employing robust and well studied relations between easily

measurable quantities and the total cluster mass is therefore an excellent method of addressing this problem.

The scaling relation that connect various quantities and the total cluster mass are the consequence of the physics of halo formation and evolution. There are many scaling relations available in the literature, connecting for example the X-ray luminosity and temperature of the intra-cluster gas, total mass and temperature, luminosity, cluster richness, concentration and mass etc.

Considering simple models where gravity is the only dominant force, Kaiser (1986) has shown it leads to the so-called self similar models, with scaling relations following power laws (i.e. $f(x) = x^n$). Mathematically speaking exact self similar functions reflect a property of fractals, with the system being identical to itself for each rescaling length. Nature however exhibits such a property only for statistical quantities within certain scale ranges (Giodini et al. 2013).

Especially in the case of very large cluster samples, such as the ones offered by future surveys such as Kilo Degree Survey (KiDS, de Jong et al. 2013), Euclid (Laureijs et al. 2011), Subaru Hyper Suprime-Cam (Takada 2010), Large Synoptic Survey Telescope (LSST, Ivezic et al. 2008), Dark Energy Survey (DES, The Dark Energy Survey Collaboration 2005), etc., which will provide thousands of galaxy cluster candidates (see Fig. 1.4), obtaining individual mass estimates will prove to be prohibitively demanding observationally. Inexpensive proxies based on the global optical properties of clusters play and important role for several reasons: the necessary data is easily acquired, even for high redshift cluster samples, and they are applicable to the lower mass range of clusters where there are not enough member galaxies in order to obtain a dynamical mass estimate.

The richness parameter is usually defined as the number of observed galaxies within a certain radius and with specific colour and brightness properties. Using multi-band data lowers the background correction errors and improves the purity of the sample, tightening the mass-richness relation significantly. Data inhomogeneity and incongruent definitions employed by different studies limit somewhat the applicability of the mass-richness relation to comparing results within the literature, especially since it is often the case that the cluster samples are not having significant overlap (see Fig. 1.5). It follows that in the absence of a better way to convert different richness proxies into each other, the optimal way to obtain the maximum information for the least amount or observational effort is the self-calibration of each study on a subset of clusters.

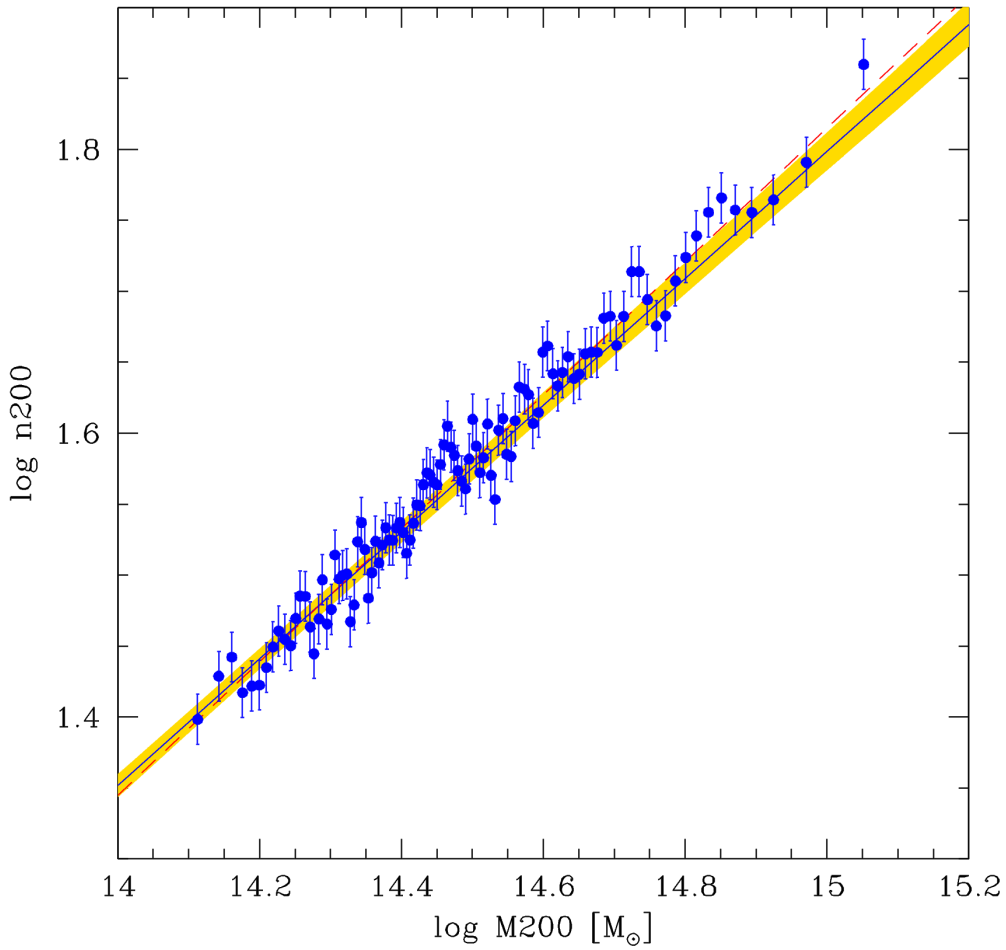

Figure 1.4: Richness-mass scaling for the simulated Pann Stars 1 combined with Euclid-like data. The dashed line corresponds to the input relation, while the solid line marks the regression line fitted on observed data, with the shading representing the 1-σ error on the fit. The data points represent bins of 201 clusters, individual clusters not being used in the fit. Figure from Andreon & Bergé (2012).

The Poisson-scatter in the mass-richness relation can be reduced by using more optimal estimators (Gladders et al. 2007; Rozo et al. 2009a); for example Rozo et al. (2009b; 2011) used a matched filter method coupled with an optimized iterative measure of the cluster extent (see also Rykoff et al. 2012; Giodini et al. 2013). Overall, after careful statistical analysis and proper implementation of the methods, Andreon & Hurn (2010) have shown that optical richness proxies have similar prediction performance for the total mass estimation when compared to scaling relations based on the X-ray luminosity.

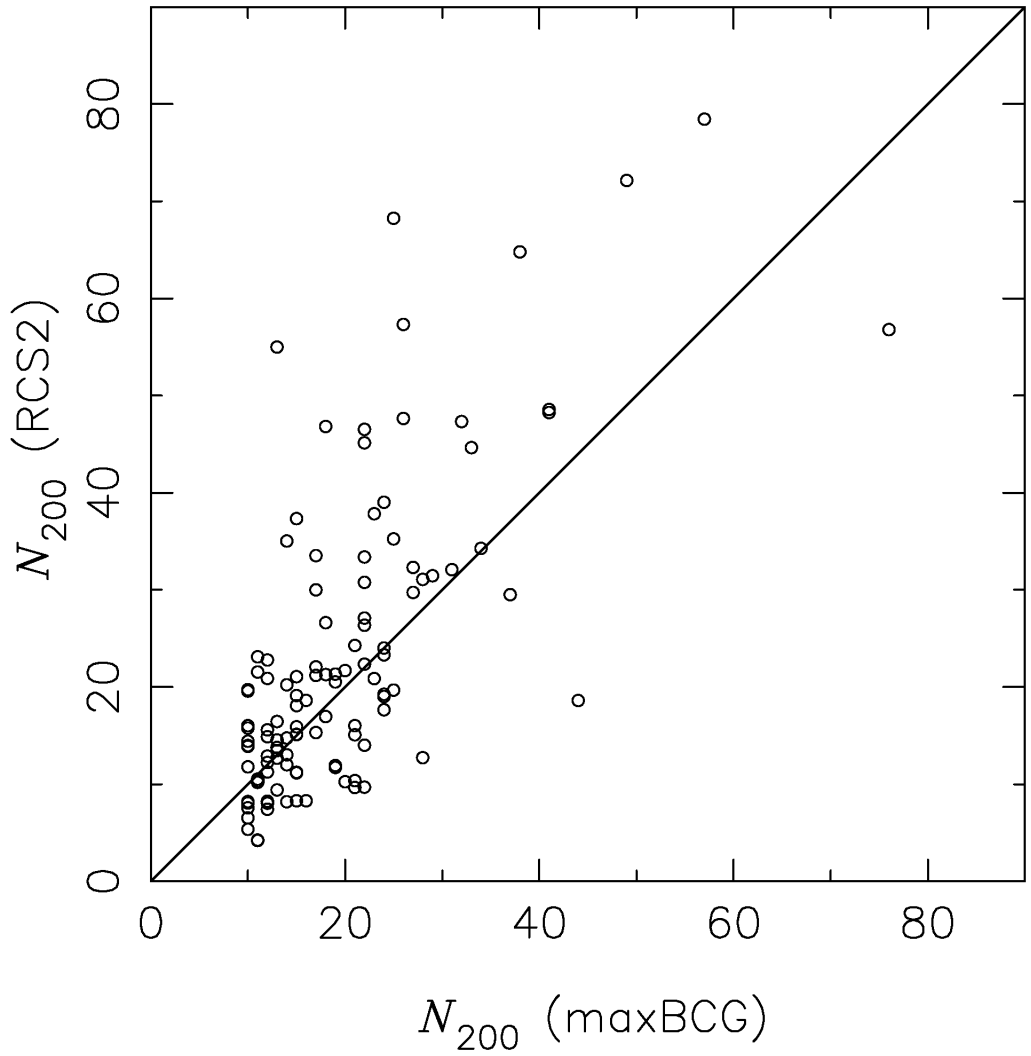

Figure 1.5: Comparison of the cluster richnesses (N200) of 114 matched clusters between maxBCG (Koester et al. 2007) and RCS2 (van Uitert et al. 2016), with the solid line tracing the one-to-one relationship. Figure from van Uitert et al. (2016).

1.3.4 Significance

Dark matter halos represent biased tracers of the underlying dark matter distribution. Their formation is being seeded by high amplitude density variations in the primordial density field, thus giving birth to a correlation between the dark matter halo mass and clustering amplitude (Kaiser 1984). As the formation of dark matter haloes is driven mostly by self gravitational interaction, there is practically no dependence on the physics of the relatively minor baryonic component. The clustering of galaxies thus provides a tool for deriving properties of the halos in which they form (Zehavi et al. 2005; van den Bosch et al. 2003; Tinker 2005; Abazajian et al. 2005; Zheng et al. 2007; Yoo et al. 2009), and coupled with galaxy redshift measurements, a window into

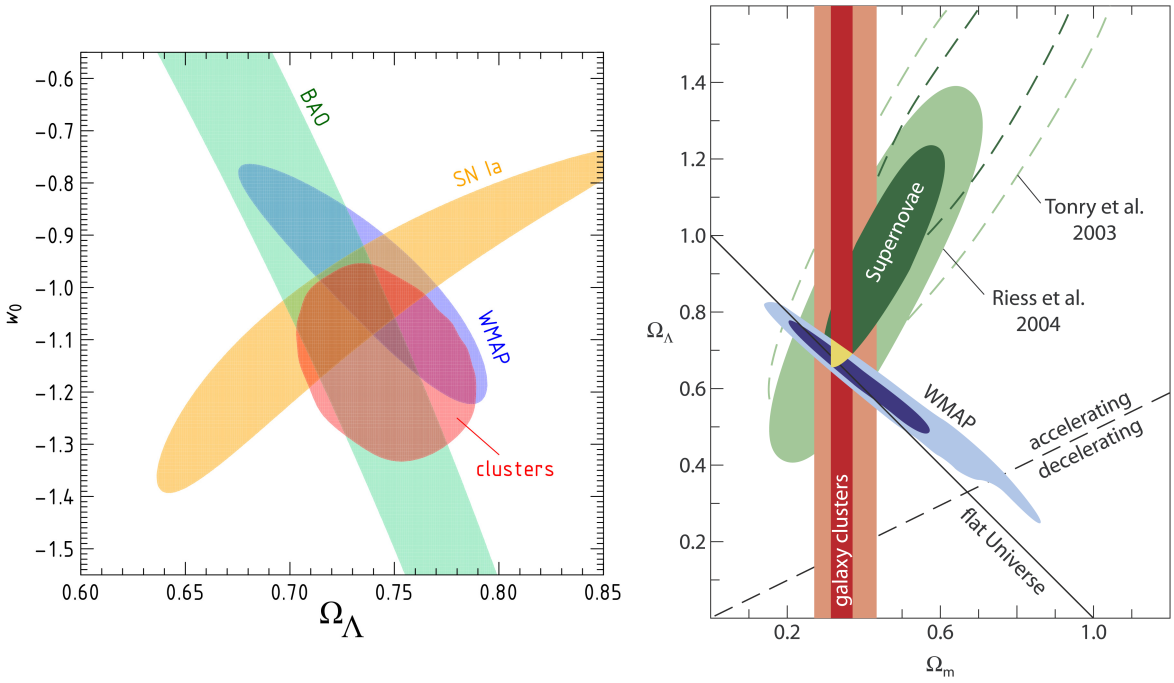

Figure 1.6: Constraints of cosmological parameters. Left: Constraints in the $\Omega_\Lambda - w_0$ plane at the 1σ level - type Ia supernovae from Davis et al. (2007), BAO from Percival et al. (2007), WMAP from Komatsu et al. (2009) and clusters from Vikhlinin et al. (2009). Figure adapted from Vikhlinin et al. (2009). Right: Current observational constraints from type Ia supernovae (Tonry et al. 2003; Riess et al. 2004), CMB (Spergel et al. 2003) and galaxy clusters (Schuecker et al. 2003) on the cosmic density of all matter including Ω_Λ and Ω_m relative to the density of a critical-density Universe. The dark red region for the galaxy cluster determination corresponds to a 2σ confidence when assuming good knowledge of all other cosmological parameters, and the light red region assumes a minimum knowledge. For the supernovae and WMAP results, the inner and outer regions correspond to 1σ and 2σ certainties, respectively. Figure credit: European Southern Observatory.

the evolution through time of the large scale structure of the Universe.

Galaxy clusters also represent important tools for investigating cosmological models, for example by comparing the numbers of galaxy clusters observed per unit volume with predictions of the halo mass function (see Eq. 1.55, Fig. 1.2, Fig. 1.6, Jenkins et al. 2001 and Tinker et al. 2008; 2010). This particular example is very sensitive to the normalisation of the primordial matter power spectrum of density fluctuations and the proportion of matter content in the Universe, σ_8 and Ω_m. Massive high redshift galaxy clusters play a proportionally higher role for constraining such parameters since although they are rare at any redshift, few exist earlier in the history in the universe.

While the low redshift region of (virialised) galaxy clusters has been very well studied, with mass-observable relations being reasonably well calibrated, constraining these relations at higher redshifts is challenging, with some of the (X-ray data based) studies published giving sometimes contradictory results on the evolution of

scaling relations involving parameters depending on the intra-cluster medium properties (see e.g. Ettori et al. 2004; O'Hara et al. 2006; Kotov & Vikhlinin 2005; Pacaud et al. 2007; Reichert et al. 2011). The observational difficulties associated with obtaining well defined high redshift galaxy cluster samples strongly limit the constraints achievable on the departure from self-similar model predictions or redshift evolution.

CHAPTER 2

Gravitational Lensing

If not otherwise specified, all equations in this chapter are taken from Bartelmann & Schneider (2001).

According to the Theory of General Relativity, light rays are deflected when they propagate through a gravitational field. Gravitational lensing is broadly divided into two main categories, depending on the observational consequences. Strong gravitational lensing produces multiple images, arcs and even complete rings (also called Einstein rings). Meanwhile, the effects of Weak Gravitational Lensing are much more subtle and require statistical methods to be studied, since they are impossible to measure in a single background source. In the next sections we will concentrate on the latter.

2.1 Outline of Gravitational Lensing

Figure 2.1 shows the outline of a typical gravitational lensing system. A source located in the source plane is considered to be located at an angular diameter distance D_s from the observer, while the mass concentration (lens) at a distance D_d. The distance between the source and the deflector is given by D_ds. The observer sees the light deflected by the mass concentration of the lens (located in the lens plane). An optical axis intersects and is perpendicular to the source and lens planes, connecting the observer and the center of the lens. The source is located in the source plane at position $\vec{\eta}$. Since the distances between the lens, source and observer are much larger than the size of the lens, we can replace the normally continuously bending light ray by two straight lines. This approximation is generally true in astrophysical applications, since galaxy clusters have sizes of the order of a few Mpc, still considerably smaller than the D_s, D_ds, D_d distances, which are usually of the order of hundreds or thousands of Mpc. The distance in the lens plane between the lens and the intersection of

the light ray with the lens plane is given by $\vec{\xi}$, $\vec{\beta}$ is the position that the source would have been observed at without the deflection caused by gravitational lensing, while $\vec{\theta}$ is the observed source position. All of the angles can be assumed to be small.

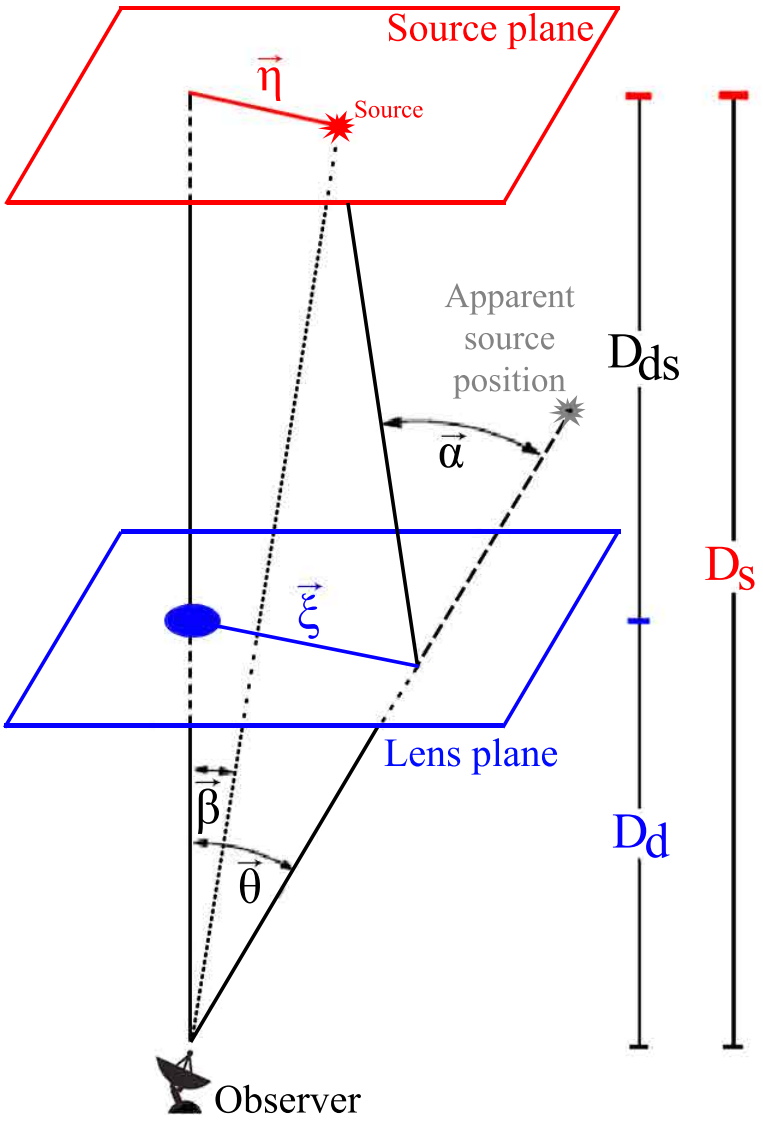

Figure 2.1: Typical gravitational lensing system geometry outline.

From Figure 2.1 we then have:

$$\vec{\eta} = \vec{\theta} D_s - \vec{\alpha}' \vec{\xi} D_{ds}. \tag{2.1}$$

Making use of the definition of the angular diameter distance (see Equation 1.4) and replacing the distance vectors $\vec{\theta}$ and $\vec{\xi}$ in both the lens and the source planes with the

angular variables β and θ, we can then transform Equation 2.1 to:

$$\vec{\beta} = \vec{\theta} - \frac{D_{\rm ds}}{D_{\rm s}}\vec{\alpha'}(D_{\rm d}\,\vec{\theta}) = \vec{\theta} - \vec{\alpha}(\vec{\theta}), \tag{2.2}$$

where in the last step we have defined the scaled deflection angle as:

$$\vec{\alpha}(\vec{\theta})) = \frac{D_{\rm ds}}{D_{\rm s}}\vec{\alpha'}(D_{\rm d}\vec{\theta}). \tag{2.3}$$

Following the consequences of Equation 2.2, we find that there can be multiple solutions, each of them representing another image of the source. Considering a spherically symmetric mass M, the deflection of a light ray passing through the exterior and given that the ray's impact parameter ξ is much larger that the Schwarzschild radius ($R_{\rm s}$) of the mass, $\xi \gg R_{\rm s} = 2GMc^{-2}$, we can then write the deflection angle α' as predicted by General Relativity:

$$\alpha' = \frac{4GM}{c^2\xi}. \tag{2.4}$$

The value of α' is twice as large as the value obtained with a Newtonian treatment of the problem, which combined with the condition that $\xi \gg R_{\rm s}$ implies that the Newtonian gravitational field strength is small, $\frac{\phi_{\rm N}}{c^2} \ll 1$. Since the field equations of General Relativity can be linearised if the gravitational field is weak, the trajectories of light rays in the vicinity of the deflecting masses (lenses) can be approximated with straight lines. A mass distribution for which this condition is satisfied is called a geometrically thin lens. The total deflection can be calculated as the superposition of deflections given by infinitesimal mass elements that compose the lens volume, which reduces the three-dimensional problem to a two dimensional one. It is thus useful to introduce the surface mass density $\Sigma(\vec{\xi})$, which is the mass density projected onto a plane perpendicular to the incoming light ray:

$$\Sigma(\vec{\xi}) = \int {\rm d}r_3 \rho(\xi_1(\lambda), \xi_2(\lambda), r_3(\lambda)), \tag{2.5}$$

where ρ is the density distribution of the lens, λ is an affine parameter and the light ray is propagating along r_3, $\xi_1(\lambda)$ and $\xi_2(\lambda)$.

The deflection angle produced by an arbitrary mass distribution can be expressed in terms of the surface mass density with:

$$\vec{\alpha}(\vec{\xi}) = \frac{4G}{c^2}\int {\rm d}^2\xi' \Sigma(\vec{\xi'})\frac{\vec{\xi} - \vec{\xi'}}{|\vec{\xi} - \vec{\xi'}|^2}, \tag{2.6}$$

given that the deflection from a straight line is small compared to the scale on which the mass distribution changes significantly.

We can express the reduced deflection angle in terms of the surface mass density as:

$$\vec{\alpha}(\vec{\theta}) = \frac{1}{\pi}\int_{\mathbb{R}^2} \mathrm{d}^2\theta' \kappa(\vec{\theta'})\frac{\vec{\theta}-\vec{\theta'}}{|\vec{\theta}-\vec{\theta'}|^2}, \tag{2.7}$$

where κ is the convergence (or the dimensionless surface mass density), which is given by:

$$\kappa(\vec{\theta}) = \frac{\Sigma(D_\mathrm{d}\vec{\theta})}{\Sigma_\mathrm{crit}}\,. \tag{2.8}$$

The critical surface mass density Σ_crit depends on the angular diameter distances between observer-lens D_d, observer-source D_s and between lens-source D_ds, the gravitational constant G and the speed of light c:

$$\Sigma_\mathrm{crit} = \frac{c^2}{4\pi G}\frac{D_\mathrm{s}}{D_\mathrm{d}D_\mathrm{ds}}\,. \tag{2.9}$$

We can also express the reduced deflection angle as the gradient of the deflection potential ψ:

$$\psi(\vec{\theta}) = \frac{1}{\pi}\int_{\mathbb{R}^2} \mathrm{d}^2\theta' \kappa(\vec{\theta'})\ln|\vec{\theta}-\vec{\theta'}| \tag{2.10}$$

as

$$\vec{\alpha} = \nabla\psi(\vec{\theta})\,, \tag{2.11}$$

where by making use of the identity:

$$\nabla^2\ln|\vec{\theta}| = 2\pi\delta_\mathrm{D}(\vec{\theta})\,, \tag{2.12}$$

we can also derive the Poisson equation in two dimension for convergence:

$$\nabla^2\psi = 2\kappa\,, \tag{2.13}$$

where δ_D is the two dimensional Dirac delta function.

2.2 Weak Gravitational Lensing

We have been concerned so far only with point sources or single light rays and we now discuss the case of extended objects. Besides being able to create multiple images of the same source, gravitational lensing also modifies the properties of a source from the point of view of the observer due to differential deflection across light bundles. Specifically, the shape of an object can be distorted (sheared) and the observed flux changed (magnified). The distortion of such an extended source can be described with a Jacobian matrix of the form:

$$\mathcal{A}(\vec{\theta}) = \frac{\partial\vec{\beta}}{\partial\vec{\theta}} = \delta_{ij} - \frac{\partial\partial\psi(\vec{\theta})}{\partial\theta_i\partial\theta_j} = \begin{pmatrix} 1-\kappa-\gamma_1 & -\gamma_2 \\ -\gamma_2 & 1-\kappa+\gamma_1 \end{pmatrix}, \tag{2.14}$$

where γ and κ are the shear and convergence. γ is a complex number and thus has two components:

$$\gamma \equiv \gamma_1 + \mathbf{i}\gamma_2 = |\gamma|e^{2\mathbf{i}\phi}, \tag{2.15}$$

and where κ is connected to the deflection potential ψ as seen in Equation 2.13.

The magnification factor μ is the inverse of the determinant:

$$\mu(\vec{\theta}) = \frac{1}{\det\mathcal{A}(\vec{\theta})} = \frac{1}{(1-\kappa)^2 - |\gamma|^2}. \tag{2.16}$$

The magnification factor can take both negative and positive values, with the corresponding images being said to have negative or positive parity. An infinitesimally small source is therefore dimmed or brightened by a factor of $|\mu(\vec{\theta})|$. The behaviour of magnification for certain values of $\vec{\theta}$ is highly non-linear or divergent, since the determinant of $\mathcal{A}$ can be very small or zero.

Although theoretically gravitational lensing is perfectly achromatic since photons of different wavelengths are deflected by the same amount, in practice magnification can exhibit a colour dependence due to the finite resolution of observations if the magnification varies on scales comparable to the source size.

Figure 2.2 shows the effect of different values of κ and γ when they are both much smaller than unity, within the so-called weak lensing regime. In other cases where the convergence and shear are very different from unity, gravitational lensing can lead to observable phenomena such as giant arcs, where background sources are severely distorted compared to their unlensed appearance.

In order to quantify the observed changes in the shape of the source, we start by defining the complex ellipticity:

$$\epsilon = |\epsilon|e^{2\mathbf{i}\phi}, \tag{2.17}$$

where ϕ is the position angle and:

$$|\epsilon| = \frac{1-r}{1+r}, \tag{2.18}$$

with r representing the axis ratio of the ellipse tracing the light distribution of the source. Re-writing the Jacobian in a different way:

$$\mathcal{A}(\vec{\theta}) = (1-\kappa)\begin{pmatrix} 1-g_1 & -g_2 \\ -g_2 & 1+g_1 \end{pmatrix}, \tag{2.19}$$

where we define the reduced shear g with:

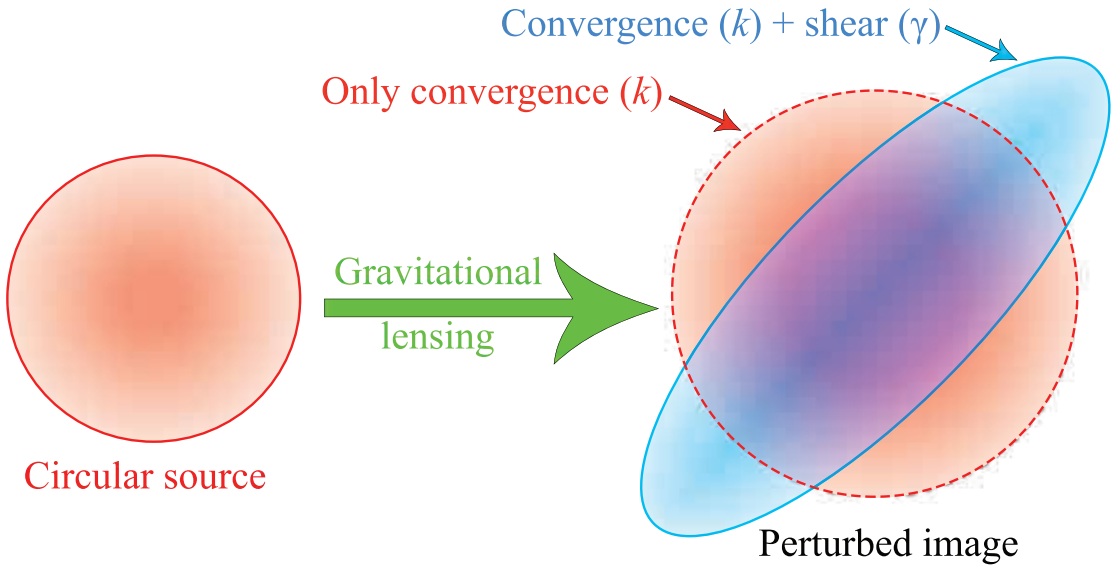

Figure 2.2: Illustration of the effects of convergence (κ) and shear (γ) on the shape and size of a hypothetical circular source. The convergence acting alone causes an isotropic magnification of the image (dashed red circle), while the shear deforms it to an ellipse (cyan).

$$g \equiv \frac{\gamma}{1-\kappa} = \frac{|\gamma|}{1-\kappa} e^{2i\phi} \,. \tag{2.20}$$

It is clear from Equation 2.19 that the $(1-\kappa)$ term is responsible for only an isotropic stretch of the image, unlike the other term that does affect the shape of the image. This implies that by measuring galaxy ellipticities one can only infer the reduced shear, not the convergence and shear separately.

It was shown by Schneider & Seitz (1995) that the ellipticity changes due to gravitational lensing as:

$$\epsilon_{\rm lensing} = \frac{\epsilon + g}{1 + g^* \epsilon} \text{ for } |g| \leq 1 \text{ and } \epsilon_{\rm lensing} = \frac{1 + g\epsilon^*}{g^* + \epsilon^*} \text{ for } |g| > 1 \,. \tag{2.21}$$

In general it is not known if a background galaxy is lensed or not. In order to overcome this problem a large number of galaxies are used, under the assumption that the average of the intrinsic ellipticities is zero, i.e. there is no preferred ellipticity orientation in the Universe. For an ensemble of galaxies that is of sufficient size it is possible to statistically determine values of weak lensing observables.

2.2.1 Magnification of Number Counts

If the luminosity function of a population of background source is sufficiently steep, this will lead to an enhancement of the number of observed sources in the vicinity of massive halos, an effect known as the magnification bias. There are two competing effects in a survey with a limit magnitude $mag_{\rm lim}$. First, there is a decrease in the ob-

served number of sources due to the solid angle enlargement effect of magnification, inversely proportional with the magnification factor μ. Second, the sources are being lensed (brightened) and therefore become detectable by the survey if they are brighter than $mag_{\rm lim} + 2.5 \log \mu$.

Reversing the idea above, the magnification produced by a gravitational lens can be detected through the change from inherent (N_0) to observed (N) differential number counts of background sources:

$$N(m)\,\mathrm{d}\,m = \mu^{\alpha-1} N_0(m)\,\mathrm{d}\,m\,, \tag{2.22}$$

(Narayan 1989), where m is the apparent magnitude of sources, and $\alpha \equiv \alpha(m)$ is proportional to the logarithmic slope of the source number counts as:

$$\alpha = \alpha(m) = 2.5 \frac{\mathrm{d}}{\mathrm{d}\,m} \log N_0(m)\,. \tag{2.23}$$

This means that the observed source spatial density of lensed galaxies can either increase or decrease, depending on the sign of $\alpha - 1$. Galaxies with number counts where $(\alpha - 1) > 0$ will appear to be spatially correlated with the position of lenses, while for $(\alpha - 1) < 0$ an anti-correlation will be observed. There is no effect in the case of $(\alpha - 1) \approx 0$, since the dilution and amplification effect will mutually cancel out and no correlation signal will be produced this way.

2.2.2 Galaxy Clusters and Gravitational Lensing

Clusters of galaxies are at the top of the mass scale of virialized objects in the Universe and contain tens to thousands of large galaxies, mostly early-type galaxies (ellipticals and S0 spirals). The gravitational potential of a galaxy cluster is then expected to be be strong enough to act as a gravitational lens. Some of the the most famous effects of strong lensing is the observation of luminous arcs and multiple images of background objects around the inner regions of galaxy clusters. These effects can be used for reconstructing the mass distribution of the inner part of the lens. The weak lensing effects of galaxy clusters are more subtle, with the average shapes and sizes of galaxies suffering systematic changes tangentially around galaxy clusters.

CHAPTER 3

Data

Sections of this chapter have already been published in Tudorica et al. (2017).

3.1 SWIRE - Infrared Data

The Spitzer Wide-area InfraRed Extragalactic Legacy Survey[1] (SWIRE) (Lonsdale et al. 2003) is one of the six large legacy surveys observed during the first year in space of the Spitzer Space Telescope. It covers approximately 50 deg^2 in all 7 infrared wavelength bands available on Spitzer: four with the Infrared Array Camera (IRAC, see Fazio et al. 2004) at 3.6, 4.5, 5.8, 8 μm, and three more with the Multiband Imaging Photometer for Spitzer (MIPS, see Rieke et al. 2004), at 24, 70 and 160 μm. The survey is divided in six separate patches on the sky, carefully chosen to be the best infrared fields for detecting faint infrared galaxies and quasars, away from the direction of our Milky Way's disk of stars and as free as possible from interplanetary or interstellar gas and dust. Three of the fields are located in the northern hemisphere (European Large Area ISO Survey - ELAIS - N1, N2 and the Lockman Hole), two of the fields in the southern hemisphere (ELAIS S1 and Chandra Deep Field South) and one equatorial field, XMM-Newton Large Scale Structure Survey (XMM LSS). We used only the XMM LSS, ELAIS N1&N2 and the Lockman hole fields for this research. Figure 3.1 shows the outline of the four SWIRE fields that overlap with the CFHT data and the individual CFHT pointings used in this work.

3.2 SpARCS - Optical Follow-up of SWIRE

The Spitzer Adaptation of the Red-Sequence Cluster Survey (SPARCS Wilson et al. 2009; Muzzin et al. 2009) is a follow-up survey of the SWIRE fields in the z' band down

[1] http://swire.ipac.caltech.edu/swire/public/survey.html

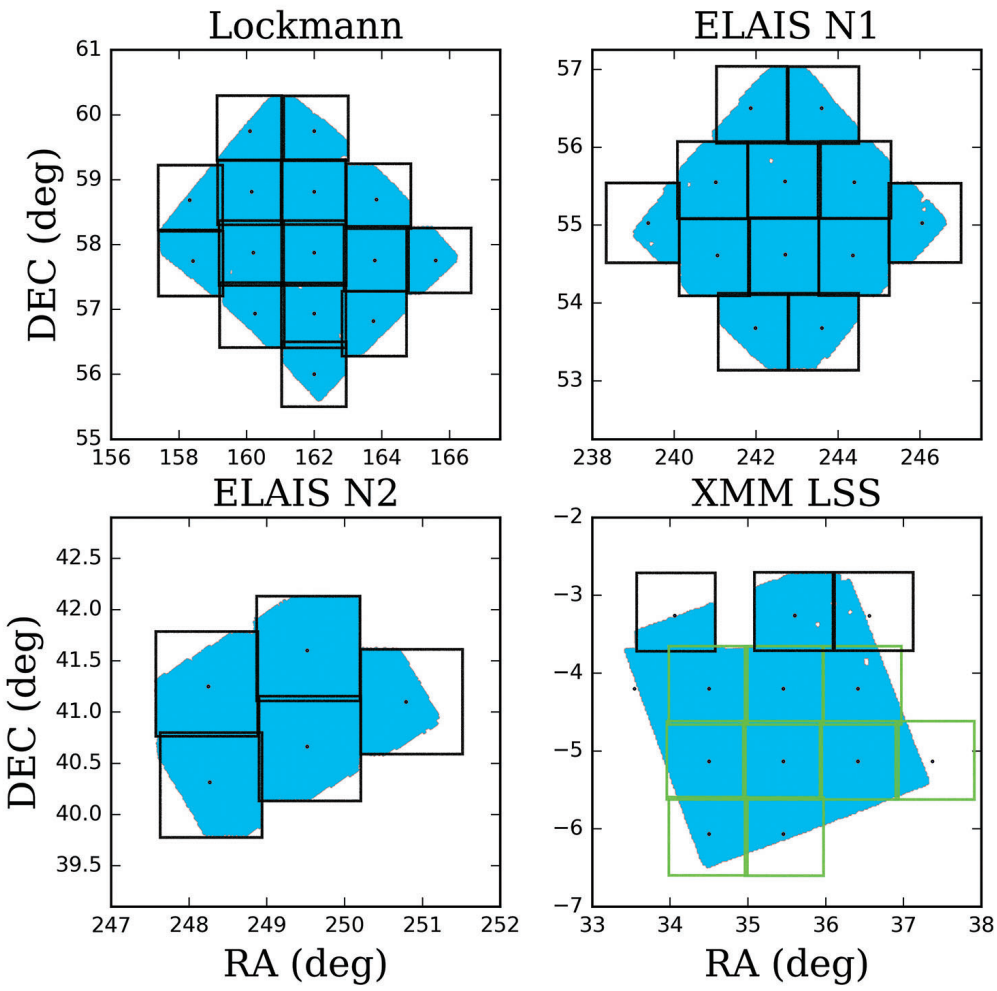

Figure 3.1: Outline of the SpARCS fields observable from the northern hemisphere. The blue area traces the distribution of sources detected in SWIRE (with the original data masking applied), while the black squares show the locations of the CFHT individual pointings, each covering approximately 1 $\deg^2$. The bottom green squares in the XMM LSS field outline the CFHTLS pointings we use. Pointing centres are marked with black dots.

Table 3.1: Properties of the six SpARCS fields. ELAIS S1 and Chandra Deep Field South (DFS) are not used in our study and do not have corresponding optical (*ugriz*) data. All areas are in deg^2.

Field Name	RA (centre) (HH:MM:SS)	Dec (centre) (DD:MM:SS)	SWIRE Area	SpARCS Area	Usable Area	Filters
ELAIS S1	00:38:30	-44:00:00	7.1	8.3	6.5	...
XMM LSS	02:21:20	-04:30:00	9.4	11.7	7.3	*ugriz*
Chandra DFS	03:32:00	-28:16:00	8.1	7.9	7.1	...
Lockman Hole	10:45:00	+58:00:00	11.6	12.9	9.7	*ugrz*
ELAIS N1	16:11:00	+55:00:00	9.8	10.3	4.3	*ugrz*
ELAIS N2	16:36:48	+41:01:45	4.4	4.3	3.4	*ugrz*
Total			50.4	55.4	41.9	

to a mean depth of $z'_{AB} = 24.0$ at 5σ (for extended sources), using MegaCam on the 3.6 m CFHT for the three Northern fields and XMM LSS, while MOSAIC II was used on the 4 m Blanco telescope at the Cerro Tololo Inter-American Observatory (CTIO) for the Southern Fields. It is one of the largest high-z cluster surveys with a total area of 41.9 deg^2, with hundreds of $z > 1$ cluster candidates based on the $z' - 3.6\,\mu$m colour. It was designed to assemble a large homogeneously-selected sample of massive clusters up to $z \sim 2$ (Muzzin et al. 2009; Wilson et al. 2009; Demarco et al. 2010; Muzzin et al. 2012) by using a version of the cluster red-sequence method adapted to the infrared. The 4000Å-break at $z > 1$ traverses the $z' - 3.6\mu$m color, making possible the detection of red-sequence galaxies over-densities that trace massive galaxy clusters, while simultaneously providing a reliable redshift estimate for the clusters through the colour fit to the red-sequence.

3.2.1 Cluster Catalogue

The SpARCS cluster catalogue is created by using a modified version of the Gladders & Yee (2000) algorithm, as described in detail by Muzzin et al. (2008). The Cluster Red-Sequence (CRS) method employed requires the use of only two imaging passbands that span the rest-frame of the 4000 Å break feature in early type galaxies. Elliptical galaxies constitute the dominant population in galaxy clusters, lying along a linear relation in colour-magnitude space. In the colour-magnitude diagram constructed with such a combination of filters, elliptical galaxies in clusters appear always as the reddest and brightest at any specific redshift, strongly contrasting with the field population.

Muzzin et al. (2009) and Wilson et al. (2009) construct the cluster candidates catalogue by finding peaks in the smoothed spatial galaxy density maps of individual colour slices representing different redshifts. Galaxies are given weights based on several criteria. In addition to weights based on their colours, galaxies are also weighted based on their apparent magnitude, relative to a fiducial M* value, since early type

cluster galaxies are usually the reddest and brightest galaxies within a colour slice. The probability of belonging to a colour sequence model line for a particular galaxy is also taken into account by weighting. A probability map is constructed for each colour slice by considering the aforementioned weights, representing the spatial galaxy density map of the survey within each redshift slice. The pixel size for each map is 125kpc at all redshifts. The galaxies within each pixel are added, weighted by the product of the corresponding colour and magnitude weights. Each map has the noise properties homogenised by smoothing with an exponential kernel and by adding redshift dependent noise maps. We refer the reader to Section 3.1-3.6 of Muzzin et al. (2008) for a detailed description of the cluster detection algorithm and to Muzzin et al. (2009) and Wilson et al. (2009) for more details on its application to the SpARCS dataset.

The richness parameter associated with these detections is quantified by $N_{\rm red}$, a slightly altered version of the cluster-centre galaxy correlation amplitude ($B_{\rm gc}$) estimator described in detail by Yee & López-Cruz (1999). $N_{\rm red}$ represents the number of background-subtracted, red-sequence galaxies brighter than M^* + 1 within a 500 kpc circular aperture. M^* is determined from the survey data (see Section 5.1 and Figure 14 in Muzzin et al. 2008), while the width of the red-sequence is chosen to be ±0.15 mag at all redshifts. The scaled version of $N_{\rm red}$, $B_{\rm gc}$ has been shown to correlate well with various cluster properties (e.g. R_{200}, X-ray temperature, velocity dispersion, virial radius, see Yee & López-Cruz 1999; Yee & Ellingson 2003; Gilbank et al. 2004; Muzzin et al. 2007).

The exact position of the cluster centre is a critical piece of information as many important properties are estimated using measurements that depend significantly on the approximated centre position (e.g. richness, mass, luminosity function etc.). Muzzin et al. (2008) estimate two centroids, one based on the location of the peak of the red sequence probability flux in the probability maps, and the other defined as the position where the $N_{\rm red}$ is maximised. We correct for cluster miscentering statistically in the model by shifting the cluster centres with a radial offset following a 2-D Gaussian probability distribution (see Figure 1 in Ford et al. 2014). Since the difference between these two centroid estimates is small and it does not make a significant difference in the final results, we chose to use only the former cluster centre estimates from Muzzin et al. (2008), i.e. the position where the $N_{\rm red}$ is maximised.

The CRS technique is well tested and is an observationally efficient method for selecting galaxy clusters in high-redshift surveys (Gladders & Yee 2005; Wilson et al. 2005), providing photometric redshifts accurate to 5 percent (Gilbank et al. 2007; Blindert et al. 2004) as well as low false-positive rates (smaller than 5%, see e.g., Gilbank et al. (2007); Blindert et al. (2004); Gladders & Yee (2005)). As part of the Gemini CLuster Astrophysics Spectroscopic Survey (GCLASS), 10 of the richest cluster candidates in SpARCS with a photometric redshift range $0.86 \leq z \leq 1.34$ were observed spectroscopically over 25 nights with the Gemini North and South telescopes, confirming their cluster nature and their distance estimated with the CRS algorithm (Muzzin et al. 2012; van der Burg et al. 2014).

We select 287 candidate clusters from the SpARCS catalogue compiled by Muzzin et al. (2009) and Wilson et al. (2009), with a cut-off in richness $N_{\rm red} \geq 10$, which ensures

that the detection significance is high and the candidate has a high likelihood of being a real galaxy cluster. The distribution of redshifts and of the $N_{\rm red}$ richness for the sample, along with 6 individual clusters from GCLASS can be seen in Figure 3.2, while Figure 3.3 shows the optical appearance of one very high redshift cluster ($z = 0.871 \pm 0.002$).

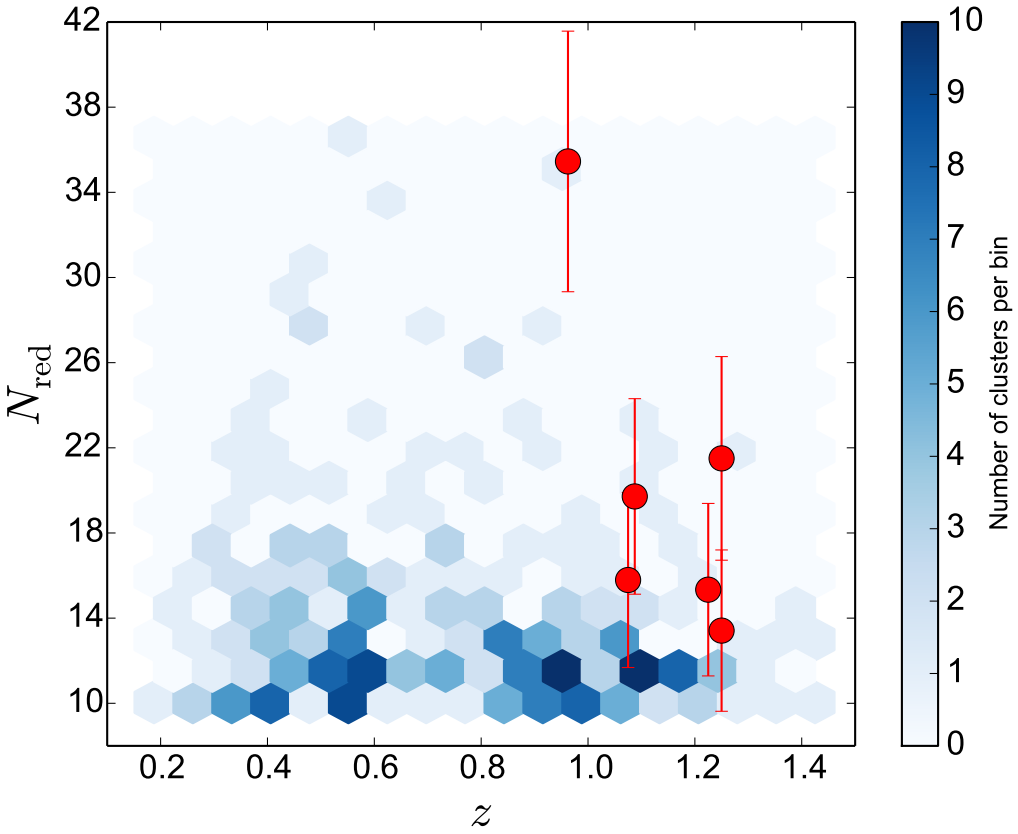

Figure 3.2: Number density as a function of redshift and richness for the sample of galaxy clusters used in this study. The six GCLASS clusters falling within the area covered by the CFHT data are shown individually with the red points, with the errorbars representing the uncertainty in their $N_{\rm red}$ values.

3.3 CFHT *ugriz* Optical Data

We add *ugri* coverage to the Northern SpARCS fields from available CFHT archival and proprietary data, with the total area and available filters for each patch described in Table 3.1. The MegaCam instrument is mounted in the CFHT prime focus and consists of 36 charge-coupled devices (2048 × 4612 pixels each, totalling 340 megapixels) with a pixel scale of 0.187″ and covering a total field of view of about 1 deg^2.

We obtained 35 individual CFHT MegaCam pointings designed to maximise the total overlap with the SWIRE fields. Coverage in the *i*-band is available only for the

Figure 3.3: SpARCS-J161315+564930, a galaxy cluster situated at a redshift of $z = 0.871 \pm 0.002$, having 14 high-confidence cluster members, a rest-frame velocity dispersion $\sigma_v = 1230 \pm 320 km\, s^{-1}$ and a corresponding mass $M = 16.9^{+4.0}_{-3.5} \times 10^{14} M_\odot$.

pointings overlapping the XMM LSS area[2]. We aimed to have a uniform depth for the fields in all bands, complementing existing data with our observations. The *r*-band average depth goal was $r \lesssim 24.5$, since the brightest LBGs ($\lesssim 24.5$) carry the largest signal. Table 3.2 contains the average seeing, limit magnitude and exposure time of each band. The limit magnitude is based on the values given per pixel by `SExtractor` and are calculated for a 2″ (diameter) circular aperture at 5σ. The minimum number of images stacked for each filter per pointing is 4.

For approximately 7 deg^2 of the XMM LSS area we make use of existing data reduced by the CFHTLenS collaboration (Heymans et al. 2012) using similar tools and methods to our approach, which ensure uniformity in the final data products (Hildebrandt et al. 2012; Erben et al. 2013).

[2] The corresponding CFHT proposal identification codes (PIDs) for the SpARCS optical data are: 12AC02, 12AC99, 12BC05, 11BC97 and 11BC23.

Table 3.2: The average seeing (before PSF homogenization), limit magnitude and exposure times for each filter of the CFHT individual pointings.

Filter	Seeing ($''$)	Limit magnitude (mag)	Exposure time (hours)
u	0.96	24.28	1.17
g	0.95	24.61	0.91
r	0.81	24.20	0.87
i	0.80	23.50	0.59
z	0.68	23.15	1.76

3.4 Data Reduction & Source Selection

3.4.1 Basic Data Reduction

The CFHT data retrieved from the archive are already pre-processed with `ELIXIR`[3] (Magnier & Cuillandre 2004). `ELIXIR` consists of a collection of programs, databases and other tools related to the processing and evaluation of the data acquired with the telescope. This pre-processing includes the masking of dead or hot pixels, bias and overscan correction, flat-fielding, photometric superflat, fringe correction for the i and z data, as well as a rough astrometric and photometric solution for each field. An example of a frame after such basic preprocessing can be seen in Figure 3.4.

We detail below the main steps of the subsequent data reduction process, which are based on the work-flow used by the CFHTLenS collaboration (Heymans et al. 2012; Erben et al. 2013). Additionally, we convolve the different bands to the same (worst) seeing (PSF homogenization) (Hildebrandt et al. 2013). The data for each observation run are treated as a group, only separated by filter.

Basic quality control

A basic quality control is carried out for each of the images, identifying chips with a large number of saturated pixels, severe tracking errors, misidentified image type, incorrect exposure time etc. These data is excluded from further processing in order to keep the raw input data as clean as possible.

[3] CFHT data reduction pipeline

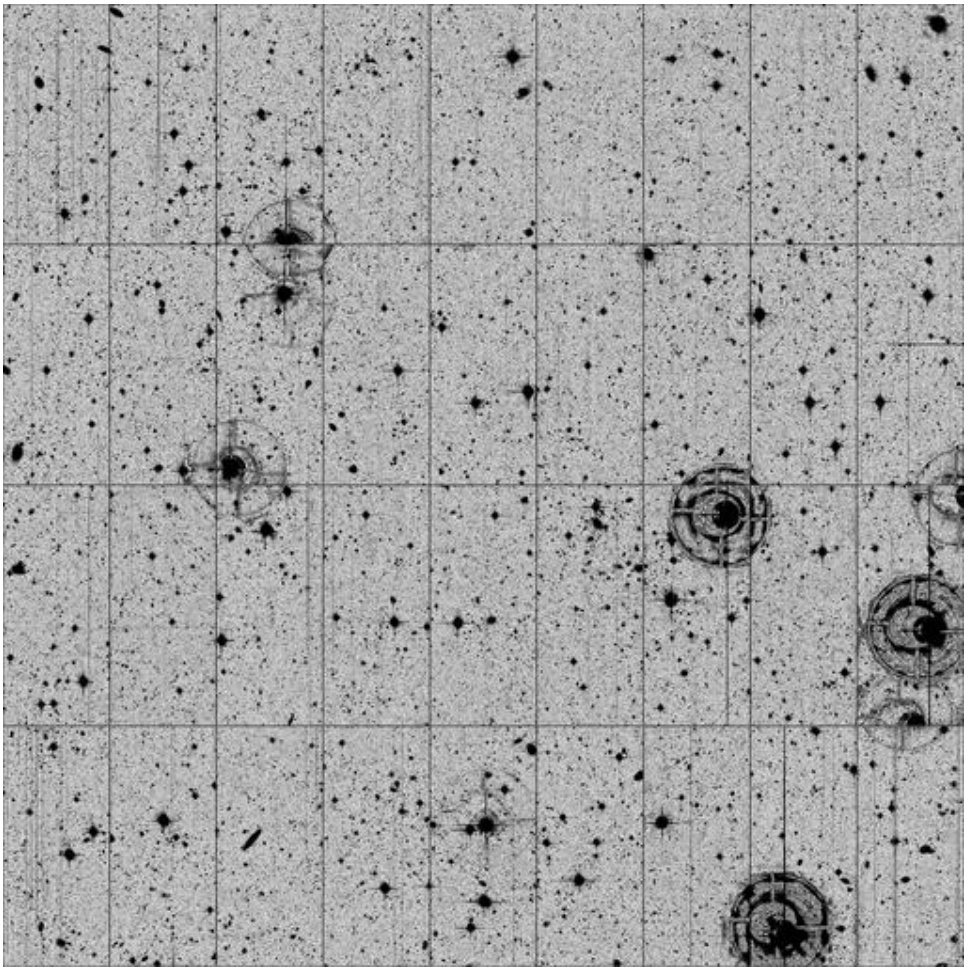

Figure 3.4: One observed field *r*-band after the basic data reduction step (CCD gaps excluded).

Satellite tracks

Satellite tracks are identified using a method based on a feature extraction technique (Hough transform, see Vandame 2001). This method was initially devised for finding imperfect instances of objects that belong to a certain class of shapes, by using a voting procedure carried out in the parameter space constructed by applying the Hough transform.

Flag and weight images

Weight maps characterize the sky-noise properties by assigning relative weights for each pixel in the science data. Flag images mark the pixels that contribute to the final co-added science image (a value of 1 in the co-added image indicates a pixel that does not have information from any of the input single frames). Flag and weight images are created for each chip, including dead or hot pixels or columns, saturated areas of the chips (e.g. the centres of very bright stars) and the satellite track masks from the

previous step.

Basic source catalogues

The source catalogues necessary for astrometric calibration are created using `Source Extractor` (`SExtractor`, Bertin & Arnouts 1996). Only sources that pass a signal-to-noise threshold of 5 σ are selected in order to ensure the accuracy of determining their positions.

Astrometric calibration

Absolute, internal astrometric calibration, and the relative photometric calibration of the *ugriz*-band images is accomplished for each field using `Software for Calibrating AstroMetry and Photometry (SCAMP)` (Bertin 2006) and the 2MASS astrometric catalogue (Skrutskie et al. 2006) as a reference. A visualisation of the 2-dimensional scatter of internal (for the same stars in each frame) and external astrometric residuals (compared to the external catalogue) can be seen in Figure 3.5 and Figure 3.6. For one pointing and filter, Figure 3.7 shows the external astrometric catalogue objects and the matches with each image, as well as an overlay of the distribution of the individual CCDs.

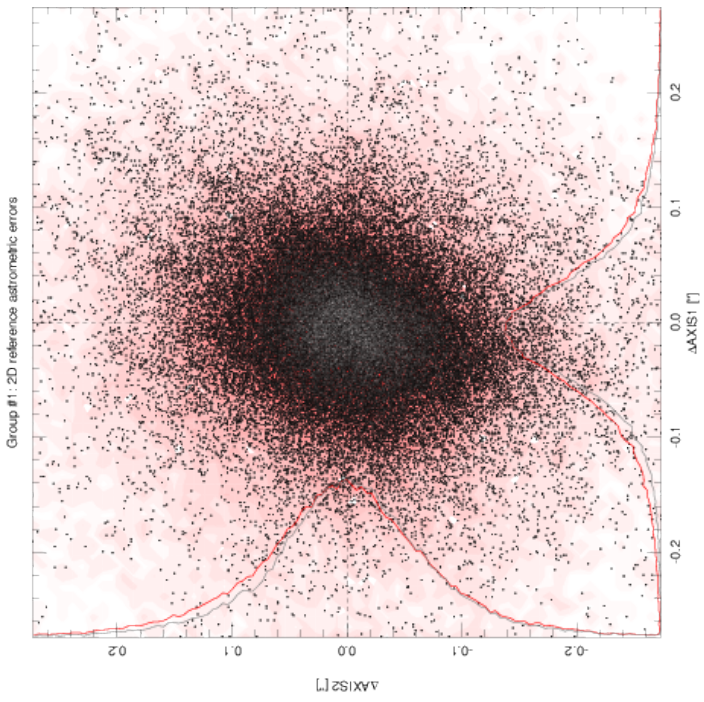

Figure 3.5: 2-dimensional scatter plot showing the residuals between the coordinates of detected sources and the coordinates of the associated astrometric reference object. The width of this distribution is expected to be determined in the case of a correct astrometric match by the precision in the position of the reference catalogue sources.

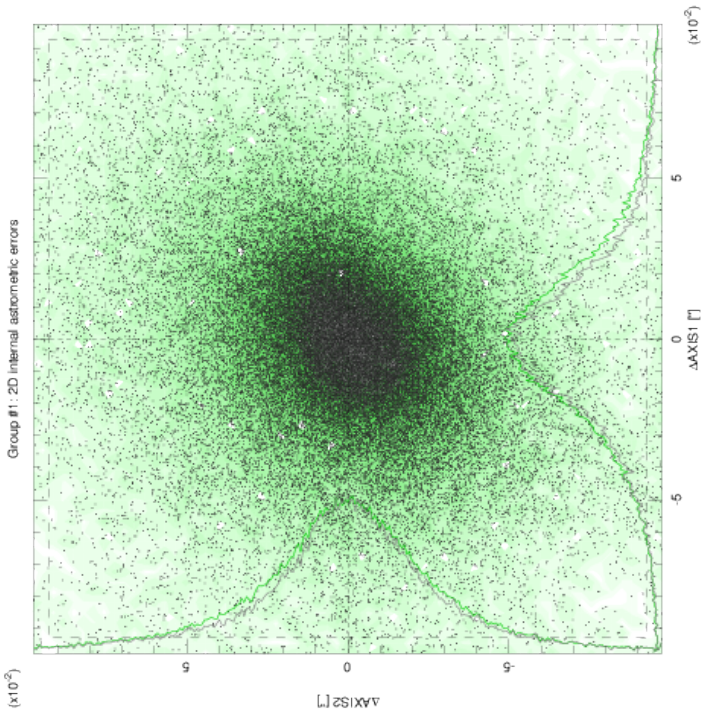

Figure 3.6: 2-dimensional scatter plot showing the internal astrometric residuals between coordinates of overlapping detections for the individual exposures of a field, after convergence to a matching solution. Typically, for a good astrometric solution we expect a featureless 2-dimensional normal distribution, whose width is of the order of 1/10th-1/20th of a pixel.

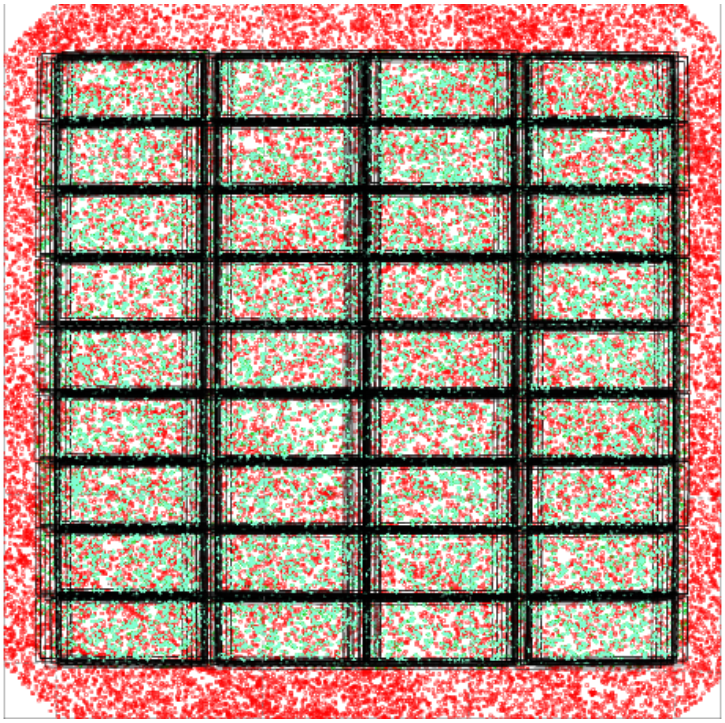

Figure 3.7: For each group of images, the field limits, source detections, astrometric sources after astrometric calibration (red circles) are shown in a similar figure to the one displayed above. The dither pattern employed for the observation of this particular field is mirrored by the positional changes of the black rectangles (denoting individual CCDs). A match for all input frames between the astrometric reference stars and the sample of high signal-to-noise source detections in the images is shown by a green circle.

Distortion correction

Image distortion is being modelled from the astrometric residuals determined in the previous step, shown in Figure 3.8 as a variation of pixel scale with pixel position.

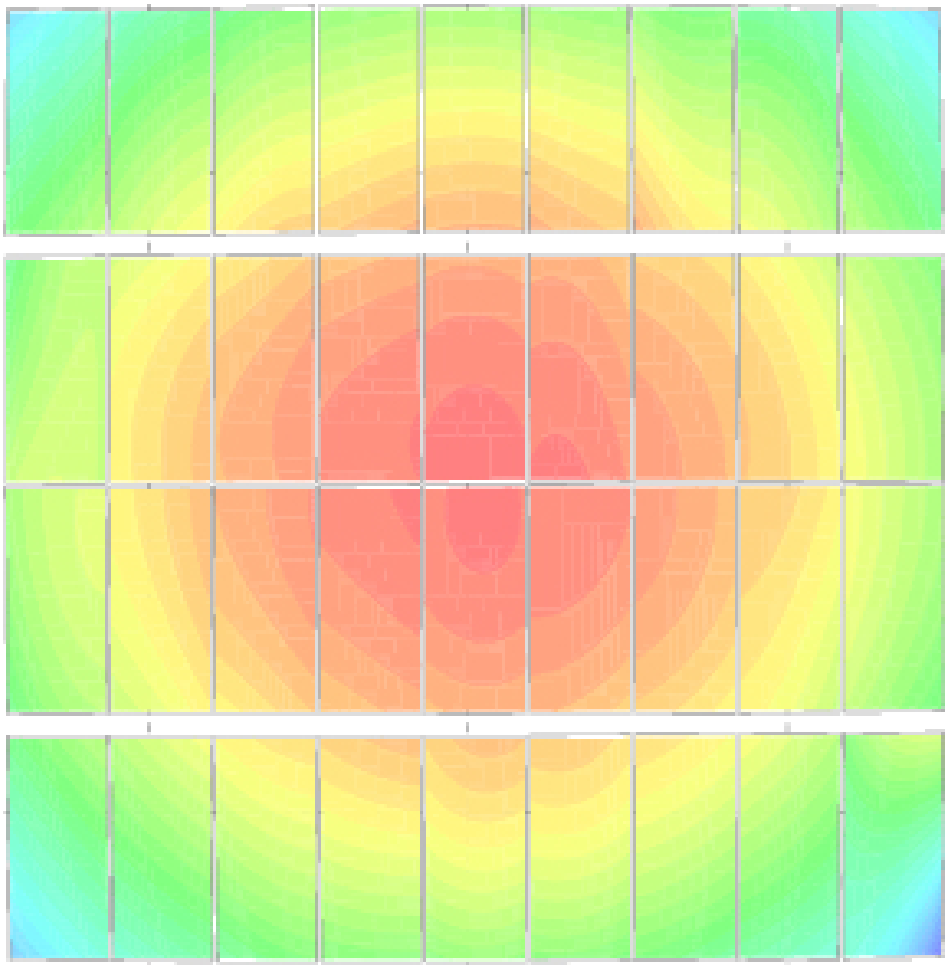

Figure 3.8: A map of the image distortion for one observed field, with the individual CCDs composing the detector being individually displayed. The distortion is represented here as a variation of the pixel scale across the detector area, using a colour scale ranging from blue (decrease of the pixel scale) to red (increase of the pixel scale), while green depicting areas with no change.

Background subtraction

Before co-adding the science images, the background level of the sky is modelled and subtracted in order to obtain a flat (on large scales) background sky level. A sufficiently large kernel was used in order to ensure that only the large scale fluctuations in the sky background were subtracted, in order to avoid biasing measurements (on small angular scales) for the sources of interest.

Co-addition

The coaddition of images is accomplished using a statistically optimal weighted average method with the `SWarp` software (Bertin et al. 2002), which accounts for the sky-background noise, the relative photometric zeropoints and the weight maps.

Image convolution and PSF correction

To account for the photometric issues created by PSF heterogeneity between different bands, we convolve the images to the same PSF using methods developed by Kuijken (2008). We always degrade the image to the image passband that has the worst seeing in order to optimize the extraction of magnitude differences between the filters for all sources. The PSF anisotropy is also minimized, with an example of before and after correction being shown in Figure 3.9.

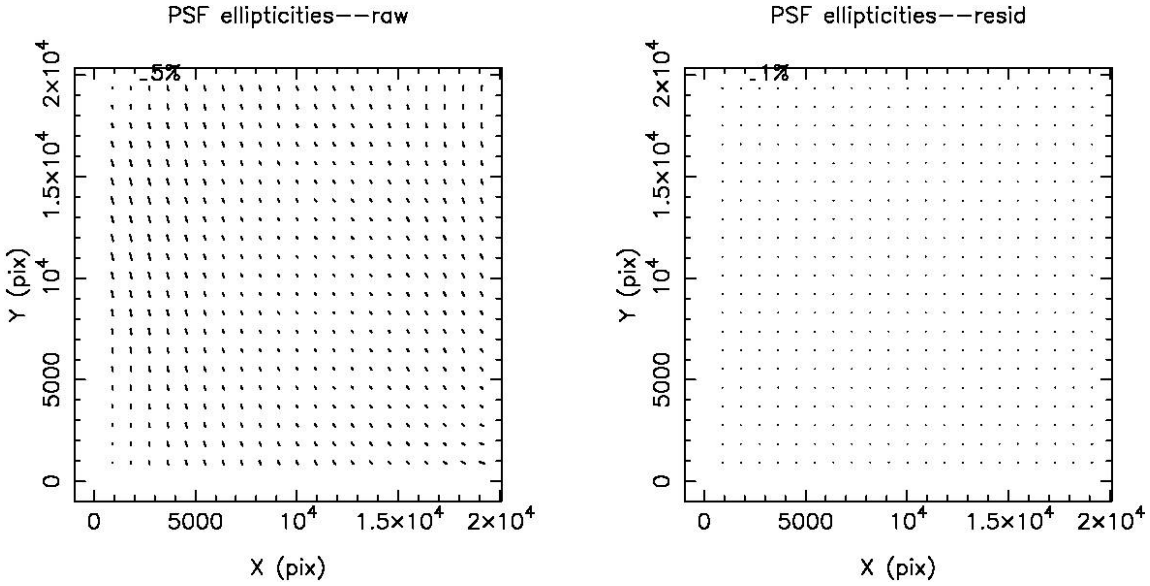

Figure 3.9: Left: PSF anisotropy of an *r*-band field determined by measuring stellar shape distortions. Right: Residual PSF anisotropy after correction. Note the different scales for the distortions in the two images, as noted in their upper-left corner.

Source extraction

With `SExtractor` it is possible to detect sources in one band and measure photometric quantities on another (dual image mode). We detect sources on the *r*-band, which is on average the deepest. This has the advantage that photometry can be forced in another band at a location where a source is known to exist and that colours are very accurately estimated if the PSF is uniform between different bands. The multicolour catalogue contains measurements in all bands for all of the *r*-band detected sources, in isophotal apertures defined by the *r*-band measurement. Five contiguous pixels with a detection threshold of $1.5\,\sigma$ above the background are the minimum criteria

required to have a detection by SExtractor. Figure 3.10 shows the distribution of the magnitude limit for one co-added image as a function of position within the field, with features such as the chip gaps, large stellar haloes and satellite tracks being easily observed through a decrease in the magnitude limit in their vicinity.

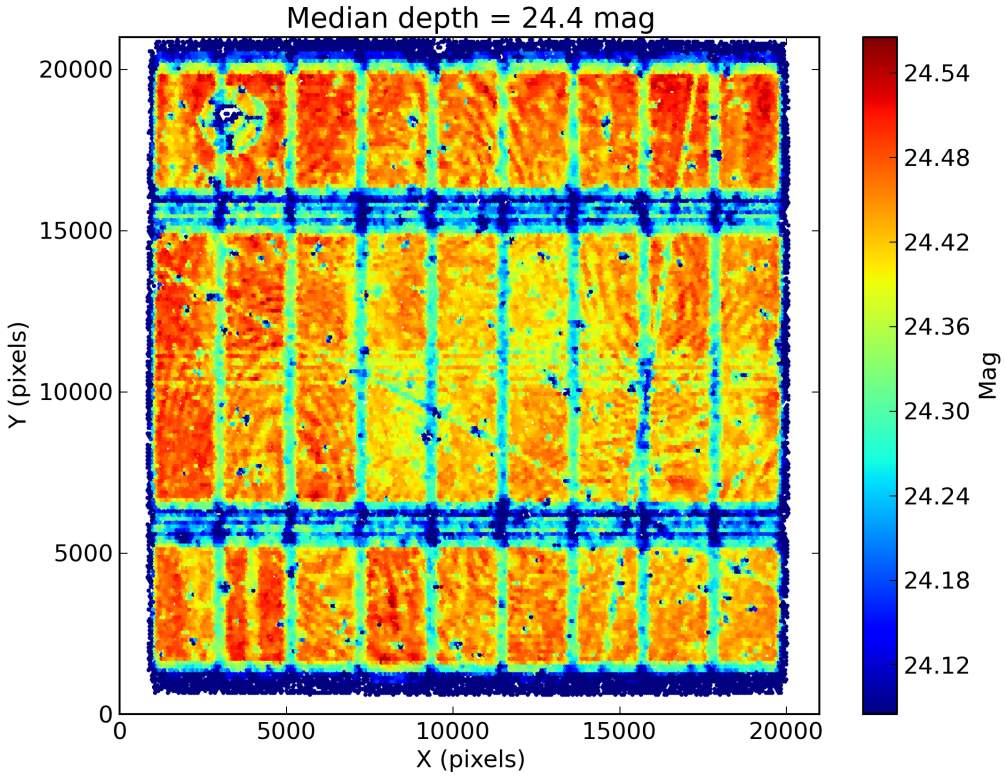

Figure 3.10: The median magnitude limit for the sources detected in the *r*-band of the ELAIS N1 P1 field as a function of position on the detector.

Masking

To mask image defects and regions where photometry is unreliable (around bright stars because of halos and diffraction spikes, in areas with a low signal-to-noise ratio, around reflections producing ghost images of bright objects, on top of asteroid tracks etc.), we use the AUTOMASK software (see Erben et al. 2009; Dietrich et al. 2007) and information from the image weights for all bands used in selecting the *u*-dropouts. The end result of the automatic masking process can be seen in Figure 3.11 for one full image, while Figure 3.12 shows in more detail the masking for the centre-left of the same image. Furthermore, each image is individually inspected visually and other problematic regions are manually excluded from the analysis using customized DS9 polygon regions. The masked objects are flagged in the multi-colour catalogue.

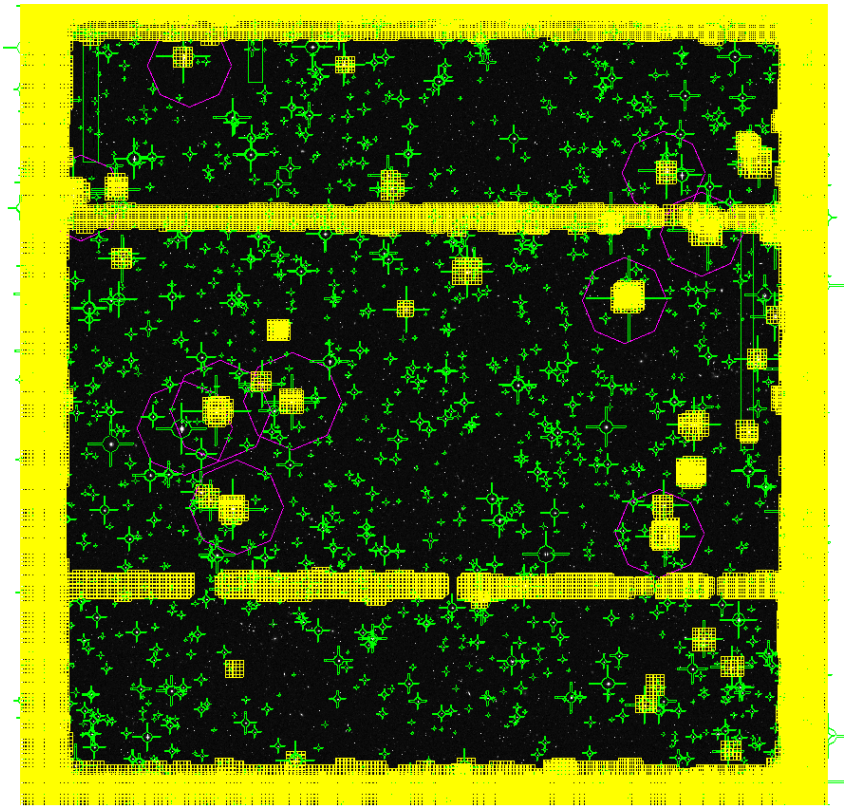

Figure 3.11: A typical field and its corresponding mask. Low object density areas, diffraction spikes, stellar reflections and halos, asteroids and CCD defects are automatically masked.

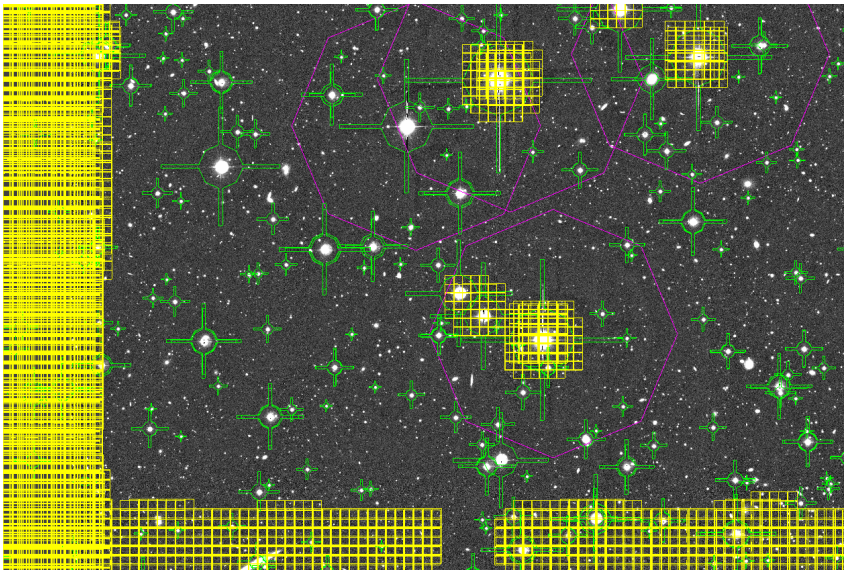

Figure 3.12: Part of field mask, with the star halo and spikes being masked automatically (with green and respectively magenta), while a detection of low source density is masked out by the yellow squares.

Final absolute photometric calibration

The final absolute photometric calibration is based on SDSS DR10 (Ahn et al. 2014). We compare the median magnitude of stellar objects in our multicolour catalogue and shift each band to match with the median magnitude of the same objects in SDSS DR10.

Photometric redshifts

Photometric redshifts are estimated using the `BPZ`[4] code (Benítez 2000), based on priors from the VIMOS VLT Deep Survey (VVDS, see Le Fèvre et al. 2013; Raichoor et al. 2014). We also provide photo-z estimates for objects that are not detected in one or more of the *ugiz*-bands (objects that have magnitudes fainter than the limit magnitudes in each field, which can occur with the dual-image mode of `SExtractor`). Note though that photometric redshifts were not used in this study but are available within the data products.

Website description

The co-added images, weights, masks, associated source catalogues and systematic effects check-plots have been prepared for and released to the public through a dedicated website. Appendix B contains a detailed description of the available image and catalogue data.

3.4.2 LBG Candidates

Lyman Break Galaxies

LBGs are high-redshift galaxies that undergo star formation at a high rate (Steidel et al. 1998). The upper energy limit of the Lyman series represents the highest energy photon that can be emitted by the hydrogen atom during recombination processes or alternatively, the minimum energy required for ionizing a hydrogen atom in the ground state. For this reason, neutral hydrogen tends to heavily absorb photons with wavelengths shorter than the Lyman-limit at 911.8 *nm*, thus severely depressing the observed emission spectra above this energy limit. Star-forming regions in galaxies are usually surrounded by clouds of neutral hydrogen and in combination with dust absorption within galaxies produce a first-order Lyman-break. This is however sensitive to the galaxy properties and its intensity varies, with the end result being a dispersion of galaxies in the color-color plane, with redshift and colour being strongly degenerate.

The inter-galactic medium (hereafter IGM) also contains vast quantities of neutral hydrogen and not only it does yield a higher amplitude effect, but one that is also independent from intrinsic characteristics of the observed objects, thus enabling the

[4] `http://acs.pha.jhu.edu/~txitxo/bpzdoc.html`

observer to select an unbiased population of galaxies. (Blaizot et al. 2004). In addition, very few stars are hot enough to produce many photons with energies above the Lyman limit, which decreases even further the total flux at wavelengths smaller than 911.8 *nm*.

The combined effect of these high-energy photons absorption results in an apparent and abrupt change in the observed magnitudes. By judiciously choosing the filters to span the Lyman limit in the observer reference frame, the magnitude drop is often of sufficient amplitude that the object can no longer be detected in one of the filters used - hence the name "dropout technique". Figure 3.13 illustrates the technique by showing an example of an u-dropout LBG candidate, with the generic LBG spectrum plotted over the transmission curves of the filters used.

Employing a combination of filters in the optical domain, generally one can select LBGs at a redshift $z > 2.5$. For a galaxy at this redshift, the Lyman-break is located between the g and u filters (Steidel & Hamilton 1993). The $u - g$ color is very sensitive to the redshift of the object observed due to the very steep slope in the color-color space and by adopting the color criteria mentioned in Eq. 3.4.2 we obtain a precise selection of galaxies in redshift space with only a small percentage of misidentified objects.

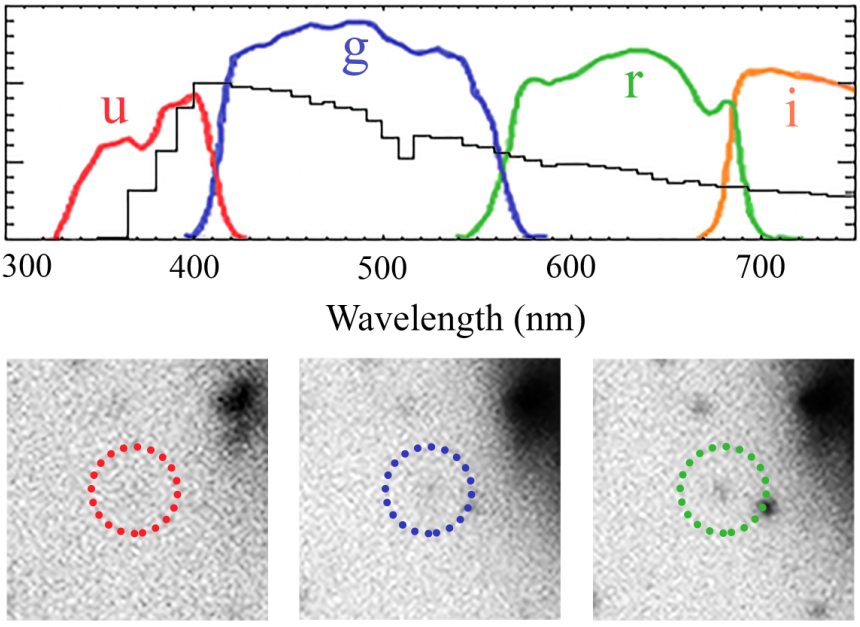

Figure 3.13: The upper panel shows an example of a typical observation of a Lyman Break galaxy spectrum (black line) with the CFHT filter transmission curves superimposed (the y-axis scale is arbitrarily scaled). The lower panel shows three images of one LBG detected using the dropout technique described in Section 3.4.2. While the galaxy is detected in the g and r-bands, it is not visible in the u-band (inside the dashed circles).

LBGs and magnification

The background population of sources used to probe the magnification signal consists of u-dropouts which are LBG candidates. LBGs have been used successfully in the past for magnification studies (see Hildebrandt et al. 2009; 2013; Morrison et al. 2012; Ford et al. 2012; 2014) since their luminosity function and redshift distribution are relatively well understood. Because the magnification signal is sensitive to the slope of the number counts of the sources used, knowledge of the luminosity function is essential for such measurements. Another advantage of using LBG as background sources is that they are situated at much higher redshifts than the galaxy clusters studied here, therefore reducing the probability of having a magnification-like signal induced by physical correlations between sources and clusters.

For the u-dropouts, we adopt the colour selection criteria previously used in Hildebrandt et al. (2009):

$$\begin{cases} 1.5 < (u-g) \\ -1.0 < (g-r) < 1.2 \\ 1.5\,(g-r) < (u-g) - 0.75 \end{cases}$$

Figure 3.14 shows the distribution of the number density of galaxies in the $u-g$ vs $g-r$ colour space, with contours logarithmically spaced. The selected u-dropouts are located in the shaded area. The selection of dropouts using these cuts in the $g-r$, $u-g$ colour space has been shown with simulated data (for a similar, but deeper data set) to produce a contamination level from stars and low-z interlopers below 10% for each magnitude bin (Hildebrandt et al. 2009). We also require the candidates to have a `SExtractor` CLASS_STAR parameter smaller than 0.9, which facilitates the rejection of most stars in the sample. Since our median FWHM is 0.8″ in the detection band, we can still reliably separate stars from high-redshift galaxies at bright magnitudes. An additional size constrains is added, requiring the object to be smaller than 5″, since LBGs at $z = 3.1$ have a maximum size of about 2″ − 3″ (Giavalisco et al. 1996). Furthermore, after applying the image masks to the data, each object in the resulting sample of LBG candidates is visually inspected, rejecting obvious false detections such as:

- very extended objects
- bright knots in spiral galaxies
- densely populated fields (numerous objects, partially or completely overlapping)
- other image defects not being masked automatically

A few examples of rejected u-dropout candidates can be seen in Figure 3.15.

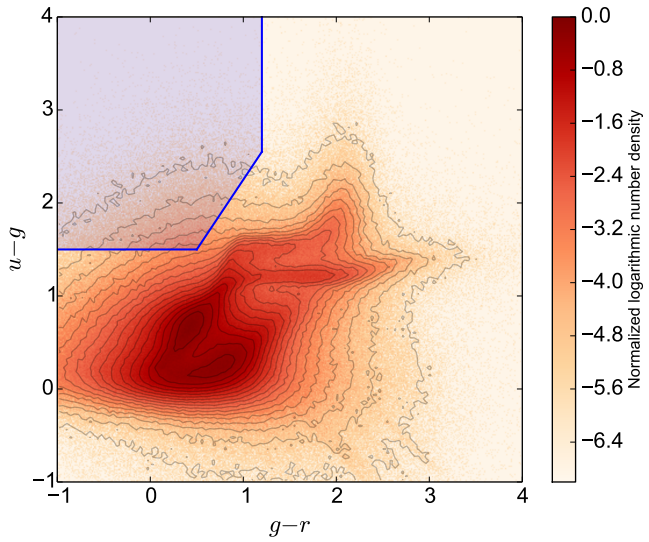

Figure 3.14: $u-g$ vs $g-r$ colour-colour number density plot of the galaxies in the SpARCS fields, selected with the `SExtractor` parameter CLASS_STAR < 0.9. The colour selection criteria described in Sect. 3.4.2 are delineated on the upper left of the image with the shaded area and the blue lines.

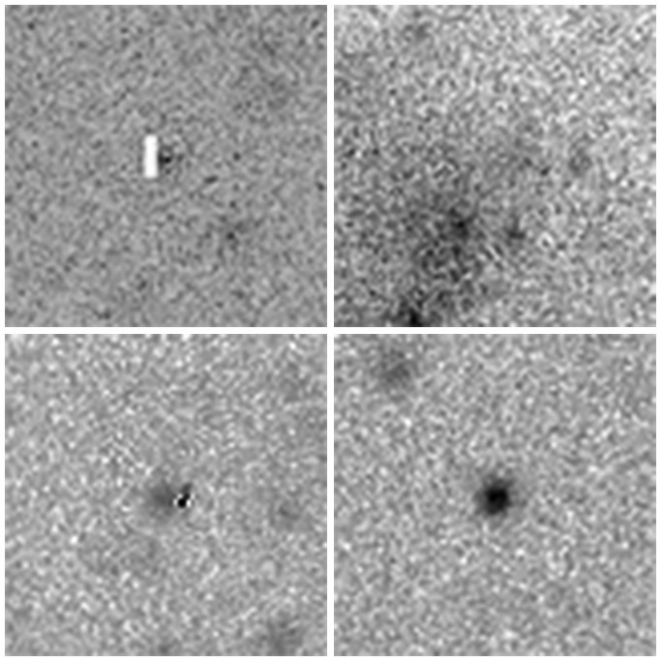

Figure 3.15: Examples of LBG candidates rejected after the visual inspection of the entire sample (top row and bottom left) and one example of an accepted u-dropout (bottom right). Top left and bottom left candidates were rejected due to hot and cold pixels respectively, while the top-right candidate was rejected because of the diffuse light contaminating the photometry.

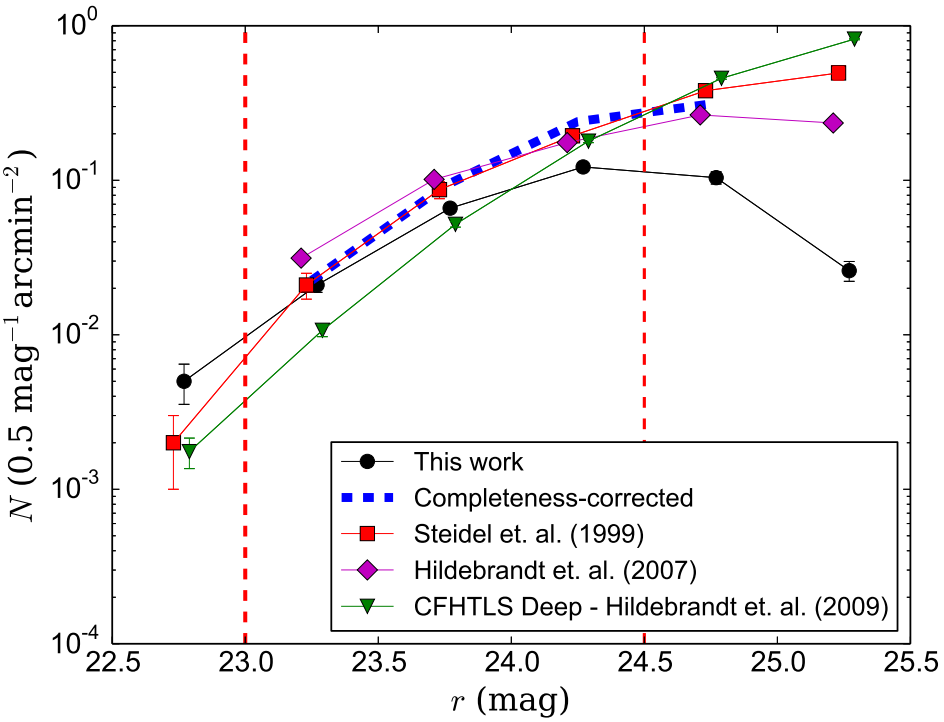

Figure 3.16: Number counts of the SpARCS u-dropout sample compared to previous work at wavelengths that roughly match the same rest-frame in the UV. The blue-dashed line represents the completeness-corrected u-dropouts number counts we measure.

A comparison between the u-dropout number counts as a function of magnitude in our sample with other work can be seen in Figure 3.16. The black circles trace the u-dropout number counts we estimate from the data. We estimate the fraction of LBGs that are lost due to the limited depth of the data from simulations similar to the ones used in (Hildebrandt et al. 2009). We create mock catalogues of SpARCS depth as well as CFHTLS-Deep depth, the latter of which are highly complete down to the magnitude limit of SpARCS. Using the ratio of the number counts between the two catalogues as an incompleteness correction for fainter magnitude bins, the number density of dropouts matches very well with other measurements in the literature, as shown by the blue-dashed line. Note that this correction is just used for this figure and not used in the subsequent analysis. Due to the large survey volume, the cosmic variance contribution can safely be neglected.

Applying the magnitude cuts and masks to the catalogues, and after the manual rejection of false LBGs, we select 16 242 u-dropouts with magnitudes in the interval range $23 \leq r \leq 24.5$, located at a mean redshift of $z \sim 3.1$. This magnitude range is chosen to minimize as much as possible low-redshift contamination, while still having a sufficient number of galaxies for a meaningful measurement.

Another peculiarity of using LBG as sources is that we must model the redshifts of contaminants to be able to minimize their influence on the measurements. As seen in Figure 3.17, there is practically no overlap between sources and lenses at high red-

shifts. Additionally, we measure the cross-correlation for a sample of clusters that does not include the low-redshift region $z < 0.3$, to control for, and reduce the possibility of having a positive signal from low-redshift, physically-induced cross-correlations. We find that since there are very few clusters with $0.2 \leq z \leq 0.3$, there is almost no difference if we either include or exclude them from the measurements.

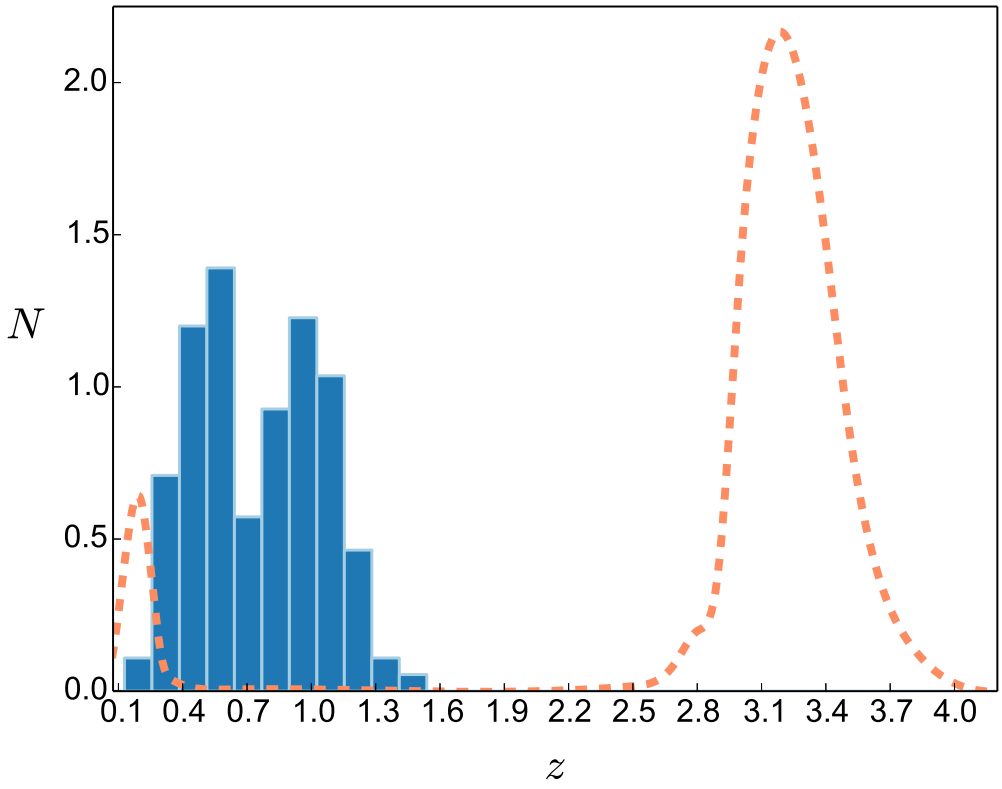

Figure 3.17: Histogram of the redshift distribution of SpARCS clusters (with total counts normalized to unity) and the redshift probability distribution function of the LBG candidates (orange dashed line).

Detailed properties of the LBG populations selected using the same methods have been described by Ford et al. (2014) and Hildebrandt et al. (2013).

CHAPTER 4

Galaxy clusters in SpARCS

Sections of this chapter have already been published in Tudorica et al. (2017).

4.1 Magnification of Number Counts

In terms of κ and γ, the convergence and shear, we can describe to first order the image deformation from the source to the observer frame through the Jacobian matrix $\mathcal{A}$:

$$\mathcal{A} = \begin{pmatrix} 1-\kappa-\gamma_1 & -\gamma_2 \\ -\gamma_2 & 1-\kappa+\gamma_1 \end{pmatrix}. \tag{4.1}$$

The magnification factor μ is the inverse of the determinant (Bartelmann & Schneider 2001):

$$\mu = \frac{1}{\det\mathcal{A}} = \frac{1}{(1-\kappa)^2 - |\gamma|^2}, \tag{4.2}$$

where $|\gamma|^2 = \sqrt{\gamma_1^2 + \gamma_2^2}$; γ_1 and γ_2 representing the shear components.

The magnification produced by a gravitational lens can be detected through the change from inherent (N_0) to observed (N) differential number counts of background sources:

$$N(m)\,\mathrm{d}\,m = \mu^{\alpha-1} N_0(m)\,\mathrm{d}m\,, \tag{4.3}$$

(Narayan 1989), where m is the apparent magnitude of sources, and $\alpha \equiv \alpha(m)$ is proportional to the logarithmic slope of the source number counts as:

$$\alpha = \alpha(m) = 2.5\frac{\mathrm{d}}{\mathrm{d}m}\log N_0(m)\,. \tag{4.4}$$

This means that the observed spatial source density of lensed galaxies can either increase or decrease, depending on the sign of $\alpha - 1$. Galaxies with number counts

where $(\alpha - 1) > 0$ will appear to be spatially correlated with the position of lenses, while for $(\alpha - 1) < 0$ an anti-correlation will be observed. There is no effect in the case of $(\alpha - 1) \approx 0$, since the dilution and amplification effect will mutually cancel out.

For the cross-correlation measurement between the positions of galaxy clusters and LBG candidates, we assigned a weight factor for each source of $\alpha - 1$, according to its position on the luminosity function (magnitude) (Scranton et al. 2005; Ménard et al. 2003).

To estimate the optimal weight factor $\alpha - 1$ required for both the measurement and its interpretation, we relied on external LBG luminosity function measurements for the characteristic magnitude M^* and faint-end slope $\alpha_{\rm LF}$ (van der Burg et al. 2010). For the u-dropouts $M^* = -20.84$ and $\alpha_{\rm LF} = -1.6$

$$\alpha = 10^{0.4(M^* - M)} - \alpha_{\rm LF} - 1\,. \tag{4.5}$$

LBGs selected using our method occupy a narrow region in redshift space centred around $z \approx 3.1$, which we approximate with a Dirac Delta function at the centre of the distribution. The validity of the approximation is supported by the fact that the angular diameter distance, on which the lensing signal depends, does not change significantly over the narrow range of the distribution.

4.2 Magnification Model

The magnification signal from galaxy clusters was modelled using the Navarro-Frenk-White (NFW) profile and a two-halo term from large-scale structure, as well as taking the effects of halo miscentering into account.

The convergence and shear were modelled as the sum of two terms:

$$\kappa(z) = \left[\Sigma_{\rm NFW}(z) + \Sigma_{\rm 2halo}(z)\right] / \Sigma_{\rm crit}, \tag{4.6}$$

$$\gamma(z) = \left[\Delta\Sigma_{\rm NFW}(z) + \Delta\Sigma_{\rm 2halo}(z)\right] / \Sigma_{\rm crit}\,, \tag{4.7}$$

where $\Sigma_{\rm crit}(z)$ is the critical surface mass density at the lens redshift, $\Sigma_{\rm NFW}$ is the surface mass density from the NFW halo, $\Sigma_{\rm 2halo}$ corresponds to the critical surface mass density from the two-halo term and $\Delta\Sigma$ represents the differential surface mass density.

The full expressions for the the surface mass density and differential surface mass density dependence on the dimensionless radial distance $x = R/r_s$ of an NFW lens as given by Bartelmann (1996); Wright & Brainerd (2000) are:

$$\Sigma_{\rm NFW}(x) = \begin{cases} \frac{2 r_s \delta_c \rho_{crit}(z)}{(x^2-1)} \left[1 - \frac{2}{\sqrt{1-x^2}} \operatorname{arctanh} \sqrt{\frac{1-x}{1+x}}\right] & (x < 1) \\ \frac{2 r_s \delta_c \rho_{crit}(z)}{3} & (x = 1) \\ \frac{2 r_s \delta_c \rho_{crit}(z)}{(x^2-1)} \left[1 - \frac{2}{\sqrt{x^2-1}} \arctan \sqrt{\frac{x-1}{1+x}}\right] & (x > 1) \end{cases} \tag{4.8}$$

and for the differential surface mass density:

$$\Delta\Sigma_{\rm NFW}(x) = \begin{cases} \frac{4}{x^2} r_s \delta_c \rho_{crit}(z) \left[\frac{2}{\sqrt{1-x^2}} \text{arctanh} \sqrt{\frac{1-x}{1+x}} + \ln\left(\frac{x}{2}\right) \right] (x < 1) \\ 4 r_s \delta_c \rho_{crit}(z) \left[1 + \ln\left(\frac{1}{2}\right) \right] \qquad (x = 1) \\ \frac{4}{x^2} r_s \delta_c \rho_{crit}(z) \left[\frac{2}{\sqrt{x^2-1}} \arctan \sqrt{\frac{x-1}{1+x}} + \ln\left(\frac{x}{2}\right) \right] (x > 1) \end{cases} \tag{4.9}$$

The critical surface mass density can be described in terms of the angular diameter distances between observer-lens $D_{\rm l}$, observer-source $D_{\rm s}$ and between lens-source $D_{\rm ls}$, the gravitational constant G and the speed of light C (not to be confused with the concentration parameter, c):

$$\Sigma_{\rm crit} = \frac{C^2}{4\pi G} \frac{D_{\rm s}}{D_{\rm l} D_{\rm ls}} \,. \tag{4.10}$$

The NFW density profile is given by:

$$\rho(r) = \frac{\delta_{\rm c}\, \rho_{\rm crit}(z)}{(r/r_{\rm s})\,(1 + r/r_{\rm s})^2} \,, \tag{4.11}$$

where $\rho_{\rm crit}(z)$ is the critical density at the halo redshift z:

$$\rho_{\rm crit}(z) = \frac{3H^2(z)}{8\pi G} \,. \tag{4.12}$$

$H(z)$ is the Hubble parameter at the same redshift, G is Newton's constant, the scale radius is given by $r_{\rm s} = r_{200}/c$, where c is the dimensionless concentration parameter, and the characteristic halo over-density $\delta_{\rm c}$ is given by:

$$\delta_{\rm c} = \frac{200}{3} \frac{c^3}{\ln(1+c) - c/(1+c)} \,. \tag{4.13}$$

The radius r_{200} is defined as the radius inside which the mass of the halo is equal to $200\,\rho_{\rm crit}$ (see Navarro et al. 1997).

$\Sigma_{\rm 2halo}$ quantifies the contribution of neighbouring halos to the surface mass density and is given by Johnston et al. (2007) as:

$$\Sigma_{\rm 2halo}(R, z) = b_{\rm l}\,(M_{200}, z)\,\Omega_{\rm M}\,\sigma_8^2\,D(z)^2\,\Sigma_{\rm l}(R, z) \,, \tag{4.14}$$

with

$$\Sigma_{\rm l}(R, z) = (1+z)^3 \rho_{\rm crit}(0) \int_{-\infty}^{\infty} \xi\left((1+z)\sqrt{R^2 + y^2}\right) {\rm d}y \,, \tag{4.15}$$

and

$$\xi(r) = \frac{1}{2\pi^2} \int_0^{\infty} k^2 P(k) \frac{\sin kr}{kr} {\rm d}k \,, \tag{4.16}$$

where r is the comoving distance, $D(z)$ is the growth factor, $P(k)$ is the linear matter power spectrum, and σ_8 is the amplitude of the power spectrum on scales of $8\,h^{-1}$Mpc. The lens bias factor b_l is approximated by Seljak & Warren (2004) with:

$$b_\mathrm{l}(x = M/M_\mathrm{nl}(z)) = 0.53 + 0.39x^{0.45} + \frac{0.13}{40x + 1} + 5 \cdot 10^{-4}x^{1.5}\,, \tag{4.17}$$

where the nonlinear mass M_nl, is defined as the mass within a sphere for which the root mean square fluctuation amplitude of the linear field is 1.68.

Cluster miscentering was taken into account statistically in the model by shifting the cluster centers with a radial offset following a 2-D Gaussian probability distribution (see Fig. 1 in Ford et al. 2014). This had the net effect of smoothing the surface mass density at small scales for the NFW-2halo term model used.

The cross-correlation $w(R)$ between the position of galaxy cluster centres and positions of LBG candidates was measured in seven logarithmic physical radial bins to 3.5 Mpc.

By stacking in physical radial bins instead of angular bins, we ensured that mixing clusters of different redshifts does not stack the magnification signal from different physical scales. We measured the magnification signal for each cluster sub-sample, each time drawing randoms 1000 times the size of the sources catalogue and with the same masking layout to account for the survey geometry. Since we only had one single measurement per pointing, we did not draw random catalogues for the clusters as well, summing instead the pairs for each angular bin for all clusters in the sample:

$$\mathrm{w}(R) = \frac{S^{\alpha-1}L - \langle\alpha - 1\rangle LR_*}{LR_*}\,, \tag{4.18}$$

where L stands for lenses, $S^{\alpha-1}$ for optimally-weighted sources and R_* for randoms. The terms represent normalized pair counts in physical radial bins.

Full covariance matrices are estimated for each set of independent measurements directly from the data (see Fig. 4.1 for the covariance matrix of the entire sample of measurements).

Assigning a constant weight for all LBG changes results only very slightly since the slope of the number counts does not change much over the magnitude interval where we perform our measurements.

To avoid entering the strong lensing regime in the innermost regions of clusters, we restricted our measurements and the model to radii larger than 1.5 times the Einstein radius. For convenience, we use the Einstein radius θ_E for an isothermal sphere, which is given by:

$$\theta_\mathrm{E} = 4\pi\left(\frac{\sigma_\mathrm{v}}{C}\right)^2 \frac{D_\mathrm{ls}}{D_\mathrm{s}}, \tag{4.19}$$

where σ_v is the velocity dispersion in km s^{-1}, calculated using Equation 1 of Munari et al. (2013):

$$\sigma_{\rm v} = 1100 \cdot \left[\frac{h(z) M_{200}}{10^{15} {\rm M}_{\rm Sun}} \right]^{1/3} , \tag{4.20}$$

where h(z) is the dimensionless Hubble parameter at redshift z.

We calculated $\theta_{\rm E}$ for each cluster and discarded the measurements performed at radii smaller than 1.5 times of this value. As $\theta_{\rm E}$ is usually smaller than the innermost bin edge, only a small proportion of the measurements is lost this way. We accounted for this by restricting the model to the same radii as the data. This is necessary because the mass-richness relation we use for calibration results in clusters massive enough to have their $\theta_{\rm E}$ within our measurements range, which induces model instability and artefacts.

4.2.1 Signal-to-Noise Ratio Estimates

To estimate the expected signal-to-noise ratio we used the methods derived by Van Waerbeke et al. (2010). As the signal-to-noise ratio is so low for most individual clusters that direct measurements of the signal are impossible, we rely on stacking multiple foreground lenses to decrease the noise of the average magnification as a function of the distance from cluster centres. The average mass and concentration parameters (M_{200} and c_{200}) of the lenses that contribute to the average magnification profile can then be constrained with the likelihood:

$$\mathcal{L} \propto \exp\left[(\delta_{\rm N}(\theta) - \bar{\delta}_{\rm N}(\theta)) C^{-1}_{\delta_{\rm N}\delta_{\rm N}} (\delta_{\rm N}(\theta) - \bar{\delta}_{\rm N}(\theta))^{\mathbf{T}} \right] , \tag{4.21}$$

where $\delta_{\rm N}(\theta)$ is the mean galaxy radial counts contrast profile that we are measuring, and $\bar{\delta}_{\rm N}(\theta)$ is the galaxy count profile model. The noise covariance matrix, $C_{\delta_{\rm N}\delta_{\rm N}}$, is estimated by choosing 200 random positions for which we estimate their angular correlation function with our LBG candidates sample. As expected, the angular correlation is consistent with zero and the dispersion around the mean corresponds to the $C_{\delta_{\rm N}\delta_{\rm N}}$ matrix elements. We then scale the amplitude of the noise covariance matrix to match the actual number of lenses that we use. This method ensures that the halo sampling and clustering noise of the source population are appropriately taken into account. By maximizing the likelihood function we find an expected signal-to-noise ratio of about 10 for using all lenses in our sample and 6 for halos with $z \geq 0.80$.

4.3 Composite-Halo Fits

The weak lensing magnification contribution to the cross-correlation signal can be calculated as follows:

$$w_{\rm lensing}(R) = \frac{1}{N_{\rm lens}} \sum_{i=1}^{N_{\rm lens}} \langle (\alpha - 1)^2 \rangle_i \left[\mu(R, M_{200})_i - 1 \right] , \tag{4.22}$$

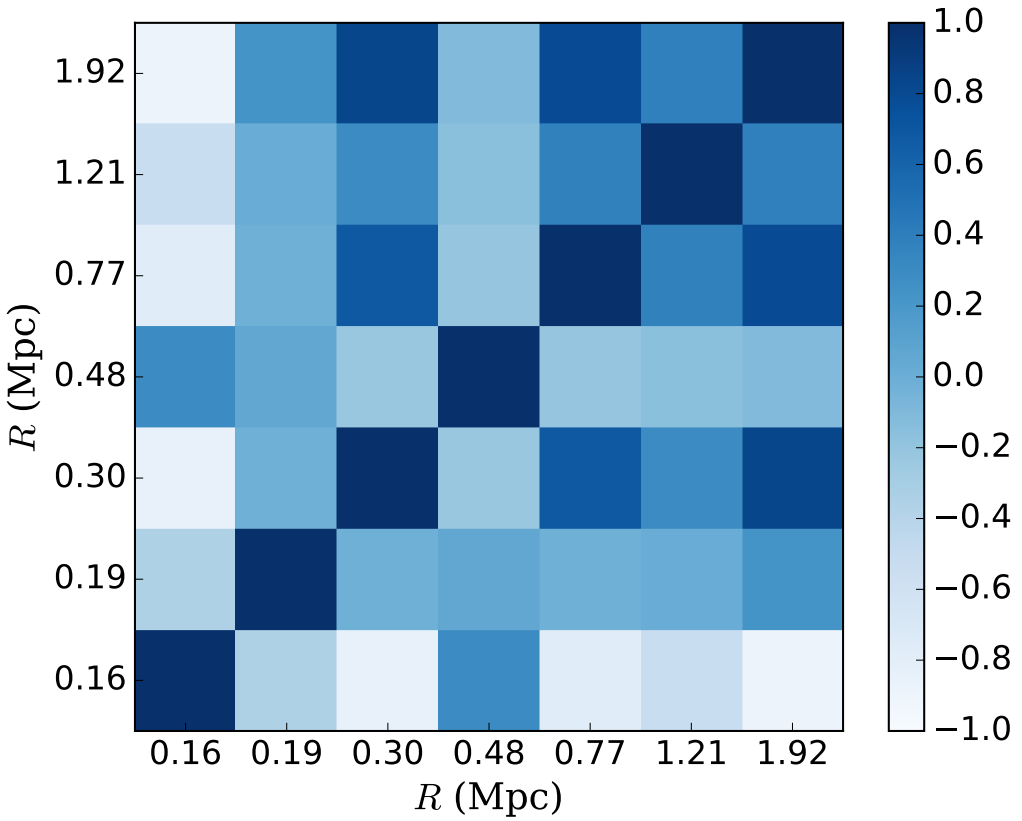

Figure 4.1: Correlation matrix (normalized covariance matrix) of the optimally-weighted cross-correlation function between *u*-dropouts and the centres of galaxy clusters.

where the sum is over the number of clusters (lenses) in a given sample selected for stacking.

Our results are not too sensitive to the choice of the mass-concentration relation and we chose the one developed by Duffy et al. (2008) to fix the halo concentration parameter c (see Equation 4.13):

$$c = A_{200}(M_{200}/M_{\rm pivot})^{B_{200}}(1 + z_{\rm cluster})^{C_{200}}\,, \tag{4.23}$$

where $A_{200} = 5.71$, $B_{200} = -0.084$, $C_{200} = -0.47$, $M_{\rm pivot} = 2 \times 10^{12}$ and $z_{\rm cluster}$ is the redshift of the lens.

However, since we needed a mass to fix the halo concentration parameter, we first made use of the mass-richness relation determined from the GCLASS cluster sample:

$$M_{200} = a\, N_{\rm red}^{2.97\pm 0.26} \times 10^{10.63\pm 0.39}\,. \tag{4.24}$$

The richness values for the GCLASS sample are Eddington-biased high, given that the GCLASS sample was selected from the main SpARCS sample due to high $N_{\rm red}$ values.

The sole fit parameter in our measurement was the amplitude of the scaling relation between mass and richness a (see Equation 4.24). We used only the central value of Eq. 4.24 for the fitting procedure. The fit was performed by varying a and minimizing the reduced χ^2 between the magnification model described above and the cross-correlation measurement. We also added for comparison in Fig. 5.5 the mass-richness relation determined by Muzzin et al. (2007) for the Canadian Network for Observational Cosmology (CNOC1, see Yee et al. 1996) set of clusters, a survey of 16 rich galaxy clusters with $0.17 < z < 0.55$:

$$M_{200} = (69.4\, N_{\rm red})^{1.62\pm 0.24} \times 10^{9.86\pm 0.77}\,. \tag{4.25}$$

We used the full covariance matrix (shown in Fig. 4.1), as determined from the measurements themselves, to find the minimum reduced χ^2.

Assuming statistically-independent data points (bins) and idealized Gaussian noise, the inverse of the maximum-likelihood estimator of the covariance is biased, with an amount depending on the ratio between the number of bins and independent measurements. Hartlap et al. (2007) have determined a correction factor (see their Eq. 17) which we applied here to avoid underestimating the error bars.

4.3.1 Masking Correction

Another effect that could disrupt our measurement would be the fact that galaxy cluster candidate galaxies are effectively masking some of the LBG candidates in the background. Umetsu et al. (2011) have developed a method of estimating the amount of masking based on deep Subaru imaging data for a sample of 5 massive clusters ($\geq 10^{15}\,{\rm M}_{\odot}$) at intermediate redshifts ($0.18 \leq z \leq 0.45$). The study found that while at large radii the masking is insignificant, amounting to only a few percent, at small radii the cluster galaxies can occupy even 10-20 percent of the annulus area.

To correct for this additional masking, we adopted a simple method similar to that described by Umetsu et al. (2011) in their Appendix A. We selected all objects brighter than *r*-band magnitude 24.5 (the LBG candidates' magnitude limit) and fainter than *r*-band magnitude 16 (where our automatic masking procedure would have already masked the objects). The area of every object was taken to be the isophotal area above the detection threshold of 2.5σ. For each cluster, the area of the objects was summed at every corresponding radial bin to calculate the proportion of area covered, with which the magnification signal was boosted. For all cluster samples, we average the correction factors f_{mask} and take the errorbars as their 1σ standard deviation. Figure 4.2 shows that the masking fraction depends only slightly on the redshift of lenses, while for clusters of different richness we do not find a significant variation of the masking fraction amplitude.

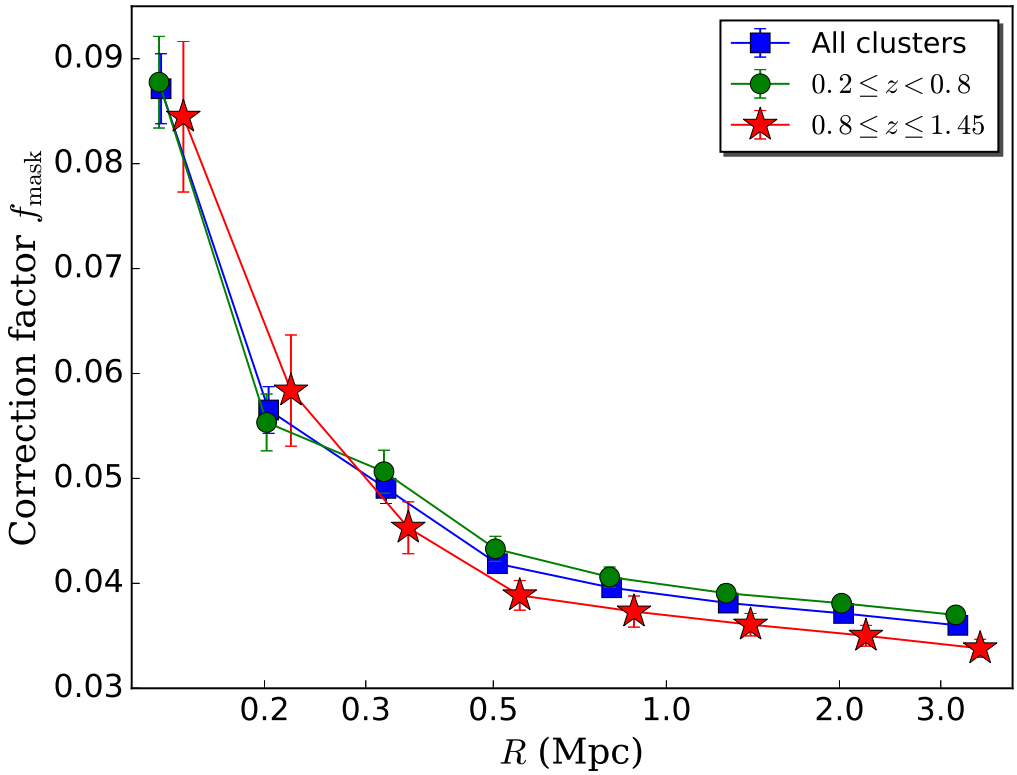

Figure 4.2: Masking correction factors f_{mask} as a function of the redshift of cluster samples. The data points are slightly shifted on the x-axis for the sake of clarity.

Although Umetsu et al. (2011) find almost twice the amount of masking we find at small annuli, this difference can most likely be explained by the slight differences in methodology, by the fact that the only cluster for which they have published the masking correction is a highly unusual one (the very massive and rich Abel 1689) and because at low redshift the galaxies are larger down to a given surface brightness.

CHAPTER 5

Results and discussion

This chapter has already been published in Tudorica et al. (2017).

Results

We split the cluster sample in several redshift bins, as can be seen in Fig. 5.1. The uncertainty estimate on w(R) is computed by jackknife resampling over the measurements for all clusters included in the respective bin, while the lines show the best-fit model to the data. The redshift $z = 0.8$ is chosen as marking the transition between the low and high-redshift samples based on the number of clusters available in each bin, with the main catalogue roughly split in half at this value.

The measurement is carried out also on cluster samples binned in richness (see Fig. 5.2), with one sample containing all clusters with $10 \leq N_{\rm red} \leq 12$ and the other containing only the richest clusters in the sample, with $12 \leq N_{\rm red} \leq 37$. The first panel of Fig. 5.2) also shows (with red filled circles) the signal measured for large number of mock lenses situated at random positions in our survey. We measure the signal in various bins of redshift and richness of different widths, which can be seen in Fig. 5.3. This particular binning is chosen in order to maximise the expected signal-to-noise (see Sec. 4.2.1) by taking into account both the lensing efficiency as a function of angular diameter distance and keeping a roughly constant number of clusters below which the measurement errors become too large. Experimenting with our data set and bins of various widths, we find that in order to keep the measurement uncertainties to an acceptable level, a number of at least 50 clusters per bin is desirable.

In all richness and redshift bins we measure the indicative signature of magnification with detection significances between 2.6σ and 5.5σ.

It is difficult to compare our results for the mass-richness relation directly with other studies. $N_{\rm red}$, the richness proxy that we use, is not defined the same way as other richness estimates, and other studies will obtain different scaling relations depending

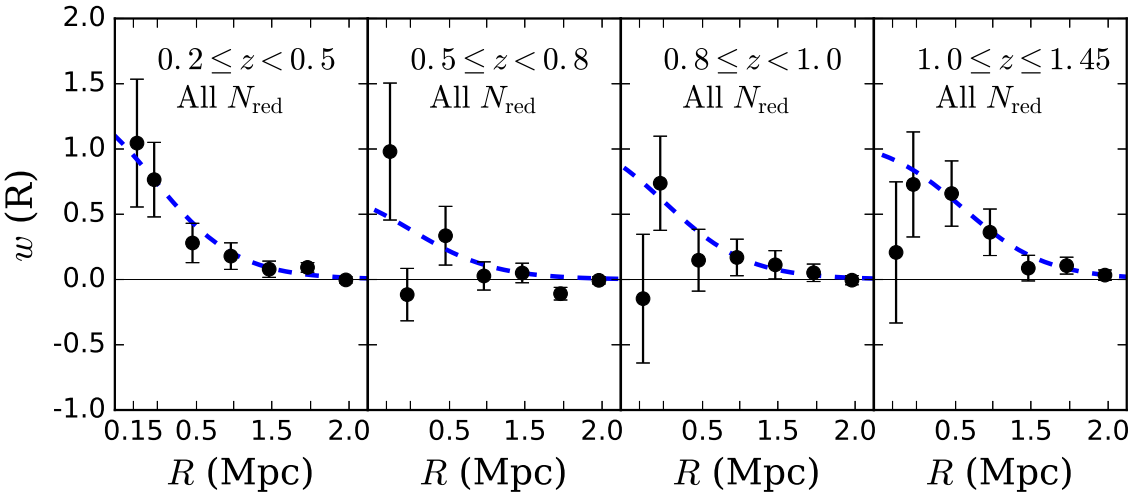

Figure 5.1: Angular cross-correlation measurements between the *u*-dropouts and the centres of galaxy clusters, as a function of the radial distance from the cluster centres in physical units. The sample of galaxy clusters on which the measurement was performed is binned in redshift as shown in each of the figure legends. Best-fit models are plotted with the dotted blue line, while our measurements are represented by the black round points.

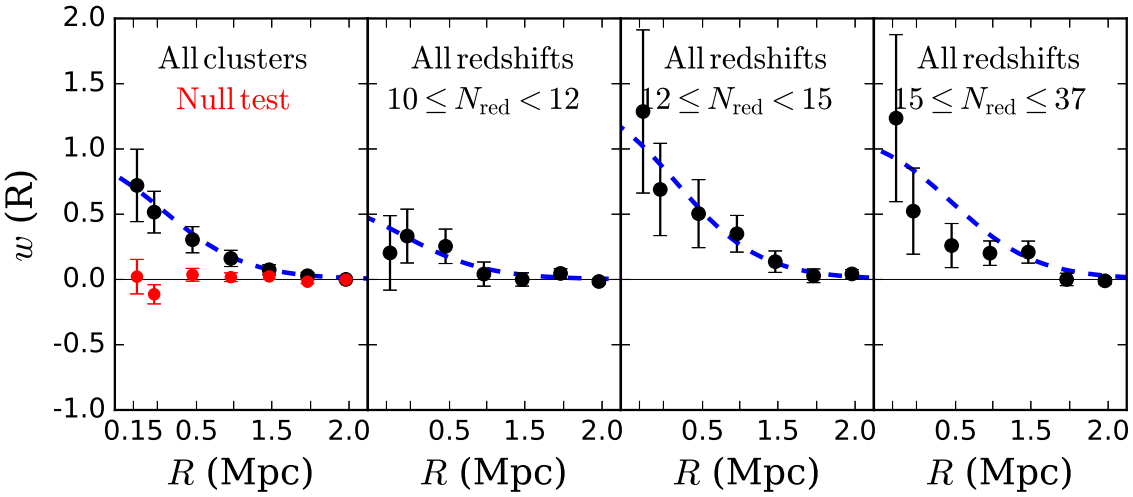

Figure 5.2: Same as in Fig. 5.1, but with the cluster samples binned in richness instead of redshift. The red circles in the leftmost panel show the cross-correlation signal measured at random lens positions in our fields.

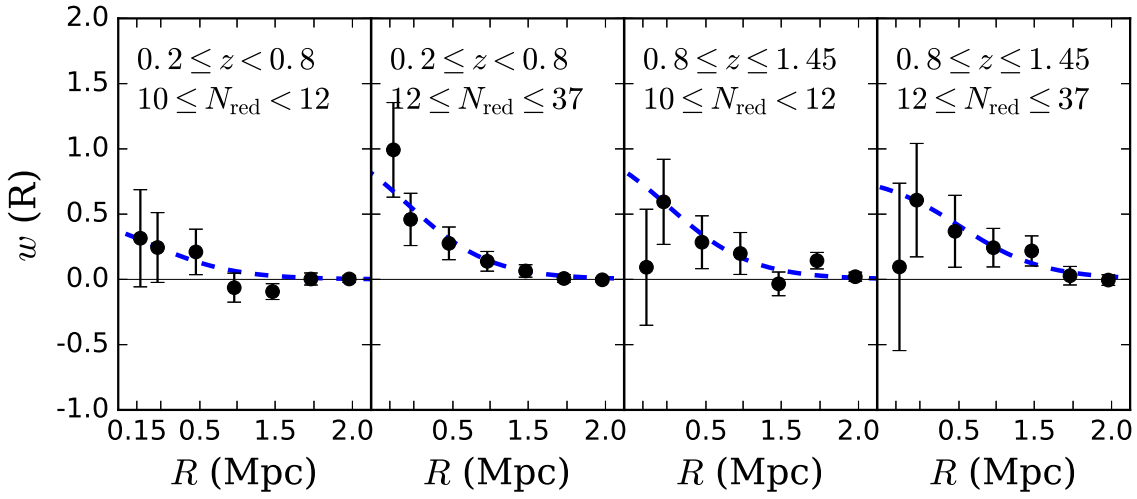

Figure 5.3: Same as in Fig. 5.1, but with the cluster samples binned in richness and redshift as indicated in each panel.

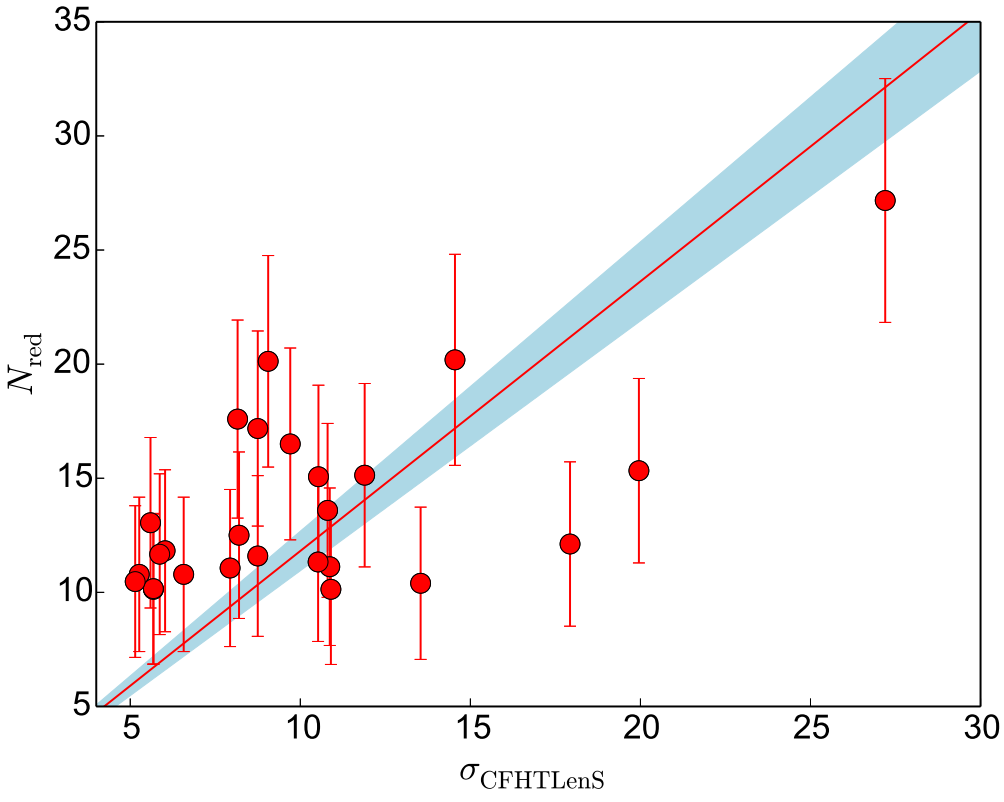

Figure 5.4: Richness proxies for the galaxy cluster candidates common to CFHTLenS and SpARCS. The best fit linear relation of the form $y = ax$ between the two quantities is shown by the continuous red line, while the associated fitting 1σ uncertainties are shown by the shaded region.

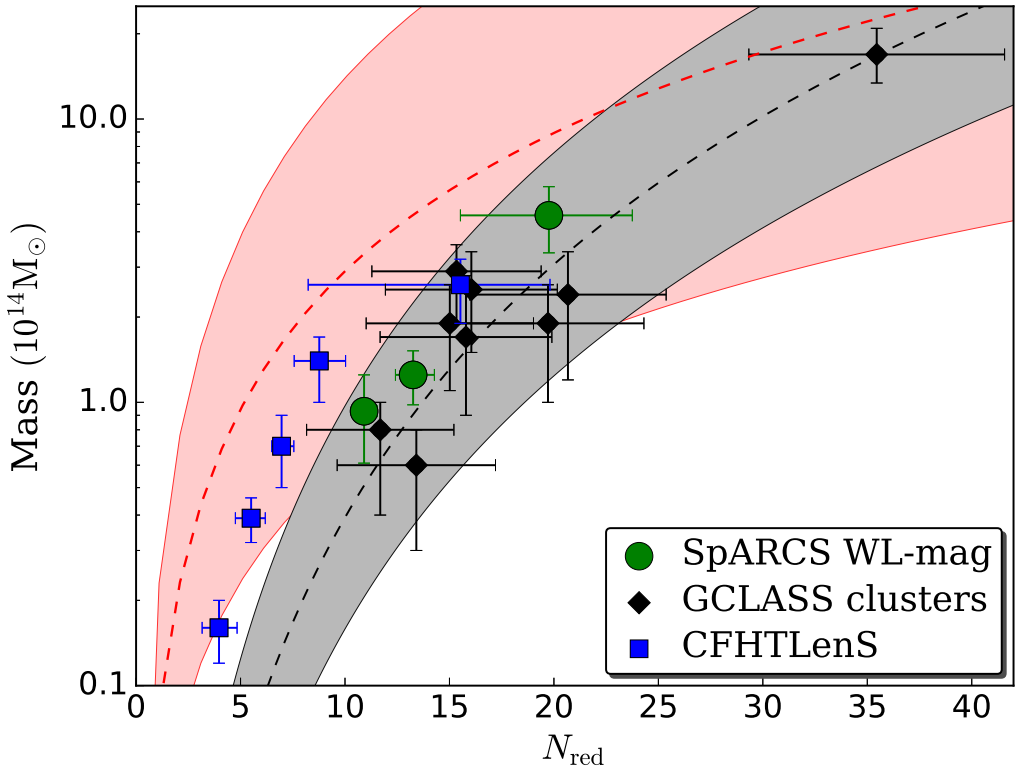

Figure 5.5: Mass and richness for the SpARCS cluster samples (green filled circles) compared to the the CFHTLenS analysis results (Ford et al. 2014), where the corresponding values are transformed into the $N_{\rm red}$ parameter as described in the text (blue filled squares). The errors of the CFHTLenS data points have the fit uncertainty from Fig. 5.4 propagated as well. The red dashed line shows the mass-richness relation from Eq. 4.25, with its uncertainty represented by the red shaded region, while the GCLASS-based mass-richness relation (Eq. 4.24) is shown by the black dashed line and respectively the shaded grey area.

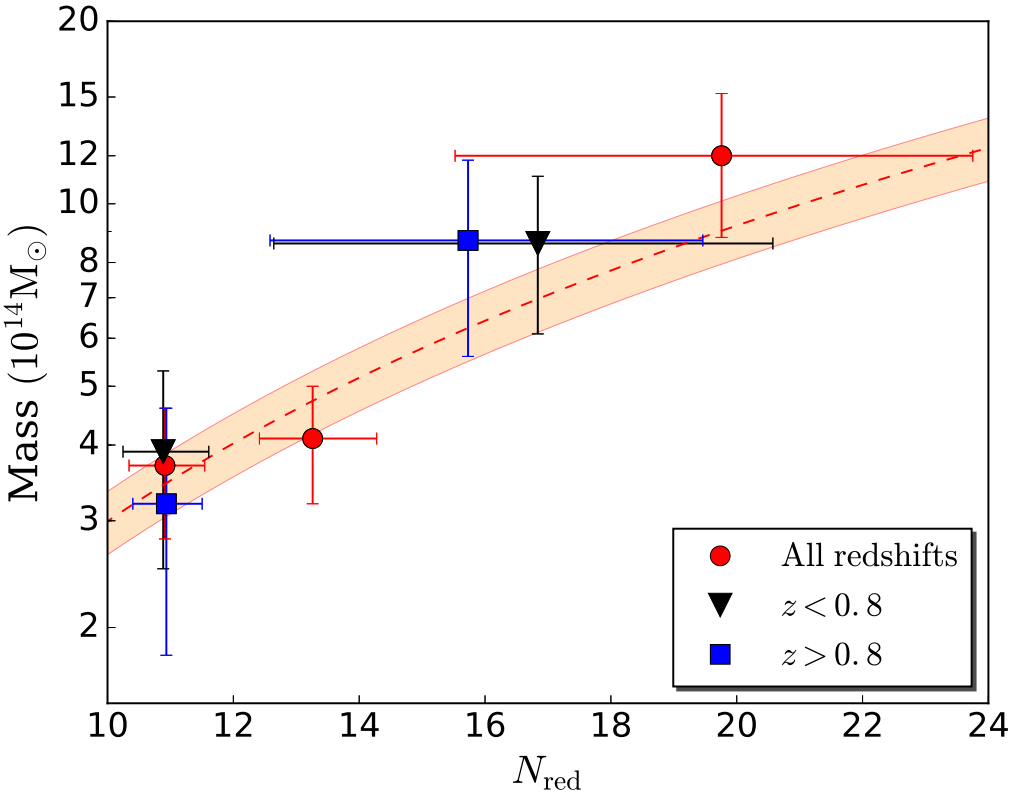

Figure 5.6: Mass-richness relation for the SpARCS cluster samples as a function of redshift. The dotted line and shaded region represent the best-fit mass-richness relation amplitude for all z, while the associated fit uncertainty is shown by the shaded region. The errorbars on the x-axis represent the ranges in $N_{\rm red}$ delimited by the 16$^{\rm th}$ and 84$^{\rm th}$ percentile for each sample.

on this particular choice, as well as on the details of the cluster detection algorithms. The uncertainties in estimating the richness parameter $N_{\rm red}$ are not propagated further in our analysis. Fortunately, the CFHTLenS survey partly overlaps with the SpARCS area. The CFHTLenS (Heymans et al. 2012; Erben et al. 2013) cluster catalogue is based on employing the 3D-Matched-Filter cluster-finder of Milkeraitis et al. (2010), with cluster candidates spanning a wide range of masses ($10^{13}-10^{15}\,M_{\odot}$) and redshifts ($0.2 < z < 0.9$). We find a number of 26 clusters with a high detection significance common to both catalogues, at similar redshifts and with a maximum separation smaller than 60arcsec. $\sigma_{\rm CFHTLenS}$ represents the significance of the likelihood peak relative to the background signal; (see Eq. 5 of Milkeraitis et al. 2010, for a detailed explanation).

Muzzin et al. (2007) and Ford et al. (2014) utilize different definitions for richness and therefore we transform the latter into the $N_{\rm red}$ parameter. To do so, we fit a linear relation that goes through the origin to the richness proxies used in the two studies, $N_{\rm red}$ SpARCS and $\sigma_{\rm CFHTLenS}$, which can be seen in Fig. 5.4. The fitting errors represented in Fig. 5.4 by the shaded region are propagated into the x-range errorbars for the CFHTLenS data points. Since the mass measurement results in Ford et al. (2014) are given as a function of N_{200} instead of $\sigma_{\rm CFHTLenS}$, we include an additional conversion between these two parameters, which provides the result plotted in Fig. 5.5. We chose to first find the relation between the CFHTLenS σ and $N_{\rm red}$ because they are similar richness estimates and scale well together, unlike N_{200} and $N_{\rm red}$. There are a number of caveats to this comparison, such as additional uncertainties and systematic biases that we do not take into account. Among these, probably most important are the fact that only a very small number of clusters is common to the two studies, which could introduce selection bias effects, as well as the rather large cut-off in separation when matching the two catalogues, which could mean that some clusters are erroneously matched.

Figure 5.5 shows the mass and richness derived from our measurements (as shown with the green filled circles) and results from the methodologically-similar study based on CFHTLenS data (blue filled squares), as well as the GCLASS clusters (black diamonds).

Figure 5.6 shows the mass-richness relation for the most relevant $N_{\rm red}$ and redshift bins, as well as the best-fit mass-richness relation and its uncertainty, shown with the dotted line and respectively the shaded region. The horizontal error bars for the SpARCS measurements represent the ranges in $N_{\rm red}$ delimited by the $16^{\rm th}$ and $84^{\rm th}$ percentile for each sample. We do not observe a clear trend of the mass-richness relation with redshift.

We select the six GCLASS clusters that are within the area covered by the CFHT pointings for measuring the magnification signal. However, the measurement appears to be too noisy for a meaningful interpretation, which can be explained by insufficient number density of the *u*-dropouts.

Table 5.1: Results of the mass measurements for cluster samples binned in redshift and richness (see Fig. 5.1 and Fig. 5.2).

Sample description	Redshift (z)	$N_{\rm red}$	$\langle N_{\rm red}\rangle$	Sample size (N)	$\langle M_{200}\rangle$ $\left(10^{14}\,{\rm M}_\odot\right)$	$\chi^2_{\rm red}$	S/N	a
z-bins	0.2 – 1.4	10-37	13.9	287	$1.28^{+0.23}_{-0.21}$	0.8	5.5	$1.21^{+0.22}_{-0.20}$
	0.2 – 0.5	10-37	14.5	71	$1.56^{+0.30}_{-0.31}$	1.4	4.6	$1.30^{+0.25}_{-0.26}$
	0.5 – 0.8	10-37	14.4	83	$1.31^{+0.31}_{-0.27}$	2.2	3.5	$1.11^{+0.26}_{-0.23}$
	0.8 – 1.0	10-37	13.3	67	$1.19^{+0.27}_{-0.33}$	1.9	2.6	$1.28^{+0.29}_{-0.36}$
	1.0 – 1.4	10-37	12.8	66	$1.03^{+0.24}_{-0.28}$	2.3	4.1	$1.24^{+0.29}_{-0.34}$
$N_{\rm red}$-bins	0.2 – 1.4	10-12	10.9	134	$0.93^{+0.32}_{-0.21}$	1.8	3.2	$1.81^{+0.62}_{-0.41}$
	0.2 – 1.4	12-15	13.3	77	$1.25^{+0.27}_{-0.23}$	2.5	4.4	$1.35^{+0.29}_{-0.25}$
	0.2 – 1.4	15-37	19.5	75	$4.57^{+1.25}_{-1.16}$	3.2	4.0	$1.53^{+0.42}_{-0.39}$
high-z-bins	0.8 – 1.4	10-12	10.9	67	$0.87^{+0.20}_{-0.22}$	2.6	3.1	$1.69^{+0.39}_{-0.43}$
	0.8 – 1.4	12-37	15.8	66	$3.44^{+1.14}_{-1.19}$	2.4	3.0	$2.22^{+0.74}_{-0.77}$
low-z-bins	0.2 – 0.8	10-12	10.9	61	$1.20^{+0.41}_{-0.38}$	1.6	2.8	$2.33^{+0.80}_{-0.74}$
	0.2 – 0.8	12-37	16.9	93	$3.29^{+1.08}_{-1.11}$	1.7	4.4	$1.74^{+0.54}_{-0.59}$

Discussion

We discuss below some of the most important effects that we are not modelling and which could potentially impact our results and other measurements based on similar techniques.

Simulations by Hildebrandt et al. (2009) for a significantly deeper data set show that by using the cuts in magnitude that we also use, the contamination from stars and low-z interlopers is below 10% in each 0.5 magnitude interval. Since our data are shallower than the one for which Hildebrandt et al. (2009) assessed the contamination, this means that the interloper proportion might be higher in our sample, therefore contributing to a dilution of the signal strength (if more stars are added into the sample) or to an additional, unwanted, cross-correlation signal between low-redshift interlopers and the low-redshift cluster sample. To minimize the probability that there is a physical cross-correlation between low-redshift contaminants in our LBG candidates sample and low-redshift galaxy clusters, we also test a sample of cluster candidates with $0.3 \leq z < 0.8$. This however results in practically identical estimates with those given by the clusters in the $0.2 \leq z < 0.8$ bin, since there are very few cluster candidates with such a low redshift. Therefore low redshift contamination most likely does not play an important role for our measurements.

Besides the effective masking described in Sect. 4.3.1, cluster galaxies might have another critical influence on the detection of LBG candidates. When u-dropouts are in the angular proximity of cluster member galaxies, the measurement of their colours could possibly also be affected. In effect, this could shift the entire population of LBGs

that are close to cluster galaxies across colour space, either by increasing magnitude measurement errors (therefore including more fake candidates and rejecting real ones, thus increasing the overall noise of the measurement) or by consistently shifting LBGs in the colour space as a function of the overall galaxy cluster colours, thus creating a redshift-dependent effect.

Additionally, the method used by `SExtractor` for background subtraction results in under- and over-subtraction at various distances from the field galaxies, especially those of sizes closest to the smoothing kernel used to estimate the background map. The procedures `SExtractor` uses to separate partly blended objects is also of relevance and must be investigated in a comprehensive manner. Understanding these effects requires detailed simulations which go beyond the scope of this study and will be left to future research.

Increasing the total area by including the high quality DECam data available for the southern SpARCS fields and modelling these additional effects could be of great assistance in decreasing the noise and increasing especially the significance and precision of the high-redshift cross-correlation measurements. This would enable us to even more accurately calibrate the mass-richness relation at $z \geq 0.8$ and to use similar magnification-based methods for studying large samples of galaxy clusters with more precision and accuracy.

In this paper we discuss many different possible systematic errors in the measurement. We neglect several possible systematic effects on the modelling side that are usually addressed in the galaxy cluster literature, such as the effect of large-scale-structure along the line of sight, triaxiality of galaxy clusters, uncertainty in the M - c relation, etc. Given the size of our statistical errors we can be confident that such effects are subdominant at the moment and defer their treatment to future work.

CHAPTER 6

Summary and Conclusions

Summary and Conclusions

This chapter has already been published in Tudorica et al. (2017).

We used optically-selected LBGs to study a sample of galaxy cluster candidates by using the magnification bias induced by the weak gravitational lensing magnification effect. A total of 287 galaxy cluster candidates with a high detection significance were selected from the SpARCS catalogue, with redshifts ranging from 0.2 to 1.4 and richness (as defined by Muzzin et al. 2008) between 10 and 37. Using the Lyman-break technique on deep *ugriz* optical data from CFHT, we selected a background sample of 16 242 objects with a magnitude range of $23.0 \leq r \leq 24.5$ and situated at a redshift of $z \approx 3.1$, offering both a sufficient surface number density and good lensing efficiency. We cross-correlated the positions of the galaxy cluster candidates and the LBGs, using an external LBG luminosity function to calibrate our measurement. We fitted a composite NFW halo model that takes into account the richness and redshift ranges of the cluster candidate sample, as well as modelling contributions from the two-halo term, miscentering and low redshift contamination.

We report a 5.5σ detection significance for the weak lensing magnification signal w(R), measured for the entire cluster dataset. We found an average halo mass for the cluster sample with $0.2 \leq z \leq 1.4$ of $M_{200} = 1.28^{+0.23}_{-0.21} \times 10^{14}\,\mathrm{M}_{Sun}$. The cluster catalogue was divided in various richness and/or redshift bins, with the mass and normalization of the mass-richness relation parameter a estimates for each bin presented in Table 5.1. As we only fitted the amplitude a of a specific mass-richness relation, it is important that we use a representative mass-richness relation for the data. Ideally, we would fit both the normalisation and the slope, thus reducing the dependence on the exact shape of the mass-richness relation at the basis of the model fitting.

Although the contamination of the cluster catalogue with spurious detections is not known precisely, our results indicate that optical-IR selection of clusters does in fact

select real, massive over-densities even at very high redshift ($z \geq 1$) and is a promising and efficient method for selecting large samples of such objects with a relatively low observational effort. The significance of the measurement for clusters at high redshift ($z \geq 1$) is a remarkable 4.1 σ, thus further strengthening the case for using weak lensing magnification methods to calibrate the mass-richness relation for large samples of high redshift galaxy clusters.

Even if the mass-richness scaling relation is directly applicable only to the cluster sample from which it was obtained, the ease of measuring richness for any optical survey makes richness an important quantity to measure. A meta-study that would compare how different richness proxies relate to each other could provide a bridge for having more direct comparisons between studies.

Albeit the signal-to-noise ratio for mass measurements obtained using weak lensing shear methods is higher in general, considerable improvements in using magnification as a complementary method are achieved. Additionally, magnification probes the surface mass density of the lens directly, while shear measures the differential mass density, thus the combination of these two methods is able to break the lens mass-sheet degeneracy. Rozo & Schmidt (2010) have shown that survey-independent statistical gains of the order of 40% - 50% can be obtained by using the two types of measurements together.

Next generation surveys, such as Kilo Degree Survey (KiDS, de Jong et al. 2013), Euclid (Laureijs et al. 2011), Subaru Hyper Suprime-Cam (Takada 2010), Large Synoptic Survey Telescope (LSST, Ivezic et al. 2008), Dark Energy Survey (DES, The Dark Energy Survey Collaboration 2005), etc. will be expected to be able to take full advantage of the large areas covered, large number of background sources and excellent redshift estimates in order to use the combined strengths of weak lensing shear and magnification for a large class of cosmological and weak lensing science problems. Having a well understood and appropriately calibrated mass-richness relation before LSST starts providing large data sets is critical for enabling the measurement of M_{200} for an unprecedented large number of cluster from imaging data alone, thus enabling very accurate cosmological studies, such as greatly strengthening constrains on the dark energy equation of state from the cluster mass function.

APPENDIX A

CFHT Optical Data Properties

Properties of the CFHT optical data for each pointing (field) and filter. The typical magnitude zeropoint error is 0.1 magnitudes.

Table A.1: CFHT optical data properties per pointing per filter

Field name	Filter (name)	Exposure time (s)	Magnitude zeropoint (mag)	Seeing ($''$)	Images stacked (n)
ELAIS N1 P1	g	2899	26.47	0.89 ± 0.02	6
ELAIS N1 P1	r	2001	26.02	0.69 ± 0.01	4
ELAIS N1 P1	u	2751	25.21	1.00 ± 0.01	5
ELAIS N1 P1	z	6002	24.8	0.69 ± 0.01	10
ELAIS N1 P10	g	8697	26.41	0.88 ± 0.01	18
ELAIS N1 P10	r	5002	25.95	0.68 ± 0.01	10
ELAIS N1 P10	u	2751	25.21	0.80 ± 0.02	5
ELAIS N1 P10	z	6002	24.83	0.71 ± 0.01	10
ELAIS N1 P11	g	2416	26.39	0.81 ± 0.02	5
ELAIS N1 P11	r	5502	25.92	0.92 ± 0.02	11
ELAIS N1 P11	u	2751	25.15	0.98 ± 0.03	5
ELAIS N1 P11	z	6002	24.8	0.63 ± 0.01	10
ELAIS N1 P12	g	2899	26.47	0.85 ± 0.01	6
ELAIS N1 P12	r	2001	26.01	0.80 ± 0.01	4
ELAIS N1 P12	u	2751	25.17	0.98 ± 0.02	5
ELAIS N1 P12	z	6002	24.82	0.52 ± 0.01	10
ELAIS N1 P2	g	2416	26.46	0.90 ± 0.01	5
ELAIS N1 P2	r	2001	26.0	0.78 ± 0.01	4
ELAIS N1 P2	u	2751	25.1	0.84 ± 0.02	5
ELAIS N1 P2	z	6002	24.82	0.62 ± 0.01	10
ELAIS N1 P3	g	2416	26.45	0.78 ± 0.01	5
ELAIS N1 P3	r	2001	25.99	0.90 ± 0.01	4

Field name	Filter (name)	Exposure time (s)	Magnitude zeropoint (mag)	Seeing (″)	Images stacked (n)
ELAIS N1 P3	*u*	2751	25.21	0.85 ± 0.01	5
ELAIS N1 P3	*z*	7802	24.8	0.80 ± 0.01	13
ELAIS N1 P4	*g*	2416	26.49	0.81 ± 0.01	5
ELAIS N1 P4	*r*	2001	26.0	0.85 ± 0.01	4
ELAIS N1 P4	*u*	2751	25.2	0.91 ± 0.01	5
ELAIS N1 P4	*z*	6002	24.84	0.66 ± 0.00	10
ELAIS N1 P5	*g*	2416	26.48	0.83 ± 0.01	5
ELAIS N1 P5	*r*	2001	26.0	1.00 ± 0.01	4
ELAIS N1 P5	*u*	2751	25.16	0.83 ± 0.01	5
ELAIS N1 P5	*z*	6002	24.81	0.67 ± 0.01	10
ELAIS N1 P6	*g*	2416	26.45	0.73 ± 0.01	5
ELAIS N1 P6	*r*	2001	26.01	0.85 ± 0.01	4
ELAIS N1 P6	*u*	2751	25.25	0.94 ± 0.01	5
ELAIS N1 P6	*z*	6002	24.83	0.82 ± 0.01	10
ELAIS N1 P7	*g*	2416	26.41	0.82 ± 0.01	5
ELAIS N1 P7	*r*	5502	25.96	0.84 ± 0.01	11
ELAIS N1 P7	*u*	3301	25.18	0.94 ± 0.02	6
ELAIS N1 P7	*z*	7803	24.76	0.65 ± 0.01	13
ELAIS N1 P8	*g*	2416	26.47	0.82 ± 0.02	5
ELAIS N1 P8	*r*	2001	26.01	0.78 ± 0.04	4
ELAIS N1 P8	*u*	2751	25.27	0.72 ± 0.01	5
ELAIS N1 P8	*z*	6002	24.82	0.48 ± 0.00	10
ELAIS N1 P9	*g*	5798	26.43	0.89 ± 0.02	12
ELAIS N1 P9	*r*	6503	25.85	0.87 ± 0.01	13
ELAIS N1 P9	*u*	7703	25.17	0.93 ± 0.02	14
ELAIS N1 P9	*z*	6002	24.82	0.51 ± 0.01	10
ELAIS N2 P1	*g*	2416	26.49	0.69 ± 0.01	5
ELAIS N2 P1	*r*	2001	26.01	0.64 ± 0.01	4
ELAIS N2 P1	*u*	3006	25.23	0.76 ± 0.02	5
ELAIS N2 P1	*z*	6002	24.83	0.59 ± 0.01	10
ELAIS N2 P2	*g*	7731	26.35	0.82 ± 0.02	16
ELAIS N2 P2	*r*	4001	26.0	0.79 ± 0.03	8
ELAIS N2 P2	*u*	5411	25.05	0.89 ± 0.02	9
ELAIS N2 P2	*z*	6002	24.84	0.61 ± 0.00	10
ELAIS N2 P3	*g*	2416	26.4	0.94 ± 0.01	5
ELAIS N2 P3	*r*	2001	25.98	0.77 ± 0.03	4
ELAIS N2 P3	*u*	3607	25.17	0.79 ± 0.01	6
ELAIS N2 P3	*z*	6002	24.81	0.74 ± 0.01	10
ELAIS N2 P4	*g*	2416	26.43	0.84 ± 0.01	5
ELAIS N2 P4	*r*	4001	25.99	0.74 ± 0.01	8
ELAIS N2 P4	*u*	6012	25.2	0.86 ± 0.03	10
ELAIS N2 P4	*z*	6602	24.81	0.50 ± 0.00	11

Field name	Filter (name)	Exposure time (s)	Magnitude zeropoint (mag)	Seeing ($''$)	Images stacked (n)
ELAIS N2 P5	*g*	1933	26.49	1.01 ± 0.02	4
ELAIS N2 P5	*r*	2001	26.0	0.73 ± 0.01	4
ELAIS N2 P5	*u*	3006	25.26	0.77 ± 0.01	5
ELAIS N2 P5	*z*	6002	24.81	0.64 ± 0.01	10
Lockmann P1	*g*	2291	26.46	1.13 ± 0.03	5
Lockmann P1	*r*	2501	25.98	0.81 ± 0.01	5
Lockmann P1	*u*	6002	25.13	1.06 ± 0.01	10
Lockmann P1	*z*	6002	24.8	0.79 ± 0.01	10
Lockmann P10	*g*	3208	26.41	1.07 ± 0.02	7
Lockmann P10	*r*	2501	25.97	0.65 ± 0.01	5
Lockmann P10	*u*	3001	25.13	1.35 ± 0.02	5
Lockmann P10	*z*	6002	24.82	0.58 ± 0.01	10
Lockmann P11	*g*	2401	26.51	1.04 ± 0.01	5
Lockmann P11	*r*	2001	26.05	0.99 ± 0.01	4
Lockmann P11	*u*	5402	24.99	0.99 ± 0.02	9
Lockmann P11	*z*	6002	24.86	0.73 ± 0.01	10
Lockmann P12	*g*	2749	26.39	1.19 ± 0.02	6
Lockmann P12	*r*	2501	25.99	0.62 ± 0.01	5
Lockmann P12	*u*	3001	25.14	0.93 ± 0.02	5
Lockmann P12	*z*	6602	24.79	0.70 ± 0.01	11
Lockmann P13	*g*	2291	26.4	0.77 ± 0.01	5
Lockmann P13	*r*	2501	25.98	0.89 ± 0.01	5
Lockmann P13	*u*	3001	25.18	1.01 ± 0.01	5
Lockmann P13	*z*	7803	24.79	0.85 ± 0.01	13
Lockmann P14	*g*	2291	26.39	0.82 ± 0.01	5
Lockmann P14	*r*	3001	25.97	0.75 ± 0.01	6
Lockmann P14	*u*	3601	25.16	1.05 ± 0.02	6
Lockmann P14	*z*	6002	24.79	0.67 ± 0.01	10
Lockmann P15	*g*	2291	26.41	0.69 ± 0.01	5
Lockmann P15	*r*	3001	25.98	0.71 ± 0.01	6
Lockmann P15	*u*	3001	25.18	1.06 ± 0.02	5
Lockmann P15	*z*	6002	24.84	0.61 ± 0.01	10
Lockmann P2	*g*	2291	26.45	1.17 ± 0.03	5
Lockmann P2	*r*	2501	25.99	0.74 ± 0.01	5
Lockmann P2	*u*	3001	25.25	1.04 ± 0.02	5
Lockmann P2	*z*	6002	24.86	0.51 ± 0.01	10
Lockmann P3	*g*	2291	26.45	1.26 ± 0.02	5
Lockmann P3	*r*	2005	26.01	1.01 ± 0.02	4
Lockmann P3	*u*	3601	25.19	1.01 ± 0.01	6
Lockmann P3	*z*	6002	24.72	0.62 ± 0.01	10
Lockmann P4	*g*	5173	26.5	1.15 ± 0.02	11
Lockmann P4	*r*	5502	26.03	0.79 ± 0.01	11

Field name	Filter (name)	Exposure time (s)	Magnitude zeropoint (mag)	Seeing (″)	Images stacked (n)
Lockmann P4	*u*	3001	25.25	1.07 ± 0.01	5
Lockmann P4	*z*	6002	24.76	0.65 ± 0.01	10
Lockmann P5	*g*	4124	26.42	1.13 ± 0.02	9
Lockmann P5	*r*	2501	26.03	0.69 ± 0.01	5
Lockmann P5	*u*	3001	25.28	1.14 ± 0.01	5
Lockmann P5	*z*	6602	24.69	0.73 ± 0.00	11
Lockmann P6	*g*	7508	26.44	1.14 ± 0.02	16
Lockmann P6	*r*	7003	25.96	0.78 ± 0.01	14
Lockmann P6	*u*	4202	25.26	1.20 ± 0.02	7
Lockmann P6	*z*	6002	24.81	0.87 ± 0.01	10
Lockmann P7	*g*	2749	26.39	1.25 ± 0.02	6
Lockmann P7	*r*	2005	25.98	0.90 ± 0.01	4
Lockmann P7	*u*	3601	25.25	1.09 ± 0.02	6
Lockmann P7	*z*	6002	24.86	0.57 ± 0.01	10
Lockmann P8	*g*	2291	26.4	0.78 ± 0.01	5
Lockmann P8	*r*	3007	25.96	0.89 ± 0.01	6
Lockmann P8	*u*	4202	25.25	0.85 ± 0.03	7
Lockmann P8	*z*	6002	24.73	0.79 ± 0.01	10
Lockmann P9	*g*	3208	26.43	1.12 ± 0.02	7
Lockmann P9	*r*	2501	26.0	0.75 ± 0.01	5
Lockmann P9	*u*	3001	25.19	1.07 ± 0.02	5
Lockmann P9	*z*	6002	24.71	0.69 ± 0.00	10
XMM LSS A	*g*	5221	26.40	0.91 ± 0.05	18
XMM LSS A	*r*	4033	25.88	0.99 ± 0.01	7
XMM LSS A	*u*	15963	25.23	1.01 ± 0.03	42
XMM LSS A	*y*	3201	25.84	0.86 ± 0.01	8
XMM LSS A	*z*	6721	24.66	1.03 ± 0.01	12
XMM LSS B	*g*	2100	26.36	0.95 ± 0.01	5
XMM LSS B	*r*	3456	25.90	1.02 ± 0.01	6
XMM LSS B	*u*	13122	25.29	0.87 ± 0.03	34
XMM LSS B	*y*	1600	25.84	0.72 ± 0.01	4
XMM LSS B	*z*	9521	24.77	0.85 ± 0.01	17
XMM LSS C	*g*	4201	26.27	1.23 ± 0.03	10
XMM LSS C	*r*	4393	25.81	0.91 ± 0.07	9
XMM LSS C	*u*	3601	25.35	0.96 ± 0.01	6
XMM LSS C	*y*	1600	25.84	0.81 ± 0.01	4
XMM LSS C	*z*	6721	24.65	0.86 ± 0.01	12

APPENDIX B

Data Release Website

This appendix describes the final SWIRE-overlapping CFHT multi-color *ugriz* science data products, produced as described in Chapter 3, Section 3.4. Co-added images, weights, sum images and multi-color catalogs for 35 deg^2 are provided.

Website and files

The data release website address is:
`http://www.astro.uni-bonn.de/~tudorica/webpages/SpARCS/`.

For each field a zommable/pannable colour image is available on the left side of the page. Below each image (which can be changed by clicking on the corresponding link on the left), a few statistics are available in a small table: for each filter, the measured seeing, total exposure time, number of exposures used in coaddition and magnitude zeropoint are provided for a quick quality inspection. On the left side of the page, there is a table that contains for all fields and filters the coaddition, weights and sum images (FITS format), the multicolor catalogue containing the values for all parameters in the appendix (LDAC FITS format), the mask files (in DS9 format, both X,Y and RA,DEC), and finally a link to the systematics plots check-page (opens in new window). At the bottom of the table, bash scripts for download of the whole dataset (based on `wget`) are also provided for convenience.

Check-plots description

For each field, a systematics plots page is available. In the order they are arranged on the pages, they represent:

- First row: geometric distortion for each of the *gruz* filters
- Second row: 5σ/'' circular aperture depth maps for each of the same filters (*gruz*)
- Third row:

  - astrometric matching plot, showing the stars from an external catalog, the instrument footprint and the matches between the standard star (SDSS DR7 or 2MASS) and the internal catalog
  - $gr - ug$ color-color plot of galaxies in the field, showing with red the selected u-dropouts
  - $rz - gr$ color-color plot of galaxies in the field, showing with red the selected g-dropouts
  - comparison between the SDSS DR10 spectroscopic redshifts and the BPZ photometric redshifts for galaxies in the field
- Fourth row:
  - g-dropouts numbercounts
  - u-dropouts numbercounts
  - r-band PSF ellipticity before correction
  - r-band PSF residual ellipticity after correction
- Fifth row: difference between the SDSS DR10 and SExtractor measured magnitude for the stars common to both catalogues for each filter
- Sixth row: difference between the SDSS DR10 and SExtractor measured magnitude for the galaxies common to both catalogues for each filter
- Seventh row: stellar evolution models colour-colour predictions and measurements for stars in the field
- Eighth row: numbercounts of stars and galaxies in the field as a function of magnitude

Table B.1: CFHT optical data data release website keys description

Key name	Key description	Physical units
FIELD_POS	Reference number to field parameters	
SeqNr	running object number	
FLUX_ISO	Isophotal flux	count
FLUXERR_ISO	RMS error for isophotal flux	count
MAG_ISO	Isophotal magnitude	mag
MAGERR_ISO	RMS error for isophotal magnitude	mag
FLUX_ISOCOR	Corrected isophotal flux	count
FLUXERR_ISOCOR	RMS error for corrected isophotal flux	count
MAG_ISOCOR	Corrected isophotal magnitude	mag
MAGERR_ISOCOR	RMS error for corrected isophotal magnitude	mag
FLUX_APER	Flux vector within fixed circular aperture(s)	count
FLUXERR_APER	RMS error vector for aperture flux(es)	count
MAG_APER	Fixed aperture magnitude vector	mag
MAGERR_APER	RMS error vector for fixed aperture magnitude	mag
FLUX_AUTO	Flux within a Kron-like elliptical aperture	count
FLUXERR_AUTO	RMS error for AUTO flux	count
MAG_AUTO	Kron-like elliptical aperture magnitude	mag
MAGERR_AUTO	RMS error for AUTO magnitude	mag
FLUX_BEST	Best of FLUX_AUTO and FLUX_ISOCOR	count
FLUXERR_BEST	RMS error for BEST flux	count
MAG_BEST	Best of MAG_AUTO and MAG_ISOCOR	mag
MAGERR_BEST	RMS error for MAG_BEST	mag
KRON_RADIUS	Kron apertures in units of A or B	
BackGr	Background at centroid position	count
Level	Detection threshold above background	count
MU_THRESHOLD	Detection threshold above background	$\mathrm{mag} \cdot \mathrm{arcsec}^{-2}$
MaxVal	Peak flux above background	count
MU_MAX	Peak surface brightness above background	$\mathrm{mag} \cdot \mathrm{arcsec}^{-2}$
NPIX	Isophotal area above Analysis threshold	pixel^2
ISOAREA_WORLD	Isophotal area above Analysis threshold	deg^2
XMIN_IMAGE	Minimum x-coordinate among detected pixels	pixel
YMIN_IMAGE	Minimum y-coordinate among detected pixels	pixel
XMAX_IMAGE	Maximum x-coordinate among detected pixels	pixel
YMAX_IMAGE	Maximum y-coordinate among detected pixels	pixel
Xpos	Object position along x	pixel
Ypos	Object position along y	pixel
X_WORLD	Barycenter position along world x axis	deg
Y_WORLD	Barycenter position along world y axis	deg
XPEAK_IMAGE	x-coordinate of the brightest pixel	pixel
YPEAK_IMAGE	y-coordinate of the brightest pixel	pixel
XPEAK_WORLD	World-x coordinate of the brightest pixel	deg
YPEAK_WORLD	World-y coordinate of the brightest pixel	deg

Key name	Key description	Physical units
ALPHA_SKY	right ascension of barycenter (native)	deg
DELTA_SKY	Declination of barycenter (native)	deg
ALPHA_J2000	right ascension of barycenter (J2000)	deg
DELTA_J2000	Declination of barycenter (J2000)	deg
XM2	Variance along x	pixel^2
YM2	Variance along y	pixel^2
Corr	Covariance between x and y	pixel^2
X2_WORLD	Variance along X-WORLD (alpha)	deg^2
Y2_WORLD	Variance along Y-WORLD (delta)	deg^2
XY_WORLD	Covariance between X-WORLD and Y-WORLD	deg^2
CXX_IMAGE	Cxx object ellipse parameter	pixel^{-2}
CYY_IMAGE	Cyy object ellipse parameter	pixel^{-2}
CXY_IMAGE	Cxy object ellipse parameter	pixel^{-2}
CXX_WORLD	Cxx object ellipse parameter	(WORLD units) deg^{-2}
CYY_WORLD	Cyy object ellipse parameter	(WORLD units) deg^{-2}
CXY_WORLD	Cxy object ellipse parameter	(WORLD units) deg^{-2}
A	Profile RMS along major axis	pixel
B	Profile RMS along minor axis	pixel
A_WORLD	Profile RMS along major axis (world units)	deg
B_WORLD	Profile RMS along minor axis (world units)	deg
Theta	Position angle (CCW/x)	deg
THETA_WORLD	Position angle (CCW/world-x)	deg
THETA_SKY	Position angle (east of north) (native)	deg
THETA_J2000	Position angle (east of north) (J2000)	deg
ELONGATION	A_IMAGE/B_IMAGE	
ELLIPTICITY	1 - B_IMAGE/A_IMAGE	
ERRX2_IMAGE	Variance of position along x	pixel^2
ERRY2_IMAGE	Variance of position along	y pixel^2
ERRXY_IMAGE	Covariance of position between x and y	pixel^2
ERRX2_WORLD	Variance of position along X-WORLD (alpha)	deg^2
ERRY2_WORLD	Variance of position along Y-WORLD (delta)	deg^2
ERRXY_WORLD	Covariance of position X-WORLD/Y-WORLD	deg^2
ERRCXX_IMAGE	Cxx error ellipse parameter	pixel^{-2}
ERRCYY_IMAGE	Cyy error ellipse parameter	pixel^{-2}
ERRCXY_IMAGE	Cxy error ellipse parameter	pixel^{-2}
ERRCXX_WORLD	Cxx error ellipse parameter	(WORLD units) deg^{-2}
ERRCYY_WORLD	Cyy error ellipse parameter	(WORLD units) deg^{-2}
ERRCXY_WORLD	Cxy error ellipse parameter	(WORLD units) deg^{-2}
ERRA_IMAGE	RMS position error along major axis	pixel
ERRB_IMAGE	RMS position error along minor axis	pixel
ERRA_WORLD	World RMS position error along major axis	pixel
ERRB_WORLD	World RMS position error along minor axis	pixel
ERRTHETA_IMAGE	Error ellipse position angle (CCW/x)	deg

Key name	Key description	Physical units
ERRTHETA_WORLD	Error ellipse pos. angle (CCW/world-x)	deg
ERRTHETA_SKY	Native error ellipse pos. angle (east of north)	deg
ERRTHETA_J2000	J2000 error ellipse pos. angle (east of north)	deg
FWHM_IMAGE	FWHM assuming a gaussian core	pixel
FWHM_WORLD	FWHM assuming a gaussian core	deg
ISO0	Isophotal area at level 0	$pixel^2$
ISO1	Isophotal area at level 1	$pixel^2$
ISO2	Isophotal area at level 2	$pixel^2$
ISO3	Isophotal area at level 3	$pixel^2$
ISO4	Isophotal area at level 4	$pixel^2$
ISO5	Isophotal area at level 5	$pixel^2$
ISO6	Isophotal area at level 6	$pixel^2$
ISO7	Isophotal area at level 7	$pixel^2$
Flag	Extraction flags	
FLUX_RADIUS	Fraction-of-light radii	pixel
IMAFLAGS_ISO	FLAG-image flags averaged over the iso. profile	
NIMAFLAGS_ISO	Number of flagged pixels entering IMAFLAGS_ISO	
CLASS_STAR	S/G classifier output	
MAG_ISO_r	Isophotal magnitude	mag
MAG_ISOCOR_r	Corrected isophotal magnitude	mag
MAG_AUTO_r	Kron-like elliptical aperture magnitude	mag
MAG_APER_r	Fixed aperture magnitude vector	mag
MAGERR_ISO_r	RMS error for isophotal magnitude	mag
MAGERR_ISOCOR_r	RMS error for corrected isophotal magnitude	mag
MAGERR_AUTO_r	RMS error for AUTO magnitude	mag
MAGERR_APER_r	RMS error vector for fixed aperture mag.	mag
FLUX_ISO_r	Isophotal flux	count
FLUX_ISOCOR_r	Corrected isophotal flux	count
FLUX_AUTO_r	Flux within a Kron-like elliptical aperture	count
FLUX_APER_r	Flux vector within fixed circular aperture(s)	count
FLUXERR_ISO_r	RMS error for isophotal flux	count
FLUXERR_ISOCOR_r	RMS error for corrected isophotal flux	count
FLUXERR_AUTO_r	RMS error for AUTO flux	count
FLUXERR_APER_r	RMS error vector for aperture flux(es)	count
IMAFLAGS_ISO_r	FLAG-image flags averaged over the iso. profile	
MAG_LIM_r	Limit magnitude in the *r*-band	mag
EXTINCTION_r		mag
MAG_ISO_u	Isophotal magnitude	mag
MAG_ISOCOR_u	Corrected isophotal magnitude	mag
MAG_AUTO_u	Kron-like elliptical aperture magnitude	mag
MAG_APER_u	Fixed aperture magnitude vector	mag
MAGERR_ISO_u	RMS error for isophotal magnitude	mag
MAGERR_ISOCOR_u	RMS error for corrected isophotal magnitude	mag

Key name	Key description	Physical units
MAGERR_AUTO_u	RMS error for AUTO magnitude	mag
MAGERR_APER_u	RMS error vector for fixed aperture mag.	mag
FLUX_ISO_u	Isophotal flux	count
FLUX_ISOCOR_u	Corrected isophotal flux	count
FLUX_AUTO_u	Flux within a Kron-like elliptical aperture	count
FLUX_APER_u	Flux vector within fixed circular aperture(s)	count
FLUXERR_ISO_u	RMS error for isophotal flux	count
FLUXERR_ISOCOR_u	RMS error for corrected isophotal flux	count
FLUXERR_AUTO_u	RMS error for AUTO flux	count
FLUXERR_APER_u	RMS error vector for aperture flux(es)	count
IMAFLAGS_ISO_u	FLAG-image flags averaged over the iso. profile	
MAG_LIM_u	Limit magnitude in the *u*-band	mag
EXTINCTION_u		mag
MAG_ISO_g	Isophotal magnitude	mag
MAG_ISOCOR_g	Corrected isophotal magnitude	mag
MAG_AUTO_g	Kron-like elliptical aperture magnitude	mag
MAG_APER_g	Fixed aperture magnitude vector	mag
MAGERR_ISO_g	RMS error for isophotal magnitude	mag
MAGERR_ISOCOR_g	RMS error for corrected isophotal magnitude	mag
MAGERR_AUTO_g	RMS error for AUTO magnitude	mag
MAGERR_APER_g	RMS error vector for fixed aperture mag.	mag
FLUX_ISO_g	Isophotal flux	count
FLUX_ISOCOR_g	Corrected isophotal flux	count
FLUX_AUTO_g	Flux within a Kron-like elliptical aperture	count
FLUX_APER_g	Flux vector within fixed circular aperture(s)	count
FLUXERR_ISO_g	RMS error for isophotal flux	count
FLUXERR_ISOCOR_g	RMS error for corrected isophotal flux	count
FLUXERR_AUTO_g	RMS error for AUTO flux	count
FLUXERR_APER_g	RMS error vector for aperture flux(es)	count
IMAFLAGS_ISO_g	FLAG-image flags averaged over the iso. profile	
MAG_LIM_g	Limit magnitude in the *g*-band	mag
EXTINCTION_g		mag
MAG_ISO_z	Isophotal magnitude	mag
MAG_ISOCOR_z	Corrected isophotal magnitude	mag
MAG_AUTO_z	Kron-like elliptical aperture magnitude	mag
MAG_APER_z	Fixed aperture magnitude vector	mag
MAGERR_ISO_z	RMS error for isophotal magnitude	mag
MAGERR_ISOCOR_z	RMS error for corrected isophotal magnitude	mag
MAGERR_AUTO_z	RMS error for AUTO magnitude	mag
MAGERR_APER_z	RMS error vector for fixed aperture mag.	mag
FLUX_ISO_z	Isophotal flux	count
FLUX_ISOCOR_z	Corrected isophotal flux	count
FLUX_AUTO_z	Flux within a Kron-like elliptical aperture	count

Key name	Key description	Physical units
FLUX_APER_z	Flux vector within fixed circular aperture(s)	count
FLUXERR_ISO_z	RMS error for isophotal flux	count
FLUXERR_ISOCOR_z	RMS error for corrected isophotal flux	count
FLUXERR_AUTO_z	RMS error for AUTO flux	count
FLUXERR_APER_z	RMS error vector for aperture flux(es)	count
IMAFLAGS_ISO_z	FLAG-image flags averaged over the iso. profile	
MAG_LIM_z	Limit magnitude in the z-band	mag
EXTINCTION_z	Extinction in the z-band	mag
MASK value	MASK flag value	
Z_B	Most likely value of the redshift	
Z_B_MIN	95%-confidence interval lower limit on redshift	
Z_B_MAX	95%-confidence interval upper limit on redshift	
T_B	Most likely spectral type	
ODDS	Likelihood that Z_B is correct within 0.1	
Z_ML	Maximum Likelihood results (flat unphysical prior)	
T_ML	Maximum Likelihood results (flat unphysical prior)	
CHI_SQUARED_BPZ	Modified χ^2	
BPZ_FILT	Filters with good photometry (BPZ)	
NBPZ_FILT	Number of filters with good photometry (BPZ)	
BPZ_NONDETFILT	Filters with faint photometry (BPZ)	
NBPZ_NONDETFILT	Number of filters with faint photometry (BPZ)	
BPZ_FLAGFILT	Flagged filters (BPZ)	
NBPZ_FLAGFILT	Number of flagged filters (BPZ)	

Bibliography

Abazajian, K., Zheng, Z., Zehavi, I., et al. 2005, ApJ, 625, 613

Ahn, C. P., Alexandroff, R., Allende Prieto, C., et al. 2014, apjs, 211, 17

Andreon, S. & Bergé, J. 2012, aap, 547, A117

Andreon, S. & Hurn, M. A. 2010, mnras, 404, 1922

Bardeen, J. M., Bond, J. R., Kaiser, N., & Szalay, A. S. 1986, ApJ, 304, 15

Bartelmann, M. 1996, aap, 313, 697

Bartelmann, M. & Schneider, P. 2001, physrep, 340, 291

Benítez, N. 2000, apj, 536, 571

Bertin, E. 2006, in Astronomical Society of the Pacific Conference Series, Vol. 351, Astronomical Data Analysis Software and Systems XV, ed. C. Gabriel, C. Arviset, D. Ponz, & S. Enrique, 112

Bertin, E. & Arnouts, S. 1996, aaps, 117, 393

Bertin, E., Mellier, Y., Radovich, M., et al. 2002, in Astronomical Society of the Pacific Conference Series, Vol. 281, Astronomical Data Analysis Software and Systems XI, ed. D. A. Bohlender, D. Durand, & T. H. Handley, 228

Blaizot, J., Guiderdoni, B., Devriendt, J. E. G., et al. 2004, MNRAS, 352, 571

Blindert, K., Yee, H. K. C., Gladders, M. D., Ellingson, E., & Golding, J. 2004, in Bulletin of the American Astronomical Society, Vol. 36, American Astronomical Society Meeting Abstracts, 1609

Brodwin, M., McDonald, M., Gonzalez, A. H., et al. 2016, ApJ, 817, 122

Clowes, R. G., Harris, K. A., Raghunathan, S., et al. 2013, MNRAS, 429, 2910

Corless, V. L. & King, L. J. 2007, MNRAS, 380, 149

Davis, T. M. & Lineweaver, C. H. 2004, PASA, 21, 97

Davis, T. M., Mörtsell, E., Sollerman, J., et al. 2007, ApJ, 666, 716

de Jong, J. T. A., Kuijken, K., Applegate, D., et al. 2013, The Messenger, 154, 44

Demarco, R., Wilson, G., Muzzin, A., et al. 2010, ApJ, 711, 1185

Dietrich, J. P., Erben, T., Lamer, G., et al. 2007, aap, 470, 821

Duffy, A. R., Schaye, J., Kay, S. T., & Dalla Vecchia, C. 2008, MNRAS, 390, L64

Einstein, A. 1915a, Sitzungsberichte der Königlich Preußischen Akademie der Wissenschaften (Berlin), Seite 844-847.

Einstein, A. 1915b, Sitzungsberichte der Königlich Preußischen Akademie der Wissenschaften (Berlin), Seite 831-839.

Einstein, A. 1915c, Sitzungsberichte der Königlich Preußischen Akademie der Wissenschaften (Berlin), Seite 778-786.

Einstein, A. 1915d, Sitzungsberichte der Königlich Preußischen Akademie der Wissenschaften (Berlin), Seite 799-801.

Einstein, A. 1916, Annalen der Physik, 354, 769

Eisenstein, D. J. & Hu, W. 1998, ApJ, 496, 605

Ellis, G. F. R. 2006, General Relativity and Gravitation, 39, 1047

Erben, T., Hildebrandt, H., Lerchster, M., et al. 2009, aap, 493, 1197

Erben, T., Hildebrandt, H., Miller, L., et al. 2013, mnras, 433, 2545

Ettori, S., Borgani, S., Moscardini, L., et al. 2004, MNRAS, 354, 111

Fazio, G. G., Hora, J. L., Allen, L. E., et al. 2004, apjs, 154, 10

Feroz, F. & Hobson, M. P. 2012, MNRAS, 420, 596

Ford, J., Hildebrandt, H., Van Waerbeke, L., et al. 2014, mnras, 439, 3755

Ford, J., Hildebrandt, H., Van Waerbeke, L., et al. 2012, apj, 754, 143

Friedmann, A. 1922, Zeitschrift fur Physik, 10, 377

Giavalisco, M., Steidel, C. C., & Macchetto, F. D. 1996, ApJ, 470, 189

Gilbank, D. G., Bower, R. G., Castander, F. J., & Ziegler, B. L. 2004, mnras, 348, 551

Gilbank, D. G., Yee, H. K. C., Ellingson, E., et al. 2007, AJ, 134, 282

Giodini, S., Lovisari, L., Pointecouteau, E., et al. 2013, ssr, 177, 247

Gladders, M. D. & Yee, H. K. C. 2000, aj, 120, 2148

Gladders, M. D. & Yee, H. K. C. 2005, apjs, 157, 1

Gladders, M. D., Yee, H. K. C., Majumdar, S., et al. 2007, ApJ, 655, 128

Gonzalez, A. H., Sivanandam, S., Zabludoff, A. I., & Zaritsky, D. 2013, ApJ, 778, 14

Harrison, E. R. 1970, Phys. Rev. D, 1, 2726

Hartlap, J., Simon, P., & Schneider, P. 2007, aap, 464, 399

Heymans, C., Van Waerbeke, L., Miller, L., et al. 2012, mnras, 427, 146

Hildebrandt, H., Erben, T., Kuijken, K., et al. 2012, mnras, 421, 2355

Hildebrandt, H., Pielorz, J., Erben, T., et al. 2009, aap, 498, 725

Hildebrandt, H., van Waerbeke, L., Scott, D., et al. 2013, mnras, 429, 3230

Horvath, I., Hakkila, J., & Bagoly, Z. 2013, ArXiv e-prints [[arXiv]1311.1104]

Ivezic, Z., Tyson, J. A., Abel, B., et al. 2008, ArXiv e-prints, astro-ph/0805.2366 [[arXiv]0805.2366]

Jenkins, A., Frenk, C. S., White, S. D. M., et al. 2001, mnras, 321, 372

Johnston, D. E., Sheldon, E. S., Wechsler, R. H., et al. 2007, ArXiv e-prints [[arXiv]0709.1159]

Kaiser, N. 1984, ApJ, 284, L9

Kaiser, N. 1986, MNRAS, 222, 323

Koester, B. P., McKay, T. A., Annis, J., et al. 2007, ApJ, 660, 221

Komatsu, E., Dunkley, J., Nolta, M. R., et al. 2009, ApJS, 180, 330

Kotov, O. & Vikhlinin, A. 2005, ApJ, 633, 781

Kravtsov, A. V. & Borgani, S. 2012, ARA&A, 50, 353

Kuijken, K. 2008, aap, 482, 1053

Laureijs, R., Amiaux, J., Arduini, S., et al. 2011, ArXiv e-prints, astro-ph/1110.3193 [[arXiv]1110.3193]

Le Fèvre, O., Cassata, P., Cucciati, O., et al. 2013, aap, 559, A14

Lemaître, G. 1933, Annales de la Société Scientifique de Bruxelles, 53

Lonsdale, C. J., Smith, H. E., Rowan-Robinson, M., et al. 2003, pasp, 115, 897

Magnier, E. A. & Cuillandre, J.-C. 2004, pasp, 116, 449

Ménard, B., Hamana, T., Bartelmann, M., & Yoshida, N. 2003, aap, 403, 817

Milkeraitis, M., van Waerbeke, L., Heymans, C., et al. 2010, mnras, 406, 673

Morrison, C. B., Scranton, R., Ménard, B., et al. 2012, mnras, 426, 2489

Munari, E., Biviano, A., Borgani, S., Murante, G., & Fabjan, D. 2013, MNRAS, 430, 2638

Murray, S. G., Power, C., & Robotham, A. S. G. 2013, Astronomy and Computing, 3, 23

Muzzin, A., Wilson, G., Lacy, M., Yee, H. K. C., & Stanford, S. A. 2008, apj, 686, 966

Muzzin, A., Wilson, G., Yee, H. K. C., et al. 2012, apj, 746, 188

Muzzin, A., Wilson, G., Yee, H. K. C., et al. 2009, The Astrophysical Journal, 698, 1934

Muzzin, A., Yee, H. K. C., Hall, P. B., & Lin, H. 2007, apj, 663, 150

Narayan, R. 1989, apjl, 339, L53

Navarro, J. F., Frenk, C. S., & White, S. D. M. 1997, apj, 490, 493

O'Hara, T. B., Mohr, J. J., Bialek, J. J., & Evrard, A. E. 2006, ApJ, 639, 64

Pacaud, F., Pierre, M., Adami, C., et al. 2007, MNRAS, 382, 1289

Peacock, J. A. 2007, MNRAS, 379, 1067

Peacock, J. A. & Dodds, S. J. 1996, mnras, 280, L19

Peebles, P. J. E. & Yu, J. T. 1970, ApJ, 162, 815

Percival, W. J., Cole, S., Eisenstein, D. J., et al. 2007, MNRAS, 381, 1053

Planck Collaboration, Ade, P. A. R., Aghanim, N., et al. 2016, A&A, 594, A20

Planck Collaboration, Ade, P. A. R., Aghanim, N., et al. 2015a, ArXiv e-prints [[arXiv]1502.01589]

Planck Collaboration, Ade, P. A. R., Aghanim, N., et al. 2015b, ArXiv e-prints [[arXiv]1502.01589]

Press, W. H. & Schechter, P. 1974, apj, 187, 425

Raichoor, A., Mei, S., Erben, T., et al. 2014, apj, 797, 102

Reichert, A., Böhringer, H., Fassbender, R., & Mühlegger, M. 2011, A&A, 535, A4

Rieke, G. H., Young, E. T., Engelbracht, C. W., et al. 2004, apjs, 154, 25

Riess, A. G., Strolger, L.-G., Tonry, J., et al. 2004, ApJ, 607, 665

Robertson, H. P. 1935, ApJ, 82, 284

Rozo, E., Rykoff, E., Koester, B., et al. 2011, ApJ, 740, 53

Rozo, E., Rykoff, E. S., Evrard, A., et al. 2009a, apj, 699, 768

Rozo, E., Rykoff, E. S., Koester, B. P., et al. 2009b, ApJ, 703, 601

Rozo, E. & Schmidt, F. 2010, ArXiv e-prints, astro-ph/1009.5735 [[arXiv]1009.5735]

Rykoff, E. S., Koester, B. P., Rozo, E., et al. 2012, ApJ, 746, 178

Schneider, P. 2006, Extragalactic Astronomy and Cosmology (Springer, 2006.)

Schneider, P. & Seitz, C. 1995, A&A, 294, 411

Schuecker, P., Caldwell, R. R., Böhringer, H., et al. 2003, A&A, 402, 53

Scranton, R., Ménard, B., Richards, G. T., et al. 2005, apj, 633, 589

Seljak, U. & Warren, M. S. 2004, mnras, 355, 129

Skrutskie, M. F., Cutri, R. M., Stiening, R., et al. 2006, aj, 131, 1163

Smith, R. E., Peacock, J. A., Jenkins, A., et al. 2003, mnras, 341, 1311

Spergel, D. N., Verde, L., Peiris, H. V., et al. 2003, ApJS, 148, 175

Steidel, C. C., Adelberger, K. L., Dickinson, M., et al. 1998, apj, 492, 428

Steidel, C. C. & Hamilton, D. 1993, aj, 105, 2017

Takada, M. 2010, in American Institute of Physics Conference Series, Vol. 1279, American Institute of Physics Conference Series, ed. N. Kawai & S. Nagataki, 120–127

The Dark Energy Survey Collaboration. 2005, ArXiv Astrophysics e-prints, astro-ph/0510346 [astro-ph/0510346]

Tinker, J., Kravtsov, A. V., Klypin, A., et al. 2008, ApJ, 688, 709

Tinker, J. L. 2005, PhD thesis, The Ohio State University, Ohio, USA

Tinker, J. L., Robertson, B. E., Kravtsov, A. V., et al. 2010, ApJ, 724, 878

Tonry, J. L., Schmidt, B. P., Barris, B., et al. 2003, ApJ, 594, 1

Tudorica, A., Hildebrandt, H., Tewes, M., et al. 2017, A&A, 608, A141

Umetsu, K., Broadhurst, T., Zitrin, A., Medezinski, E., & Hsu, L.-Y. 2011, The Astrophysical Journal, 729, 127

van den Bosch, F. C., Yang, X., & Mo, H. J. 2003, MNRAS, 340, 771

van der Burg, R. F. J., Hildebrandt, H., & Erben, T. 2010, aap, 523, A74

van der Burg, R. F. J., Muzzin, A., Hoekstra, H., et al. 2014, aap, 561, A79

van Uitert, E., Gilbank, D. G., Hoekstra, H., et al. 2016, A&A, 586, A43

Van Waerbeke, L., Hildebrandt, H., Ford, J., & Milkeraitis, M. 2010, apjl, 723, L13

Vandame, B. 2001, in Mining the Sky, ed. A. J. Banday, S. Zaroubi, & M. Bartelmann, 595

Vikhlinin, A., Kravtsov, A. V., Burenin, R. A., et al. 2009, ApJ, 692, 1060

Walker, A. G. 1937, Proceedings of the London Mathematical Society, s2-42, 90

Wheeler, J. A. & Ford, K. 1998, Geons, black holes and quantum foam : a life in physics (New York, NY: Norton)

Wilson, G., Gladders, M., Hoekstra, H., et al. 2005, Detecting Clusters of Galaxies at 1 < z < 2 in the SWIRE Legacy Fields., Spitzer Proposal

Wilson, G., Muzzin, A., Yee, H. K. C., et al. 2009, The Astrophysical Journal, 698, 1943

Wright, C. O. & Brainerd, T. G. 2000, apj, 534, 34

Yadav, J. K., Bagla, J. S., & Khandai, N. 2010, MNRAS, 405, 2009

Yee, H. K. C. & Ellingson, E. 2003, apj, 585, 215

Yee, H. K. C., Ellingson, E., & Carlberg, R. G. 1996, ApJS, 102, 269

Yee, H. K. C. & López-Cruz, O. 1999, aj, 117, 1985

Yoo, J., Fitzpatrick, A. L., & Zaldarriaga, M. 2009, Phys. Rev. D, 80, 083514

Zehavi, I., Eisenstein, D. J., Nichol, R. C., et al. 2005, ApJ, 621, 22

Zeldovich, Y. B. 1972, Monthly Notices of the Royal Astronomical Society, 160, 1P

Zheng, Z., Coil, A. L., & Zehavi, I. 2007, ApJ, 667, 760

Acknowledgements

I would like to thank several people who stimulated and encouraged me throughout the thesis work:

- Prof. Dr. Hendrik Hildebrandt, my supervisor, who continuously encouraged and inspired me throughout my PhD
- Prof. Dr. Peter Schneider for the continuous influence and support over the years
- Professor Dr. Ian Brock and Professor. Dr. Helmut Baltruschat for accepting to be part of the thesis committee
- Malte Tewes, Jennifer Pollack and Katharina Bohm, who were the best office mates one could hope for
- Gabriela Ileana Tudorica-Iacobuta and my family, always by my side

The research was partially supported by the DFG Emmy Noether grant Hi 1495/2-1.

This work is based in part on observations obtained with MegaCam, a joint project of CFHT and CEA/IRFU, at the CFHT which is operated by the National Research Council (NRC) of Canada, the Institut National des Sciences de l'Univers of the Centre National de la Recherche Scientifique (CNRS) of France, and the University of Hawaii. This research used the facilities of the Canadian Astronomy Data Centre operated by the National Research Council of Canada with the support of the Canadian Space Agency. CFHTLenS data processing was made possible thanks to significant computing support from the NSERC Research Tools and Instruments grant program.

The thesis is also partly based on observations made with the Spitzer Space Telescope, which is operated by the Jet Propulsion Laboratory, California Institute of Technology under a contract with NASA.

List of publications

Refereed publications related to the thesis

- A. Tudorica, H. Hildebrandt, M. Tewes, H. Hoekstra, C.B. Morrison, A. Muzzin, G. Wilson, H.K.C. Yee, C. Lidman, A. Hicks, J. Nantais, T. Erben, R. F. J. van der Burg, R. Demarco., "Weak lensing magnification of SpARCS galaxy clusters", 2017, A&A, 608, A141